A CHEMICAL REACTION ENGINEERING PERSPECTIVE OF POLYMER ELECTROLYTE MEMBRANE FUEL CELLS

Ee-Sunn Chia

A DISSERTATION

PRESENTED TO THE FACULTY

OF PRINCETON UNIVERSITY

IN CANDIDACY FOR THE DEGREE

OF DOCTOR OF PHILOSOPHY

2006

Acknowledgments

I am tremendously grateful for the unsurpassable guidance I have received throughout my entire graduate career from both my advisors Yannis and Jay. They have continually guided me to be the engineer that I am today. The opportunity to work with them simultaneously has been an invaluable learning experience.

My years in Princeton have flown by in the blink of the eye with friends that have unfaltering energy to encourage and have fun. I'll treasure the lunches, the dinners, the game cube *duels*, our road trips, and the izakaya hopping. Many thanks to my closest friends: Kat, Scott, Wanwipa, Phil, Daniel, Seachol, Sonia, Jason, and Mahdi. I'm also thankful for wonderful labmates – both former and current Kevrekidis and Benziger group members.

I am forever grateful for the support and motivation from my family. Although hundreds and thousands of miles away, they were and are always just a phone call or an email away. I owe it all to mom, dad, my brother Jason, and my sister Janice, for inspiring me to get to where I am today.

Most importantly, I thank Lawrence for encouraging me throughout my academic life from Virginia to Princeton. I am often in awe when I think about the confidence he has instilled in me. Lawrence, thanks for being the patient listener, the exceptional friend, and the caring husband.

Abstract

Polymer electrolyte membrane (PEM) fuel cells that are modeled and constructed as a *differential* reactor enable an examination of the kinetics and dynamics associated with the operating fuel cell. The differential reactor bypasses more complex two- and three-dimensional integral reactors and simplifies the fuel cell to a one dimensional system where spatial gradients are removed. The balance between water production and water removal in the differential reactor gives rise to ignition/extinction phenomena and multiple steady states. This phenomenon is a direct result of the polymer electrolyte membrane's role as a *reservoir* for water. A remarkable analogy between water balance in the differential fuel PEM fuel cell and the energy balance in the classical exothermic stirred tank reactor can be established.

In the initial chapters of this thesis, the rationale behind the design of the PEM fuel cell as a differential reactor is described. A mathematical model of the PEM fuel cell as a stirred tank which incorporates four of the key operating parameters: load resistance, fuel cell temperature, inlet hydrogen flow rate, and inlet oxygen flow rate, successfully captures the ignition/extinction phenomena. Changes in the water inventory as a result of a change in any operating parameter will alter the membrane resistance. This affects the rate of water production and ultimately will affect ignition/extinction.

In the later chapters of this thesis, the differential reactor is used as a building block to model the *integral* type fuel cell reactors. The segmented anode parallel channel PEM fuel cell was developed to provide insight into the inner workings of the fuel cell. Specifically, this version of the fuel cell enabled individual current measurements within

each segment which led to a spatial observation of the ignition front. A model of this segmented anode parallel channel fuel cell based on coupled stirred tanks in series is also presented at the end. In addition to the effects of the operating parameters on the fuel cell operation, flow effects (co- and counter-current), and also configuration effects were studied.

Contents

List of Figures

List of Tables

Chapter 1

Introduction and Overview

Although polymer electrolyte membrane (PEM) fuel cells have recently garnered widespread attention as an alternative power source, they were actually developed over forty years ago (Fuel Cell Handbook, 2000). In the early 1960s, PEM fuel cells developed by General Electric (GE) were used as a primary power source in Gemini spacecrafts. Unfortunately, both the lifetime and performance of PEM fuel cells were unsatisfactory until DuPont introduced a perfluorosulfonic-acid membrane with a Teflon backbone, named Nafion™, in 1968. With the introduction of Nafion, cell performance improved dramatically with power densities reaching 100 W/ft^2 in 1970 and observed lifetimes on the order of 10^3 hours (Watkins, 1993).

After the dramatic improvement brought forth by Nafion, other companies and federal agencies such as United Technologies Corporation (UTC), Ballard Power Systems and Los Alamos National Laboratory (LANL) continued research in PEM fuel cells. However, breakthroughs in PEM fuel cells were difficult due to the unreasonably high costs associated with the catalyst and the membrane. Therefore, PEM fuel cells remained

largely unnoticed until Raistrick and his group at LANL discovered a method to impregnate the gas diffusion electrodes with Nafion before hot pressing the electrodes onto the membrane itself (Raistrick, 1986). This method led to a dramatic reduction in catalyst requirements from 4 mg/cm^2 of platinum to to 0.05 mg/cm^2. This breakthrough in catalyst reduction paved the way for more recent research in PEM fuel cells.

1.1 Obstacles to Fuel Cell Development

PEM fuel cells are extensively pursued for both mobile and stationary power applications (Fuel Cell Handbook, 2000; Acres, 2001; Perry and Fuller, 2002). More recently, PEM fuel cells have become particularly attractive for automobile and mobile electronic applications due to their relatively lightweight and compact construction in addition to their low operating temperature. However, researchers will need to address several key issues in PEM fuel cell development before they will be able to mass produce and market PEM fuel cells as a consumer product. Four main concerns in PEM fuel cell development are discussed in what follows and are summarized in Figure 1.

1.1.1 Hydrogen Production

Concerns about the increased dependence on energy and exhausting the natural nonrenewable fossil-fuels spurred interests in using hydrogen as a nonpolluting alternative. In 1973, Gregory presented a case to divert all energy sources towards hydrogen production but research efforts in this area continue until today (Gregory, 1973). Hydrogen seems like a suitable fuel alternative since it is the most abundant element on earth

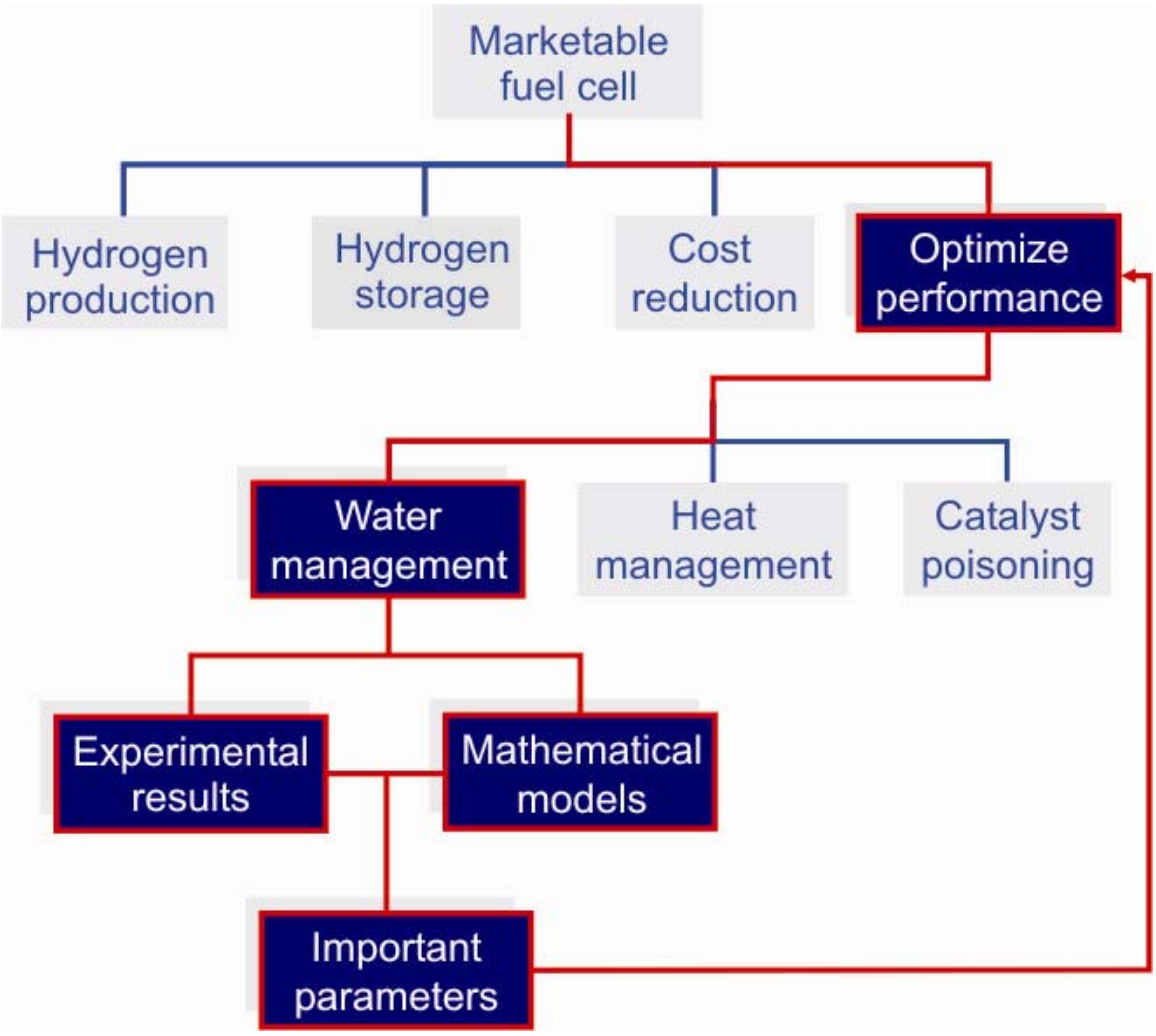

Figure 1: Our PEM fuel cell research pathway. We address the issue of PEM fuel cell performance by introducing a *differential* PEM fuel cell which enables us to focus on water management in the cell. In the later chapters, we will see that water is a variable that gives rise to complex nonlinear dynamical behavior reminiscent of classical exothermic stirred tank reactor dynamics. Through both experimental and modeling efforts, we identify parameters that help us operate and optimize the fuel cell performance.

with an excellent energy density per weight. However, it is unfortunate that pure hydrogen sources are scarce; hydrogen is largely available in water and hydrocarbons.

The simplest method of hydrogen production is the electrolysis of water but the electricity requirements make this an expensive route. A more common method of hydrogen production is steam reforming of natural gas which is followed by the water gas shift reaction to remove carbon monoxide.

$$CH_4 + H_2O \rightarrow 3H_2 + CO$$

$$CO + H_2O \rightarrow H_2 + CO_2$$

Most of the hydrogen produced today is used for mainly two chemical processes: ammonia production and fuel hydrocracking. Existing hydrogen production methods will not generate enough hydrogen to meet the demands of a hydrogen economy. In a commentary on hydrogen, Grant (Grant, 2003) estimates that 230,000 tonnes of hydrogen need to be produced daily to sustain an economy dependent on fuel cell surface transportation. Grant also draws to attention the enormous number of new power plants required to meet this requirement: 800 natural gas plants generating 500 MW which is equivalent to 500 coal fired units (800 MW) or 200 Hoover Dams that generate 2 GW each. The cost associated with constructing these new plants is undoubtedly a huge barrier. Some also argue that splitting water to produce hydrogen creates as much greenhouse gas as petroleum fuels (Grant, 2003; Washington, 2003).

In order to meet forecasted levels of hydrogen usage, newer methods of hydrogen production are necessary. One such method is the autothermal reforming of ethanol to produce hydrogen developed by Deluga et al. (Deluga et al., 2004). Hydrogen produc-

tion, directly or even indirectly, from biomass will aid in reducing greenhouse emissions as well.

1.1.2 Hydrogen Storage

A breakthrough in hydrogen production will pave the way to a more realistic hydrogen economy but overcoming the hydrogen production problem alone is insufficient because hydrogen storage remains an issue. Conventional storage methods in tanks/cylinders are difficult to implement for gaseous hydrogen due to the extremely large volume that gaseous hydrogen occupies. One solution is to pressurize the gas and store it in specially designed tanks reinforced with carbon fibers. However, there are also concerns that gaseous hydrogen is light enough to result in leakage from its storage medium.

Another alternative is to liquefy the gaseous hydrogen and store it in insulated double-walled vessels (Wolf, 2002). Since cryogenic liquid hydrogen boils at -252°C, precautionary measures to minimize boil-off are necessary. The vessels used to store liquid hydrogen are thus insulated with several layers. Newer methods of hydrogen storage which are actively pursued include using various carbon forms: carbon nanotubes, intercalated plates, and carbon fibers (Baughman et al., 2002; Chambers et al., 1998; Dillon et al., 1997; Liu et al., 1999). Crystalline metal organic frameworks that contain uniform internal structure and size have also been suggested as possible media for hydrogen storage (Rosi et al., 2003). Researchers have also used metals and alloys that can reversibly absorb hydrogen, resulting in metal hydrides (Bogdanovic et al., 2000; Schlapbach and Zuttel, 2001; Zaluski et al., 1997).

1.1.3 Cost

Most PEM fuel cells use a form of perfluorosulfonated acid membrane such as Nafion (produced by DuPont). Unfortunately, the large cost of Nafion membranes is another major impediment for commercial fuel cells. Therefore, alternative proton conducting membranes such as composite membranes (Liu et al., 2003; Nakajima and Honma, 2002; Yang, 2003) and hydrocarbon polymers are being developed (Kreuer, 2001; Rikukawa and Sanui, 2000). Aside from membrane cost alone, efforts to develop better and cheaper electrodes also exist (Ralph et al., 1997). Further decrease in the platinum catalyst loading requirements would help as well.

With any new technology, cost concerns are inevitable when it comes to developing a new hydrogen infrastructure to support the anticipated hydrogen demands for fuel cells. As mentioned previously, hydrogen production and storage methods need to be improved significantly before they are economically viable. For hydrogen production, a suitable feedstock and production method will need to be discovered before hydrogen becomes a competitive alternative to gasoline (Agrawal et al., 2005).

1.1.4 Better Performance Fuel Cells

Fuel cells for mobile applications will necessarily adjust to various non-steady state requirements such as variable loads in power plants, climate effects on temperature and humidity, and fast changes such as vehicle acceleration. The fuel cell performance will need to be optimized for maximum power output under such changes. To develop optimized fuel cells, three main issues need to be addressed: water management, heat management, and catalyst poisoning.

Water management is a vital concern in PEM fuel cells because an optimum level of water is necessary for the fuel cell to function. The membrane can only conduct the protons if it is sufficiently humidified. However, too much water will result in flooding that will create additional mass transport resistances for the reactants that are trying to reach the catalyst.

Individual PEM fuel cells do not generate enough power for commercial applications. PEM fuel cells in practical applications will be produced in the form of fuel cell stacks that will generate enough power (Amphlett et al., 1994; Chu and Jiang, 1999; Hamelin et al., 2001; Lee and Lalk, 1998). Heat management is important when we consider the heat dissipation from the fuel cell stacks.

Hydrogen sources that are reformed from hydrocarbon fuels often contain traces of carbon monoxide that can poison the catalyst. Since current catalysts have very low carbon monoxide tolerances, more robust catalysts need to be developed to withstand such poisoning. Methods to generate cleaner hydrogen feeds must also be introduced.

1.2 Our Approach to PEM Fuel Cells

Before PEM fuel cells become a commercially viable alternative power source, it is critical that predictive models of fuel cell performance for realistic operating conditions are developed. Many PEM models attempt to capture the internal workings of an operating fuel cell (Bernardi and Verbrugge, 1992; Fuller and Newman, 1993; Janssen, 2001; Pisani et al., 2002; Springer et al., 1991). However, such models often include intricate details that create additional complexity. Predictive models of fuel cell performance that

correctly incorporate the transient interplay of reaction and transport processes are therefore critical.

Out of the four concerns highlighted above, we focus our research efforts in optimizing the PEM fuel cell performance via a better understanding of what we believe is the most interesting and controlling factor: water management. In this dissertation, we apply fundamental reaction engineering knowledge to study a novel PEM fuel cell that enables us to observe the effects of water on the fuel cell operation. We first review the PEM fuel cell, its components, and provide an overview of PEM fuel cell modeling efforts in Chapter 2.

In Chapter 3, we present the rationale behind our *differential* PEM fuel cell reactor that was designed and constructed to examine kinetics and dynamics (Benziger et al., 2005a; Benziger et al., submitted; Benziger et al., 2004; Benziger et al., 2005d). We show that this differential reactor design, which bypasses the additional complexity of two- and three-dimensional integral reactors (Bernardi and Verbrugge, 1992; Fuller and Newman, 1993; Janssen, 2001; Springer et al., 1991) focuses on reaction/transport dynamic coupling under well-defined conditions. The differential PEM fuel cell (stirred tank reactor (STR) PEM fuel cell) response is experimentally tracked as a function of the controllable operating parameters: temperature, external load resistance, or hydrogen and oxygen feed flow rates. Here, we also establish that the membrane functions as a reservoir for water in the fuel cell. This will be closely tied to the ignition/extinction phenomena and multiple steady states that were reproducibly demonstrated by Moxley et al. (Moxley et al., 2003). The experiments suggested that the proton transport dependence on water activity in the PEM membrane underpins the observed dynamical phenomena.

Water ionizes and shields stationary anions in the membrane which causes proton transport to increase by orders of magnitude.

We present and analyze a remarkable analogy between water balance in the differential PEM fuel cell and energy balance in the classical exothermic stirred tank reactor in Chapter 4. This is accomplished through a simplified model that embodies what we believe to be the essential physics controlling ignition in a PEM fuel cell. Water, the reaction product in the PEM fuel cell, autocatalytically accelerates the reaction rate by enhancing proton transport through the PEM. This is analogous to the Arrhenius temperature-based rate acceleration due to the heat produced by an exothermic reaction. We modify the established textbook analysis of heat autocatalyticity in a CSTR (Aris, 1965; Perlmutter, 1972; Schmitz, 1975; Uppal et al., 1974; van Heerden, 1953) to present water management autocatalyticity in a STR-PEM fuel cell. Steady states arise at the intersection of a (linear) water removal curve and a (sigmoidal) water production curve.

Having established the autocatalyticity analogy between the exothermic CSTR (Aris, 1965) and our STR-PEM fuel cell, we study parametric and dynamic operation of the STR-PEM fuel cell with our model. The fuel cell literature contains extensive anecdotal reports that PEM fuel cells only operate when sufficient water is present in the membrane. Our analysis helps elucidate the role of *critical initial* membrane water content for ignition; the same tools can help quantify *critical inlet stream humidity*.

We demonstrate how the single STR-PEM fuel cell can be experimentally connected in series to mimic more conventional PEM fuel cells in Chapter 5. We introduce a segmented anode parallel channel fuel cell as an approximation of the tanks in series fuel cell. With this design, the cell current along the flow channels can be measured, giving a

better idea of which portions of the fuel cell generate more current while allowing us to observe ignition fronts in the cell.

In Chapter 6, we present a modified version of our initial STR-PEM fuel cell model that incorporates key mass transport processes to capture flooding effects in the cathode side catalyst/gas diffusion layer. We have employed our one-dimensional stirred tank reactor model as a building block to model more complex flow geometries via a "tanks-in-series" approach. This methodology provides a simplified straightforward approach to examine dynamics of PEM fuel cells. We have bypassed the more complex gas diffusion layer models to be able to handle dynamics (Jeng et al., 2004; Lin et al., 2004; Pasaogullari and Wang, 2004).

Chapter 2

A Brief Background of PEM Fuel Cells

Ever since the introduction of the polymer electrolyte membrane (PEM) fuel cell by William Grubb (Grubb and Niedrach, 1960), researchers have been striving to incorporate the PEM fuel cell technology into newer applications. This chapter begins with an overview of the PEM, followed by a brief background on PEM fuel cells. A description of current fuel cell modeling efforts is presented at the end of this chapter.

2.1 The Polymer Electrolyte Membrane (PEM)

The PEM is a low density material with a relatively high mechanical strength, making it suitable as an ion conductive gas barrier in fuel cells. The PEM exhibits desirable levels of oxygen solubility and proton conductivity while maintaining chemical stability (Srinivasan et al., 1993). PEMs have to operate at low temperatures to prevent membrane dehydration since dry membranes exhibit decreased conductivity (Thampan et al., 2000; Yang, 2003; Yang et al., 2004). Although there is interest in developing thinner membranes for improved cell performance, this benefit is offset by the increased like-

lihood of reactant gas cross diffusion (Watkins, 1993) in addition to a loss of mechanical strength.

DuPont's introduction of a perfluorosulfonic-acid membrane known as Nafion provided a significant improvement to previous hydrocarbon based membranes. Early membranes consisted of polystyrene-divinylbenzene sulfonic acid crosslinked with an inert fluorocarbon film. The C-H bonds in these early membranes had a tendency to degrade oxidatively, shortening the polymer lifetime in an operating fuel cell (Perry and Fuller, 2002). As illustrated in Figure 2.1, Nafion differs from other membranes because of its Teflon-like backbone. Nafion's inert properties in harsh conditions such as strong acids or bases make it a suitable membrane in most applications. In a PEM fuel cell, the Nafion membrane acts as a barrier to anions, allowing only the transport of cations (protons).

There are two well known models of the Nafion structure, one by Gierke and another by Yeager. In the Gierke model, the ionic groups in Nafion aggregate and form spherical clusters (connected by channels) that can swell with water (Eisenberg, 1970; Gierke et al., 1981; Hsu and Gierke, 1982). Yeager offers a different view, suggesting that Nafion consists of three different regions: a fluorocarbon phase, interfacial regions, and ionic clusters (Yeager and Steck, 1981). Both models support the existence of ionic clusters that have been shown to play an important role in the membrane water uptake. Zawodzinski et al. showed that the membrane water uptake depends on the drying method due to the ionic cluster reorganization during drying (Zawodzinski et al., 1993).

The membrane's ability to absorb water is critical because proton conduction can only occur when percolation pathways through the membrane are established. Therefore,

as mentioned previously, operating a PEM fuel cell at elevated temperatures will dry out the membrane and result in decreased proton conductivity.

2.2 The PEM Fuel Cell and its Components

A typical PEM fuel cell consists of the anode, cathode, and the membrane electrolyte. Both electrodes contain platinum deposits to catalyze the reactions. Hydrogen fed into the anode compartment is broken down into protons and electrons. The protons are transported across the membrane to the cathode side, while the electrons travel via an external electrical circuit to the cathode. At the cathode, hydrogen and oxygen react to form water. A schematic of the PEM fuel cell is shown in Figure 2.2.

Several factors that limit fuel cell performance include mass transfer limitations, CO poisoning, and catalyst type. Mass transfer limitations arise from the transport of reactants to the electrodes in addition to the transport of protons across the membrane. Proton transport is only feasible when the membrane is sufficiently hydrated. As stated previously, a thinner membrane or a more ion-conductive membrane will enhance proton transport into the cathode compartment.

Carbon monoxide (CO) poisoning at the anode is another concern, especially in platinum catalysts. When a hydrocarbon fuel is converted into the hydrogen anode source through a reforming (2.1) and/or the shift process (2.2), CO in the hydrogen feed is also produced by the reforming reaction and from the reverse water-gas shift reaction. CO molecules adsorb on the catalyst surface and inhibit the adsorption of reactant molecules, resulting in CO poisoning at the anode, especially on platinum catalysts.

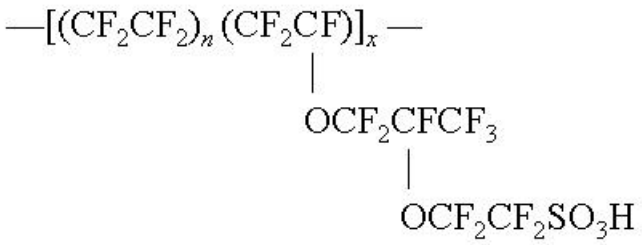

Figure 2.1: The chemical structure of Nafion.

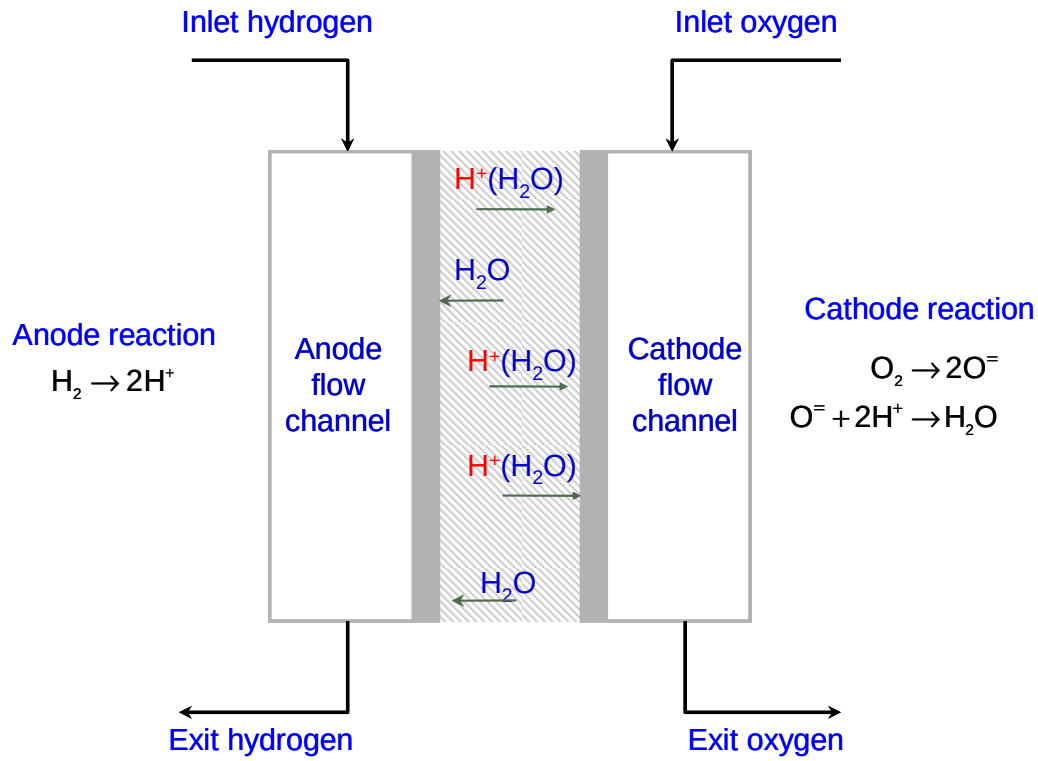

Figure 2.2: Schematic diagram of a typical PEM fuel cell. The membrane must remain sufficiently hydrated for proton transport.

$$CH_4 + H_2O \leftrightarrow CO + 3H_2 \quad (2.1)$$

$$CO + H_2O \leftrightarrow CO_2 + H_2 \quad (2.2)$$

Polarization effects (the loss of cell voltage due to current) are manifest in plots of cell voltage as a function of current density. The polarization curves in Figure 2.3 depict the effect of low CO levels in a PEM fuel cell at 80^0C as presented by Gottesfeld (Gottesfeld and Pafford, 1988). Even low levels of CO significantly decrease the cell voltage, resulting in a smaller power output at a given current density; the presence of CO strongly inhibits fuel cell performance. Fortunately, CO levels may be reduced by injecting low amounts of oxygen into the hydrogen anode feed stream. The added oxygen oxidizes the adsorbed CO to CO_2. However, a direct reaction between hydrogen and oxygen may also occur, leading to a loss of fuel conversion (on the order of several percent).

The choice of catalyst electrode may improve the fuel cell design. Platinum, palladium, and nickel are commonly used metals with desirable electrocatalytic properties. Platinum is preferred over other metals since it most effectively adsorbs hydrogen and oxygen and catalyzes the surface reaction. In PEM fuel cells, nanometer sized Pt catalyst particles are deposited into one side of a porous carbon layer and pressed onto the PEM. The other side of the carbon layer is attached to a carbon fiber paper that provides some structural support to the assembly and controls reactant diffusion toward the electrode.

In the past, one barrier to PEM fuel cell development was the extremely high cost of platinum. However, a major improvement occurred when Raistrick showed that a reduction of platinum loadings in the electrodes was feasible by coating the electrodes

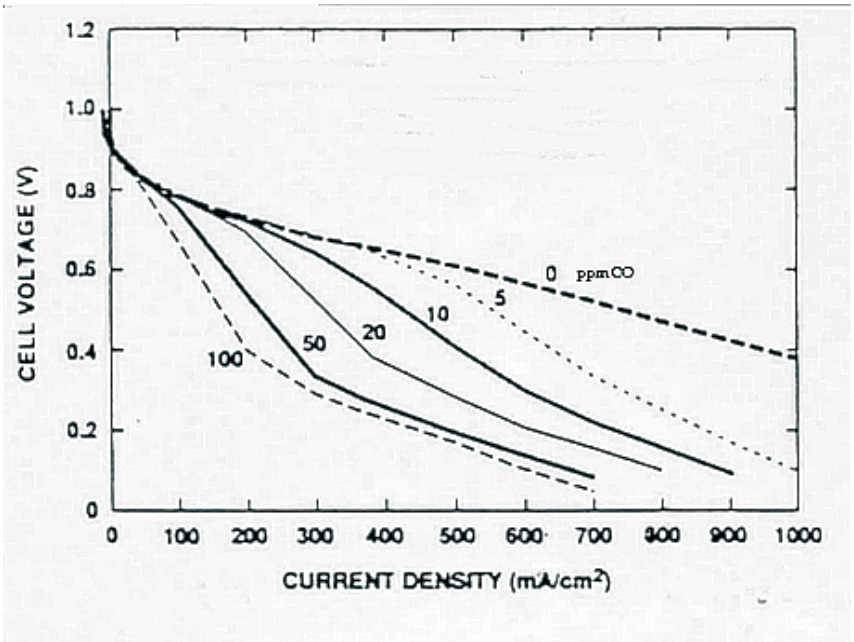

Figure 2.3 Effect of low CO levels in the anode at T = 80^0C. Even ppm levels of CO significantly decrease the cell voltage and result in a smaller power output at a given current density (Gottesfeld and Pafford, 1988).

with the perfluorinated ionomers in a liquid form (Raistrick, 1986). This step resulted in an increased interfacial area since it created a thin layer of the polymer on the catalyst before the hot pressing step. Since Raistrick's important discovery, further refinements in the area of membrane electrode assembly (MEA) preparation followed (Wilson et al., 1993; Wilson and Gottesfeld, 1992). Flooding, which arises due to water condensation in the pores can inhibit reactant diffusion toward the catalyst. The electrode contacting water may be treated with a hydrophobic substance such as Teflon to prevent pore flooding and wetting (Uchida et al., 1995).

2.3 PEM Fuel Cell Modeling Efforts

A fuel cell model is essential in optimizing fuel cell performance. An accurate model will enable predictions of the cell performance under varied operating conditions. Numerical and analytical fuel cell models that incorporate various aspects of heat, mass, and momentum transport characteristics have been proposed in the past. Most modeling efforts have focused on the various parts of the PEM fuel cell which include the gas diffusion layer / gas flow channel (reactant transport), the polymer electrolyte membrane (proton and water transport), and the catalyst layer (reaction site). Typical PEM fuel cell models consist of transport equations for these respective parts and may include water transport and heat effects.

Bernardi and Verbrugge initially developed a half-cell one-dimensional model of a cathode gas diffusion electrode bonded to a fully hydrated polymer electrolyte membrane under isothermal conditions (Bernardi and Verbrugge, 1991). As depicted in Figure 2.4, the modeled system consists of the membrane region, an active catalyst layer, and a gas

diffusion layer. Corresponding transport equations were written for each respective layer. Bernardi and Verbrugge later extended this model to a complete PEM fuel cell model where they addressed limiting cell performance factors and mechanisms of species transport within the PEM fuel cell (Bernardi and Verbrugge, 1992). Their work showed that the membrane thickness and oxygen transport through the cathode to reaction sites affect cell performance. Lower cell potentials were measured for thicker membranes while higher limiting currents were obtained for more porous cathode electrodes. Prior to the published work by Bernardi and Verbrugge mentioned above, Bernardi also proposed a PEM fuel cell model based on gas phase transport which identified operating conditions to ensure a water balance in the cell (Bernardi, 1990).

Elsewhere, Springer et al. presented a one dimensional steady-state model for a complete PEM fuel cell with a Nafion membrane (Springer et al., 1991). This model was used to address the issues of transport through porous electrodes and transport through the membrane electrolyte by using calculated diffusivities (corrected for porosity) and experimentally determined transport parameters. The model proposed by Springer et al. does not require a fully hydrated membrane and thus differs from Bernardi and Verbrugge's model.

When the protons migrate toward the cathode, water molecules are dragged by osmotic action which creates a gradient in water concentration within the membrane, depleting the anode side of water. Typically, water produced in the cathode reaction diffuses back to the anode and the membrane remains hydrated. However, at high current densities, water drag is more severe and it complicates the PEM fuel cell operation. In the Springer model, water distribution in the fuel cell at steady-state is calculated by

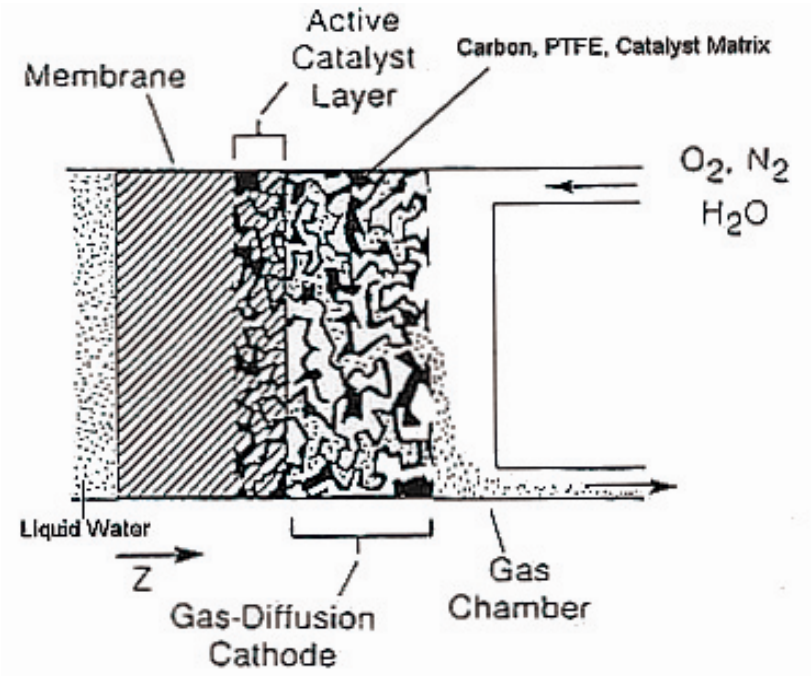

Figure 2.4: Schematic diagram of a gas diffusion electrode. The modeled system consists of the membrane region, an active catalyst layer, and a gas diffusion layer (Bernardi and Verbrugge, 1992).

accounting for water flow in the electrodes, membrane, and reactant inlets. Further refinements to incorporate interfacial kinetics at the catalyst/membrane interface, gas transport, and conductivity issues were later proposed (Springer et al., 1993).

Two dimensional models of PEM fuel cells that address water management issues have also been developed by several groups (Fuller and Newman, 1993; Gurau et al., 1998; Hsing and Futerko, 2000; Nguyen and White, 1993). Fuller and Newman used concentrated solution theory to model water transport and heat management in a two-dimensional membrane electrode assembly (Fuller and Newman, 1993). Nguyen and White focused on heat and mass transport along the gas flow channel while accounting for water evaporation and condensation (Nguyen and White, 1993). In this work, they obtained the temperature, water, gas and current density distribution in the gas flow channels. This model did not account for the water variation across the membrane. The parameters were determined from the anode side water content.

Gurau's group sectioned the PEM fuel cell into three domains according to the phases of the fluid (Gurau et al., 1998). The model was developed to closely describe the species concentration distribution along the gas channel-gas diffusion-catalyst layer domain. This could only be accomplished by introducing two dimensional momentum equations in the coupled domain. The transport, electrochemical, and current density equations were then solved numerically to obtain polarization curves under various operating conditions. Hsing and Futerko presented a finite-element based model of coupled fluid flow, mass transport, and electrochemistry (Hsing and Futerko, 2000). This model was developed to operate without prior external humidification of the reactant gas. In a later study, Gurau derived an analytical solution of a half-cell model for PEM fuel cells.

The ability to identify trends through functions instead of sets of numerical data was a main incentive for developing the one-dimensional analytical model (Gurau et al., 2000).

Besides the transport models described above, electrochemical PEM fuel cell models have been proposed. Mann et al. focused on developing a generalized steady-state electrochemical model for a PEM fuel cell (Mann et al., 2000). Previous fuel cell models were not applicable to cells with varying characteristics and dimensions. Therefore, Mann's group developed a generic model that accepted operating variables and cell parameters such as active area and membrane thickness. To account for the decrease in the membrane's water-carrying capacity over time, the model also included a membrane aging term. The model was only capable of predicting cell performance for an idealized PEM cell utilizing Nafion.

In addition to other complete fuel cell models (Bevers et al., 1997; Pisani et al., 2002; Springer et al., 2001; Standaert et al., 1996; Thirumalai and White, 1997), there also exists a number of models that focus on water/proton transport within the membrane (Janssen, 2001; Okada et al., 1998; Paddison, 2001), membrane/catalyst layer interface (Eikerling and Kornyshev, 1998; Lin et al., 2004), and fuel cell stacks/systems (Amphlett et al., 1994; Amphlett et al., 1998). Although many proposed models are capable of predicting experimental fuel cell performance, they are either too complicated or oversimplified. Most models can only predict the cell performance over limited operating conditions. Therefore, the models do not yield an adequate fit of experimental data over all conditions. Many models concentrate on either the entire cell or a half-cell that encompasses the membrane layer through the gas channel. Focusing on such a large region makes it difficult to model the effects of various parameters within each layer.

Chapter 3

The Differential PEM Fuel Cell

Experimentally constructing and modeling the PEM fuel cell as a differential reactor allows us to avoid the intricate details of water and proton transport through the PEM, electron transfer reactions at the electrodes, and transport through various layers of the fuel cell. Most importantly, spatial and temporal variations are uncoupled in a differential PEM fuel cell, enabling us to study the dynamics. We propose here a reaction engineering perspective of the PEM fuel cell as a differential reactor and describe the rationale behind its design.

3.1 The Stirred Tank Reactor PEM Fuel Cell

PEM fuel cells consist of two graphite flow channels that sandwich a membrane electrode assembly (MEA). Reactant gases are fed into the graphite flow channels, better known as serpentine flow channels, typically contain tortuous pathways. Due to these zigzag pathways, gradients in reactant concentration in both the anode and cathode flow channels arise, causing a non-uniform current distribution over the membrane. While it

is feasible to track the current evolution over the membrane in both space and time, it would be easier if one can focus on a differential element as illustrated in Figure 3.1. Concentrating on such a small element allows one to assume that the reactant concentrations are uniform in the anode and cathode chambers and that the only composition gradient is transverse to the membrane. These well mixed chambers are the basis of the *stirred tank reactor (STR) PEM fuel cell* (Benziger et al., 2004).

The characteristic dispersion number, a ratio of diffusive transport to convective transport, provides a measure of mixing inside the flow channels. A characteristic dispersion number (D/uL) much larger than 1 indicates that diffusive transport dominates and the gas phase is homogenous. Here, D is the diffusivity, L is the flow channel length and u is the gas velocity. The GlobeTech serpentine flow field shown in Figure 3.2 contains channels that are 100 mm in length with a cross sectional flow channel area of 1 mm^2 over an MEA area of 5 cm^2. In contrast, the flow channels in the STR-PEM fuel cell are 14 mm in length with a cross section of 4 mm^2 over a much smaller MEA area of 1 cm^2. The dispersion number for the GlobeTech fuel cell producing 1.4 A/cm^2 at 100% H_2 utilization with flow rates of 50 mL/min is less than 0.2. In comparison, for the STR-PEM fuel cell producing the same current density with flow rates of 10 mL/min or less, the dispersion number is greater than 1. Convective mixing in the serpentine flow field thus creates compositional gradients along the flow channels.

Unlike typical PEM fuel cells, the STR-PEM fuel cell does not contain the tortuous serpentine flow channels and it is operated at flow rates such that the gas phases in the anode and cathode chambers remain well mixed (long residence times). The homogenous gas phase in the anode and cathode reduces the fuel cell to a one-dimensional

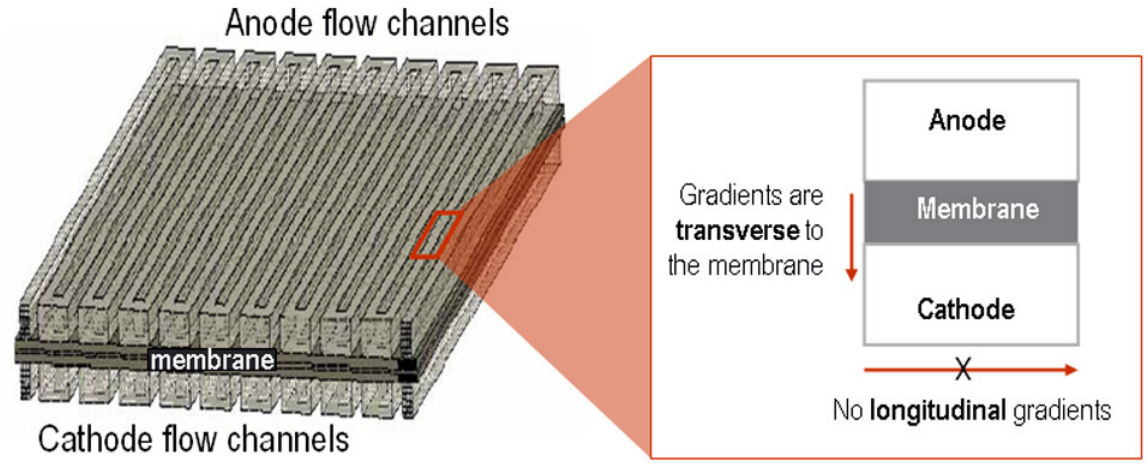

Figure 3.1: Visualizing the differential PEM fuel cell as a differential element from a serpentine gas flow channel PEM fuel cell. The schematic on the right is a blow up of the boxed element. In a serpentine type PEM fuel cell, variations in current density occur over the membrane. However, only gradients transverse to the membrane occur in a differential fuel cell.

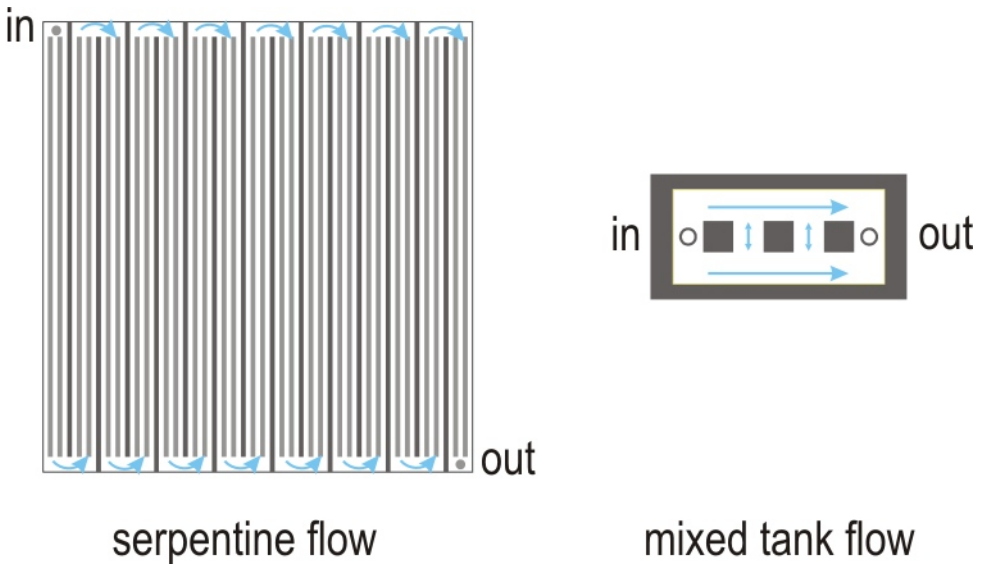

Figure 3.2: Comparing the serpentine flow channel to the mixed tank flow channel. In a typical PEM fuel cell such as the GlobeTech fuel cell shown on the left, reactant gases are passed through serpentine pathways that cover an area of 5 cm^2. Convective transport dominates in the serpentine channels, resulting in compositional gradients between the inlet and exit streams over the membrane. In contrast, for the STR-PEM fuel cell, the reactant gases are more homogenous in the open plenum area that covers only 1 cm^2. The dark areas in the figure are the raised portions of the graphite plate that contact the MEA whereas the light colored regions are open spaces available for gas flow.

system which also significantly simplifies the data analysis. This unique chemical engineering perspective of the PEM fuel cell as a stirred tank offers an important advantage in studying the dynamics. We can address issues of fuel cell startup from different initial conditions and whether or not the system parameters affect the fuel cell startup. Also, we can study how the fuel cell responds to changes in the system parameters such as the load, temperature, or reactant flow rates.

3.2 Experimental Setup

The first one-dimensional STR-PEM fuel cell system was constructed by previous group members (Moxley et al., 2003) and we have also developed a mathematical model of it (presented in the following chapter). There are four main parameters which an operator can control: heat input to the cell (temperature), the variable external load resistance, hydrogen flow rate into the anode, and oxygen flow rate into the cathode. The STR-PEM fuel cell is connected to the variable load resistance. The current through and the voltage drop across this load are measured. The experimental setup is schematically illustrated in Figure 3.3.

The graphite plates with gas plenum volumes (V) of 0.2 mL contain machined pillars that are matched between the two plates to ensure that pressure is applied uniformly to the MEA. Hydrogen and oxygen gases are controlled through mass flow controllers and fed at flow rates (F_{in}) between 1 and 10 mL/min. The residence times (V/F_{in}) of 1.2 to 12 s are longer than the characteristic diffusion times ($V^{2/3}/D$) of 0.3 to 1 s. As mentioned previously, the residence times in the anode and cathode chambers are sufficiently long so that the reactant gases remain well mixed.

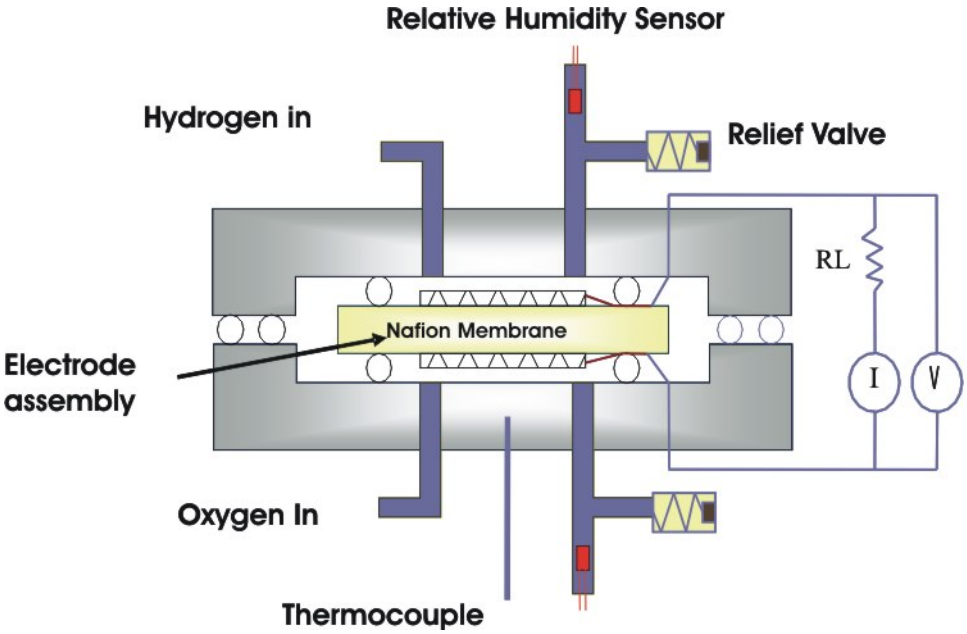

Figure 3.3: A schematic of the STR-PEM fuel cell experimental setup.
The STR-PEM fuel cell consists of two graphite plates that are sandwiching a membrane electrode assembly. The gas volumes above (anode chamber) and below the membrane (cathode chamber) are well mixed. The controllable parameters include the temperature, variable load resistance, and inlet reactant flow rates.

The MEA consists of a Nafion 115 membrane with an area of 1 cm^2 that is hot pressed between 2 E-tek electrodes with a catalyst loading of 0.4 mg Pt/cm^2. The E-tek electrodes are carbon cloths that come coated with a Pt/C catalyst. The electrodes are impregnated with a 5% Nafion solution to a loading of 0.6 mg/cm^2 before hot pressing with a 2200 lbf (9.77 kN) at 130°C. The MEA is then placed between two silicon rubber gaskets before it is sandwiched between the graphite plates. Copper sheets are pressed against the graphite plates with wires that attach to the external variable load resistor. The graphite plates are placed in between aluminum blocks that are fitted with cartridge heaters connected to a temperature controller.

A 10 turn 0 to 20 Ω potentiometer is used as the variable external load resistor. Current through the load resistor is also passed through a 0.2 Ω sensing resistor and an instrumentation amplifier (Analog Devices AMP02) amplifies the differential voltage across the sensing resistor by a factor of 100. The current is read directly by a data acquisition board.

3.3 System Variables and Parameters

It is important to identify the system variables from the system parameters before proceeding to the experimental results. The *system variables* in the STR-PEM fuel cell system are quantities that describe the local state of the fuel cell and these quantities cannot be directly controlled. However, the *system parameters* are quantities that an operator can manually change based on his/her discretion. For instance, one can regulate the amount of water fed into the fuel cell but the membrane water content is a measurable quantity that cannot be directly controlled. The membrane water content (as indicated by

the membrane water activity a_w) depends on many factors including the rate of water production (as indicated by the current), the inlet water content (water fed), and exiting water content (water removed), as well as the cell temperature. Since the operator cannot *directly* fix the membrane water content, it is an example of a system variable. We will later show that the membrane water content is an important variable that is responsible for the unique dynamics characteristic of the STR-PEM fuel cell.

We have chosen to operate the STR-PEM fuel cell under a fixed external load resistance (a system parameter) and we let the voltage and the current evolve. The voltage and the current are system variables that depend on the membrane water content. Since we neither fix the voltage nor the current, the STR-PEM fuel cell is not potentiostatically or galvanostatically regulated. We have chosen to operate the fuel cell this way so that we may study the autonomous response to the four operating parameters. If we choose to control the voltage or current, implementing a potentiostatic or galvanostatic control loop on the fuel cell system would prevent us from extracting information pertaining to the kinetics of the operating fuel cell.

The STR-PEM fuel cell can be schematically depicted as two reactors (anode and cathode) that are connected by two valves as shown in Figure 3.4. The two valves represent the external load resistance (R_L, a system parameter) that regulates the electron flow across the external circuit and the membrane resistance (R_M, a system variable) that regulates the proton flow across the membrane. R_M is not directly controllable because it has been shown to be strongly dependent on the water content in the membrane (membrane water activity) (Yang, 2003). In addition to R_L, inputs to the fuel cell such as the feed composition and feed flow rates are system parameters. On the other hand, the

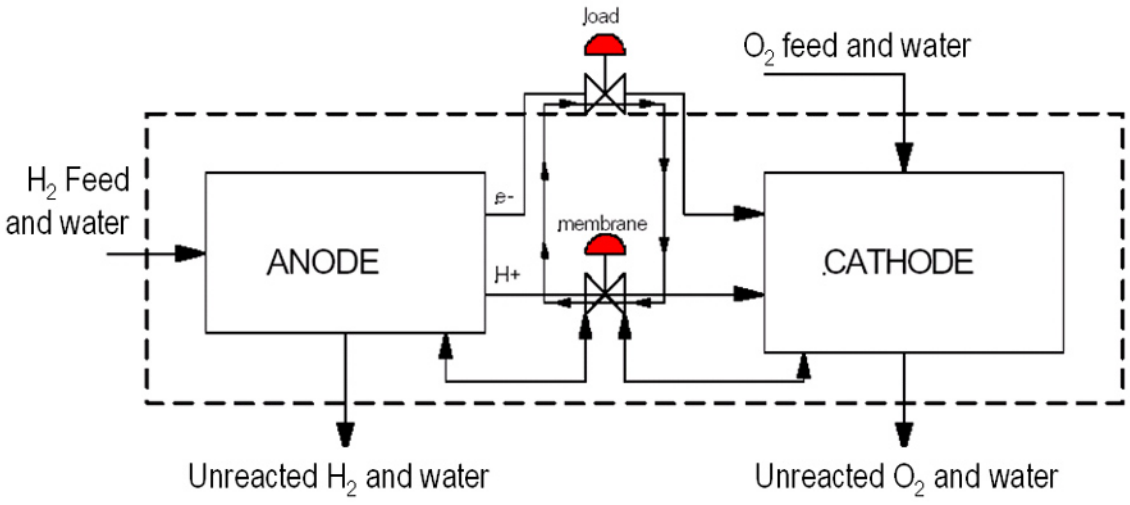

Figure 3.4: Conceptual reactor coupling in the STR-PEM fuel cell. Inputs that lie outside of the dashed box are directly controllable operating parameters. The external load resistance and the membrane resistance act as valves that regulate the electron flow across the external circuit and the proton flow across the membrane respectively.

exiting flow rates and effluent composition are system variables since these quantities depend on the mass balance between reaction and production in the fuel cell. An operator can only control the parameters that lie outside of the dashed box which represents the physical boundary of the fuel cell. Note that the two regulators are connected in series, indicating that the total resistance is the sum of both resistances.

From the electrical circuit equivalent of the fuel cell as shown in Figure 3.5, the current is defined according to Ohm's law as:

$$i = \frac{V}{R_M + R_L} \tag{3.1}$$

Therefore any increase in R_M or R_L will result in a lower overall current. A list of the system parameters and variables is shown in Table 3.1.

3.4 Experimental Results

3.4.1 Fuel Cell Startup

We are particularly interested in the fuel cell startup behavior from different initial conditions. In a previous experiment, the importance of an optimum level of water in the fuel cell was illustrated (Benziger et al., 2004). The membrane was first dried by flowing dry nitrogen gas through the anode chamber and dry oxygen gas through the cathode chamber at flow rates of 100 mL/min for 12 hrs while maintaining the cell temperature at 60°C. The membrane was then preconditioned to a fixed humidification level by shutting off the oxygen flow to the cathode and passing 10 mL/min of nitrogen gas through a water bubbler (equilibrated at room temperature) before it was fed into the anode chamber. The anode effluent relative humidity was measured as a function of time to

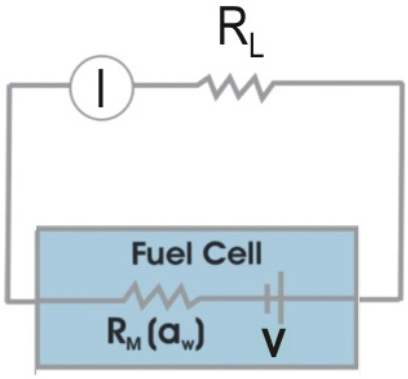

Figure 3.5: Equivalent electrical circuit for the PEM fuel cell. Both resistances are connected electrically in series so that any increase in either resistance will lead to a decreased cell current. The membrane resistance is a strong function of the membrane water content (activity).

System Variables	System Parameters
Effluent flow rates	Reactant feed flow rates
Effluent composition	Reactant feed composition
Gas relative humidity	Membrane material
Cell temperature	Heat Input
Cell voltage	Cell construction
Cell current	Electrode structure
Membrane water content	External Load Resistance

Table 3.1: Relevant system variables and system parameters for the STR-PEM the fuel cell.

determine the water uptake into the membrane. When the membrane reached the desired humidification level, the nitrogen flow was turned off and the dry hydrogen flow into the anode and dry oxygen flow into the cathode (both at 10 mL/min) were resumed. The current through the 5 Ω external load resistor was monitored and recorded over time.

The water uptake (denoted by λ) expressed as the number of water molecules per membrane sulfonic acid group (N_{H20}/N_{SO3}) is a measure of the water content in the membrane. From Figure 3.6, it can be seen that depending on the initial λ value, the fuel cell current ignites or extinguishes as indicated. For small λ values less than or equal to 1.4, the fuel cell extinguishes over time but for values greater than or equal to 1.6, the fuel cell ignites. If the membrane does not contain enough water, the membrane resistance to proton flow is large, causing a low rate of water production. When the water production is less than the water removal, the membrane continues to dry and the fuel cell eventually reaches the extinguished state.

In a separate experiment, the fuel cell startup with different external load resistances was observed. Starting with the same initial membrane water content, the fuel cell was operated at 60°C and reactant flow rates of 10 mL/min with external load resistances of 20 Ω and 5 Ω. As shown in Figure 3.7, at the larger load of 20 Ω, the current decreased to the extinguished state. In contrast, when the fuel cell was operated at a lower load of 5 Ω, the current increased from about 20 mA to 150 mA. This finding illustrates that the external load resistance can also affect the final steady state fuel cell current. As stated in Equation 3.1, the current depends on the sum of the external load resistance and the membrane resistance because they are electrically connected in series.

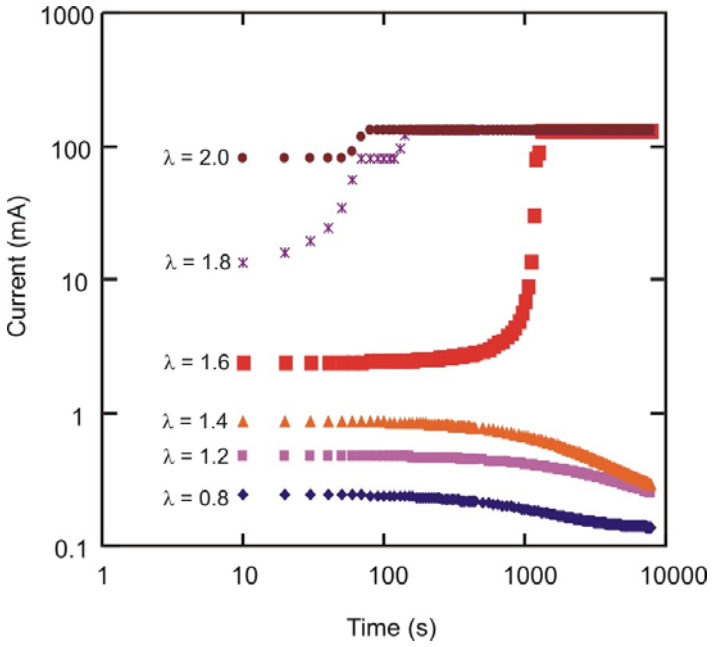

Figure 3.6: Fuel cell startup from different initial water contents. For small λ, the membrane resistance to proton flow is large and the fuel cell current extinguishes. But for large enough λ values, the fuel cell current ignites (Moxley et al., 2003).

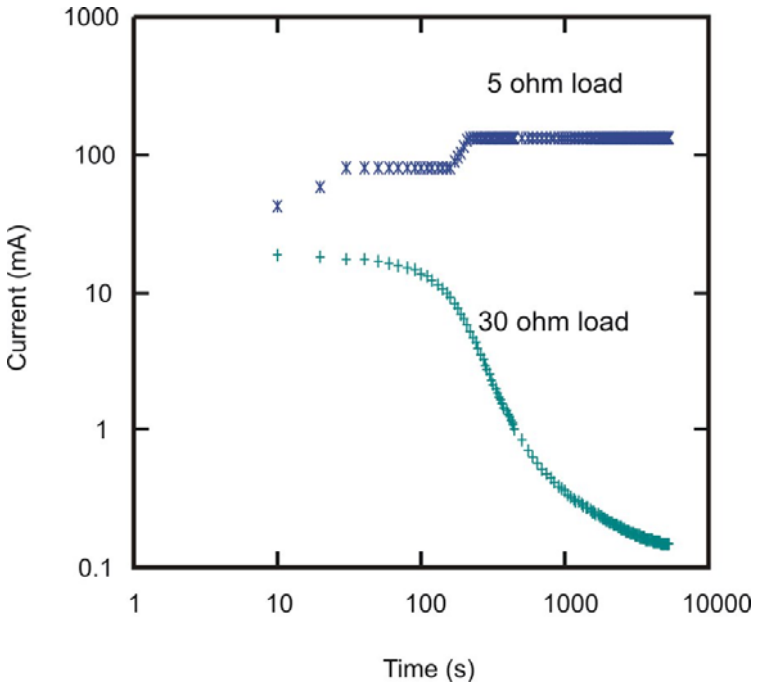

Figure 3.7: Fuel cell startup with different load resistances. The larger external load resistance of 30 Ω suppresses the water production rates, resulting in a drier membrane which eventually leads to the current extinguishing. In contrast, the fuel cell starting up from 5 Ω is able to balance the water removal and water production rates and ultimately reaches the ignited current steady state (Benziger et al., 2004).

Besides the initial membrane water content and external load resistance, the inlet reactant humidification levels also affect startup. To test the humidification effects, the membrane was first dehydrated by flowing dry gases into the anode and cathode for 12 hours at 60°C. A dry oxygen supply was then fed to the cathode while the hydrogen feed was passed through a bubbler operating at 25°C. Both reactant feeds were set to 10 mL/min. Figure 3.8 shows that increasing the humidifier temperature from 25°C to 30°C led to the fuel cell current igniting to about 80 mA after 1000 s. When the anode stream was further humidified by increasing the bubbler temperature to 35°C, ignition occurred even earlier and the high current steady state was reached after about only 300 s. From this result, we see that while the feed humidification levels affect the time to ignition, the final steady state current depends predominantly on the membrane water content.

3.4.2 Response to Changes in Operating Parameters

A real fuel cell operating in practical applications will necessarily respond to various heating conditions, external load demands, and fuel supply limitations. As an initial step, the fuel cell response to changes in several operating parameters was studied to get a better insight of the fuel cell dynamics. The fuel cell response to a change in the cell temperature, external load resistance, and hydrogen flow rate was monitored.

In one experiment, the reactant flow rates and the external load were held at 10 mL/min and 2 Ω respectively and the voltage, current, and effluent relative humidity response to an increase in the fuel cell temperature from 70°C to 90°C were observed. The cell temperature reached 90°C in about 200 s but the cell current took slightly longer to equilibrate. The current response as depicted in Figure 3.9 is seen to initially decrease

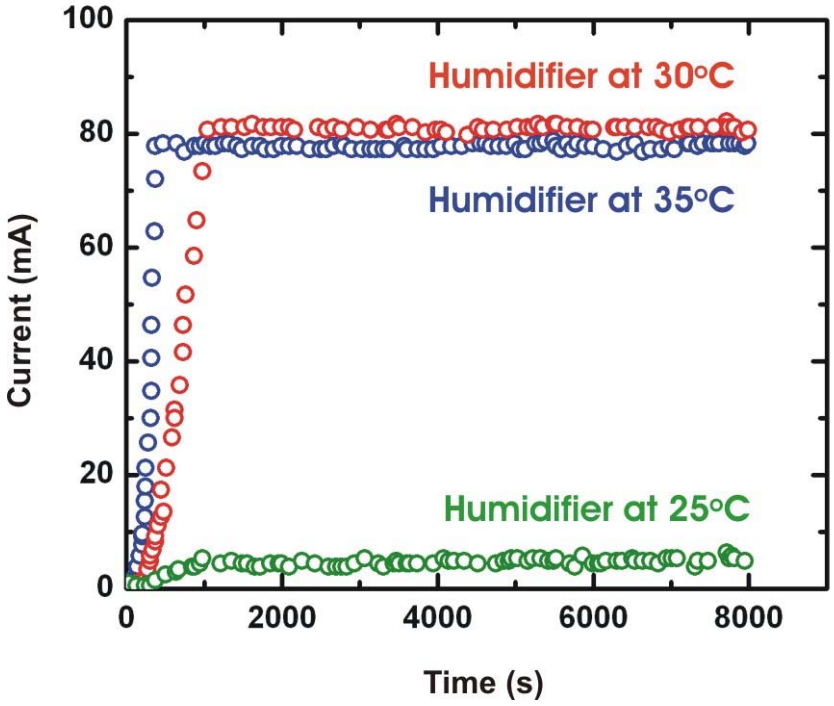

Figure 3.8: Startup from different humidifier temperatures. While feeding a dry oxygen supply to the cathode, the hydrogen feed was passed through a bubbler (held at different temperatures) before being fed into the anode. Heating the bubbler temperature to 30°C increased the water content in the anode feed, leading to the current igniting. Further humidification (bubbler temperature at 35°C) shortened the ignition time.

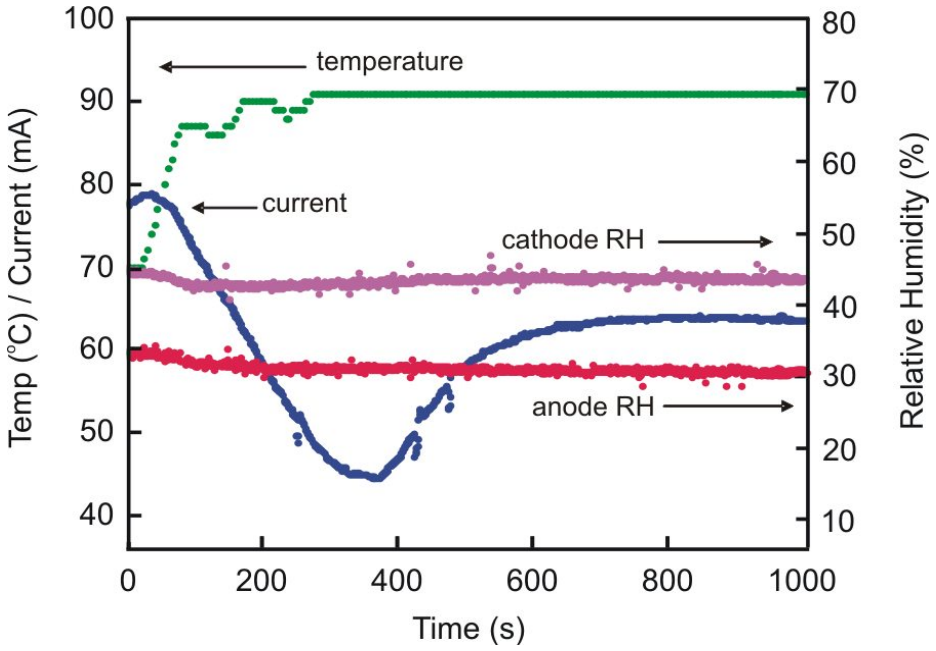

Figure 3.9: Fuel cell response to a step increase in temperature from 70°C to 90°C with the external load resistance at 2 Ω and reactant feed flow rates of 10 mL/min. A decrease in fuel cell current was observed as a result of the larger rate of water removal.

with heating from 78 mA to 45 mA but subsequently equilibrates at 65 mA. The heating process increased the water vapor pressure which resulted in a greater rate of water removal. The early decline in current is thus attributed to the water evaporation from the membrane which was initially faster than the diffusion of water in the membrane. Over time, water in the membrane and water in the membrane-electrode interfaces equilibrate and a final steady state is reached. The effluent cathode and anode relative humidities decrease with the higher temperature as well.

Cooling the fuel cell from 90°C to 70°C was accompanied by an increase in cell current from 61 mA to 83 mA as shown in Figure 3.10. Note that the cooling process took longer than the heating since it is a passive process. Both the cathode and anode relative humidities increased with the temperature drop, indicating that less water is removed due to a decrease in water vapor pressure. The lower rate of water removal led to an increased membrane water activity. As mentioned previously, the membrane resistance is lower at a larger membrane water activity, resulting in a larger fuel cell current. For both the heating and cooling processes, the complex coupling between the water production at the cathode and water transport across the membrane results in differences in the anode and cathode relative humidity responses.

The fuel cell response to a change in the external load resistance was observed by decreasing the external load resistance from 20 Ω to 7 Ω. Prior to this change, the fuel cell was set to operate at 80°C with 5 mL/min of H_2 flow to the anode and 10 mL/min of O_2 flow to the cathode. From Figure 3.11, it can be seen that the dynamic response to the decrease in the load resistance was rather unusual. The cell current immediately increased from 25 mA to about 76 mA before it gradually decayed to 65 mA. Despite

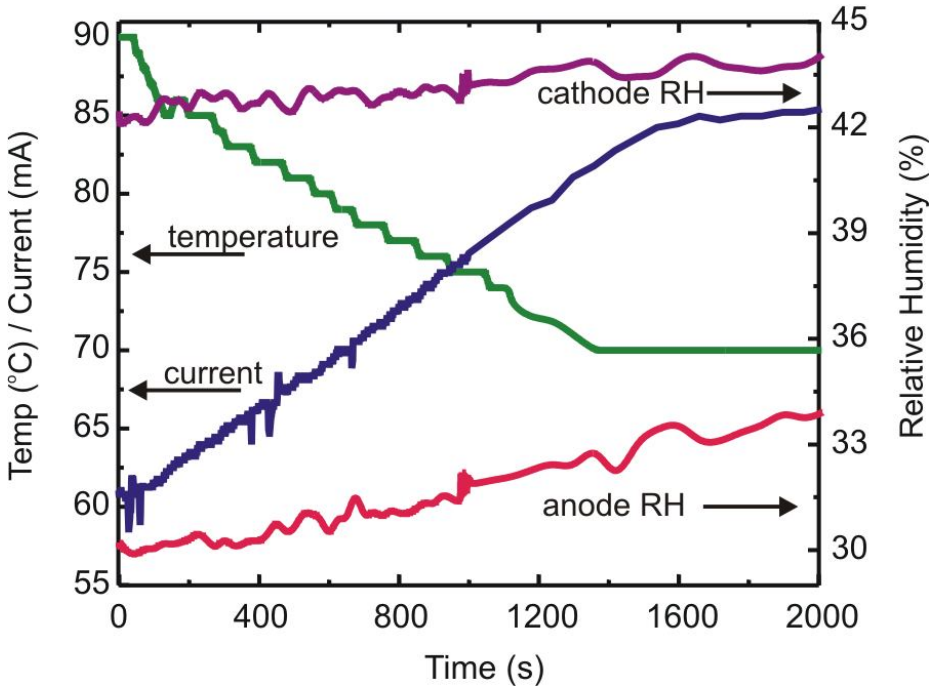

Figure 3.10: Fuel cell response to cooling from 90°C to 70°C with the external load resistance at 2 Ω and reactant feed flow rates of 10 mL/min. Less water is removed at the lower temperature, leading to a lower membrane resistance which resulted in an increase in the cell current.

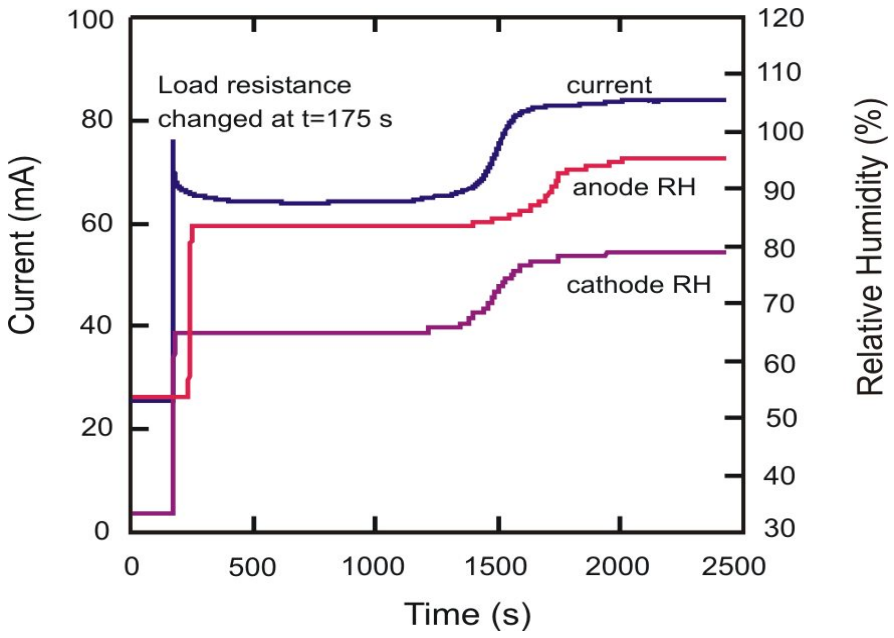

Figure 3.11: Dynamic response to an increase in the external load resistance from 20 Ω to 7 Ω at a fixed temperature of 80°C with 5 mL/min of H_2 flow to the anode and 10 mL/min of O_2 flow to the cathode. The cell current first rises rapidly before reaching a plateau at 65 mA but subsequently makes another jump to 84 mA after 1500 s. The cathode relative humidity tracks the current while the anode relative humidity lags that of the cathode.

leveling out at 65 mA, the cell current subsequently jumped to 84 mA after 1500 s (without any change in the operating parameters). The anode relative humidity response is seen to lag that of the cathode relative humidity response by about 100 s.

To observe the dynamic response to a change in the hydrogen feed, the fuel cell was first operated at 80°C and 2 Ω with 10 mL/min of O_2 flow to the cathode and 1 mL/min of H_2 flow to the anode for 12 hours. The H_2 flow was then increased up to 10 mL/min and the current, voltage, and effluent relative humidity responses were tracked. Immediately following the change in H_2 flow, as shown in Figure 3.12, the current increased from 3 to 80 mA over 10 s. The current kept increasing but at a slower rate to 100 mA, and subsequently jumped to 145 mA after 650 s.

The initial increase in current is caused by the sudden increase in the hydrogen supply. After that initial response, the fuel cell took some time to adjust to the increased water production rates and equilibrated to the plateau. The surprising jump in current is most likely the result of the balance between water transport in the membrane and the mechanical stress relaxation. We believe that the membrane swells with the increased water production and improves the membrane electrode contact, thereby resulting in a sudden jump in the current.

The cathode relative humidity is seen to track the current (by about 10 seconds) while the anode relative humidity tracks the cathode relative humidity. As the current increased slowly to 100 mA, the cathode relative humidity increased significantly as well from 45% to 85% but slowed down when then current jumped. The anode relative humidity increased by 10% from 35%. These increased effluent relative humidities are the result of the increased water production rates.

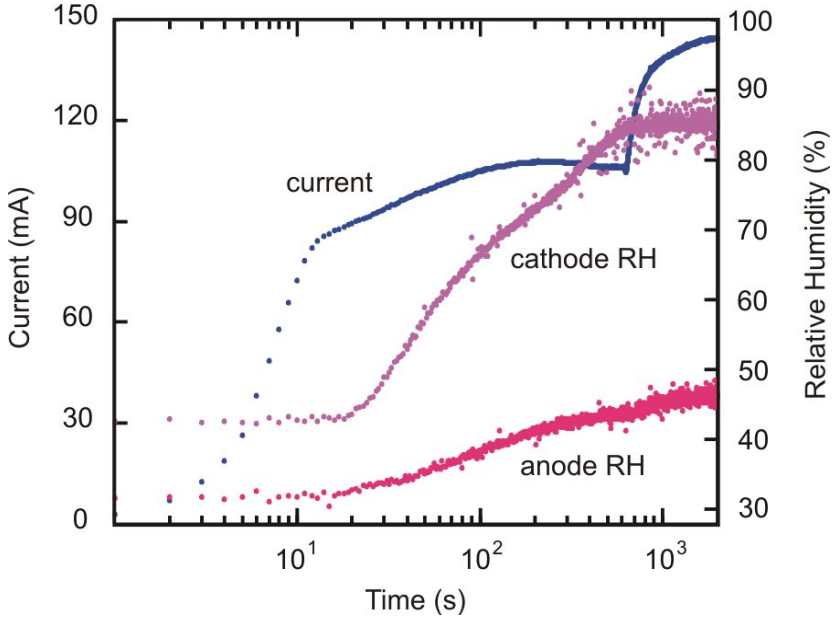

Figure 3.12: Dynamic response to a change in the hydrogen feed flow rate from 1 to 10 mL/min for a fuel cell equilibrated at 80°C, 2 Ω external load, 10 mL/min of oxygen fed to the cathode, and 1 mL/min of hydrogen supplied to the anode. Following the initial increase in current, the fuel cell equilibrated to the new conditions over 600 seconds.

3.4.3

Characteristic Times

From the observed responses to changes in operating parameters, it is evident that there are characteristic times associated with physical processes in the fuel cell. Contrary to the common assumption that PEM fuel cell response times are almost instantaneous, we have shown that the response times can take as long as hundreds of seconds. Several characteristic time constants can be derived for the fuel cell and they are listed in Table 3.2 along with order of magnitude estimates based on approximate values for the physical parameters. These time constants include the characteristic reaction time τ_1, the time for gas phase transport across the diffusion layer to the membrane electrode interface τ_2, the time for water produced in the cathode side to diffuse across the membrane to the anode side τ_3, and the time it takes the membrane to absorb the water produced τ_4.

From the fuel cell response to a change in load alone, the 100 s lag in the anode relative humidity response after the cathode relative humidity is representative of τ_3. It takes on the order of 100 s for water produced in the cathode side to travel across the membrane to the anode and exit with the anode effluent. The characteristic time for water absorption into the membrane is also on the order of 100 s as estimated by the time it takes to saturate a dry membrane with a fuel cell operating at 1 A/cm^2. The time constants and fuel cell response strongly suggest that the membrane is acting as a reservoir for water.

3.4.4

Polarization Curves

Polarization curves were recorded for the fuel cell equilibrated at 80°C and 10 mL/min of reactant flow rates under two different load resistances, 0.2 Ω and 20 Ω respectively. The load resistance was later swept from 0.2 Ω to 20 Ω over a period of 100 s while the current and voltage were recorded and plotted as shown in Figure 3.13. This clearly illustrates that preconditioning the fuel cell under the two load resistances leads to different polarization behavior (attributed to a difference in membrane water activity). The polarization curve for the 20 Ω load represents the low membrane water activity case while that of the 0.2 Ω load represents the high membrane water activity case. A lower activation polarization is observed for the latter since the voltage is larger for smaller currents. However, at larger currents, the lower voltage suggests that water inhibits the transport of oxygen to the cathode and mass transport resistance is dominant. In contrast, for the low membrane water activity case, the mass transport resistance is not as significant.

3.4.5 Autonomous Oscillations

By far the most surprising experimental result is the occurrence of autonomous oscillations in voltage and current for the STR-PEM fuel cell operating under fixed parameters. Despite maintaining the operating temperature, reactant flow rates, and the external load resistance fixed, the cell current oscillated continuously over a day. Even the cathode and anode relative humidities oscillated regularly and in phase with the current. These oscillations were observed under a variety of operating parameters. An example of

Time	Description	Approximate value
τ_1	Characteristic reaction time	0.1 s
τ_2	Characteristic diffusion time across the gas diffusion layer	0.1 s
τ_3	Characteristic diffusion time for water produced to cross the membrane	100 s
τ_4	Characteristic time for water absorption in the membrane	100 s

Table 3.2: Characteristic time constants that are associated with various physical processes occurring in the PEM fuel cell

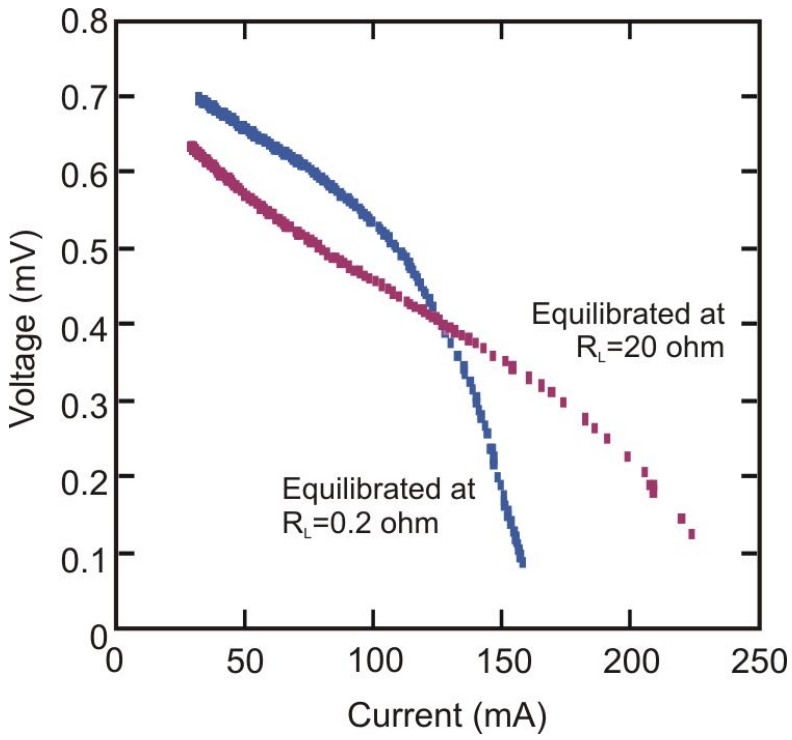

Figure 3.13: Polarization curves taken after the fuel cell was equilibrated at 80°C with reactant feed flow rates of 10 mL/min and load resistances of 20 Ω and 0.2 Ω respectively. Preconditioning the fuel cell under different external loads results in different polarization behavior. This is attributed to differences in the membrane water activity.

these autonomous oscillations is shown in Figure 3.14 for a fuel cell operating at 90°C, 0 Ω, 10 mL/min of oxygen, and 5 mL/min of hydrogen.

Changes in the membrane water activity most likely resulted in a mechanical relaxation of the polymer membrane. The oscillations are thus attributed to a strong coupling between the polymer membrane relaxation and membrane electrode interfacial resistance. The sharp jumps in current are brought about by the increased contact between the membrane and the catalyst particles as illustrated in Figure 3.15. The repeated swelling and relaxation give rise to the sustained oscillations. We believe that these unique oscillations are captured in the STR-PEM fuel cell because the spatial variations have been uncoupled from the temporal ones through this novel stirred tank design.

3.5 Summary

We have shown that the reaction engineering perspective of the PEM fuel cell as a stirred tank reactor has led to the discovery of complex fuel cell dynamics, some aspects of which remain to be fully understood. It is the differential view that simplifies the fuel cell to a one dimensional system such that there are no spatial gradients. We have also established that the membrane is a *reservoir* for water. When any operating parameter is changed, the balance of water produced by the fuel cell and water removed by the effluent gases is disrupted. This subsequently causes a change in the membrane water content which affects whether or not the fuel cell eventually ignites or extinguishes. Changes in the water inventory will result in a change in the membrane resistance. As the fuel cell equilibrates to the new conditions, the cell current is seen to change as well. The results also indicate that the coupling of transport and reaction give rise to response times that

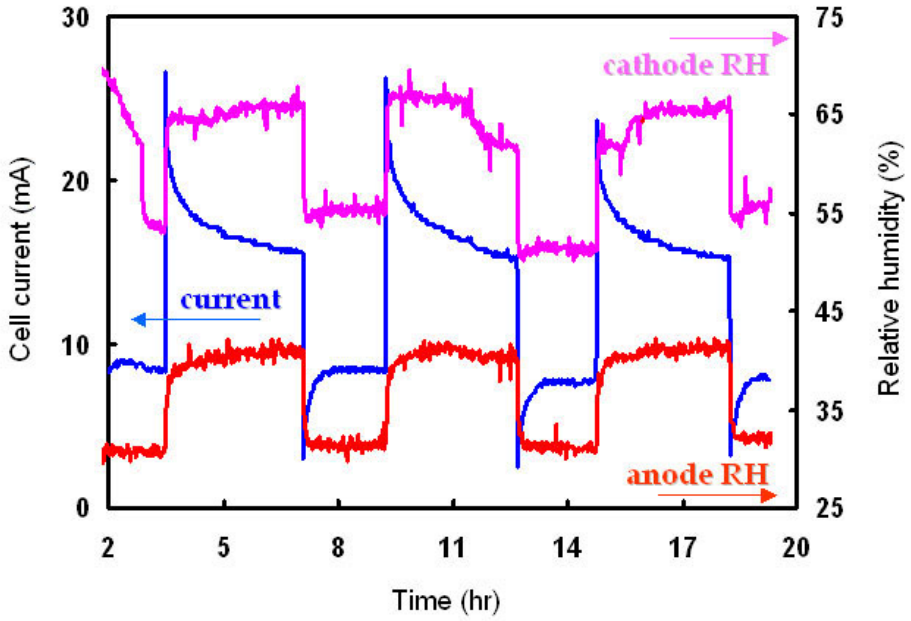

Figure 3.14: Autonomous oscillations observed in the STR-PEM fuel cell operating with 5 mL/min of hydrogen, 10 mL/min oxygen, 90°C, and 0 Ω external load resistance. Note that although the operating parameters remained fixed, regular oscillations in current and effluent relative humidities persisted for almost one day.

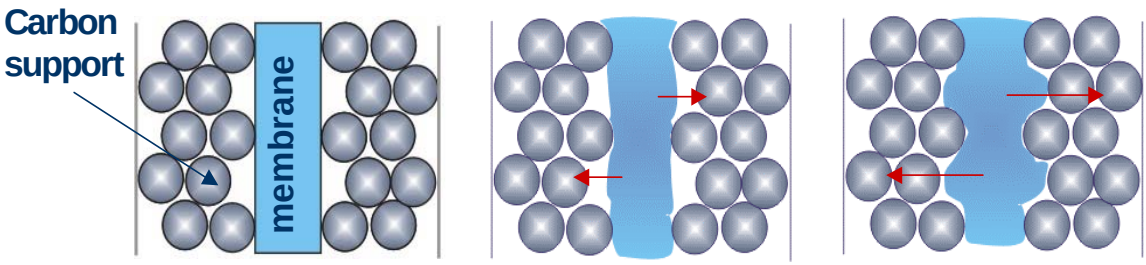

Figure 3.15: Membrane swelling and relaxation are the likely cause of the sustained oscillations. (a) The membrane is in contact with the catalyst support particles. (b) Applied pressure enhances the membrane/catalyst contact. (c) Additional pressure further increases the membrane/catalyst contact.

can be as long as hundreds of seconds. Finally, the interesting sustained oscillations are a testament to the complex and rich dynamics that remain to be explored in the STR-PEM fuel cell.

Chapter 4

Modeling Water Balance and Steady State Multiplicity in a STR-PEM fuel cell

In this chapter, we revisit steady state multiplicity in the exothermic CSTR and describe the analogy between heat autocatalyticity in an exothermic CSTR and the autocatalyticity observed in the STR-PEM fuel cell. We further develop a mathematical model of the STR-PEM fuel cell which captures the essential physics that control the ignition/extinction phenomena. We also explore the dynamic and parametric operation of an STR-PEM fuel cell with modeling tools for the dynamic/parametric analysis of chemical reactors (continuation, singularity theory, numerical stability and bifurcation analysis) to explore the STR-PEM dynamic and parametric operation (Balakotaiah and Luss, 1982a; Balakotaiah and Luss, 1982b; Doedel, 1981; Farr and Aris, 1986).

4.1 Steady State Multiplicity

Membrane water content plays a major role in both the dynamics and the steady state behavior of the cell. Excess water or too little water will hamper the fuel cell performance. Although an optimum level of water is desirable, as previously established, the membrane water content is a dynamic variable that changes with parameters.

The classic chemical engineering ignition/extinction phenomena are caused by the Arrhenius temperature-based rate acceleration due to the heat produced by an exothermic reaction. The heat produced as an exothermic reaction progresses increases the temperature and further accelerates the reaction. The analogy of a *positive feedback* holds true in both the exothermic CSTR and the STR-PEM fuel cell. In the fuel cell, as water is produced, the membrane conductivity increases, and the reaction accelerates. In the same way that the reaction rate depends on temperature exponentially, the membrane conductivity too depends on the water content exponentially, as depicted in Figure 4.1. It is interesting to see that conductivity data measured at several temperatures show that the membrane conductivity is only a weak function of the fuel cell temperature. Therefore an empirical fit of the membrane conductivity valid over the measured range of temperatures can be obtained (Yang, 2003).

Referring back to the classic CSTR, combined energy and mass balance equations yield expressions for the heat production and heat removal. When plotted as functions of temperature, intersections of the heat removal line and heat production curve represent the steady states. In the STR-PEM fuel cell, since we are concerned with the balance between water removal and water production, plots of *water removal* and *water production*

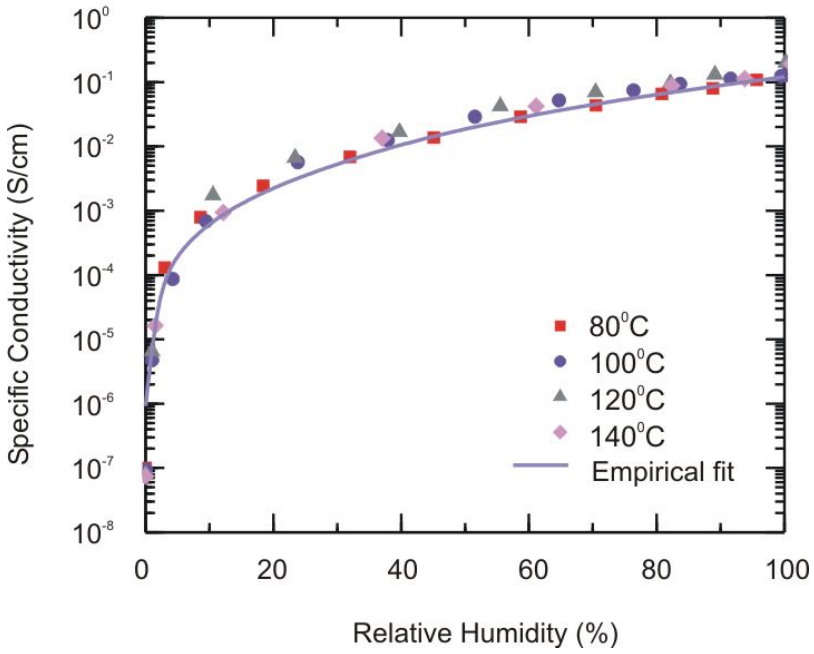

Figure 4.1: Conductivity of a Nafion 115 membrane. The conductivity depends strongly on the relative humidity but is only weakly dependent on temperature. This strong coupling is responsible for the autocatalytic nature of the fuel cell reaction. As the fuel cell reaction progresses, water that is produced further humidifies the membrane and the conductivity increases; easing proton transport across the membrane. A positive feedback loop on the transport drives the reaction even further (Yang, 2003).

as functions of the membrane water content will yield similar intersections (see Figure 4.2). The sigmoidal water production curve results from the strong dependence of conductivity on the water content.

Out of the three intersections, the middle steady state (marked 2) is unstable while the other two steady states (extinguished state 1 and ignited state 3) remain stable. From steady state 2, a fluctuation to the right would result in the water production rate exceeding the water removal rate. This would increase the overall water content in the fuel cell and drive the steady state towards 3. A fluctuation to the left of 2 also drives the system away from 2 but towards the extinguished state 1. This results from the larger water removal rate over the water production rate with the fluctuation to the left which dries out the fuel cell and extinguishes the current.

We have previously mentioned that the operating parameters also affect the fuel cell operation. In Figure 4.2, we illustrate how an increase in the load resistance and temperature can affect the steady states. We intuitively expect that a lower current would result from a larger load resistance. We see that this arises because the larger load essentially distorts the water production curve downward (while the water removal remains unchanged) and shifts the locations of the intersections. With an increase in R_L, the ignited state 3 appears at a lower membrane water content. For even larger R_L, steady state 3 disappears altogether. Altering the cell temperature changes the slope of the water removal line which also results in different steady states.

In Chapter 3, we presented data of the fuel cell startup with several feed humidification levels (as determined by the humidifier temperatures). For higher humidifier temperatures, the larger vapor pressure results in greater humidification of the feed

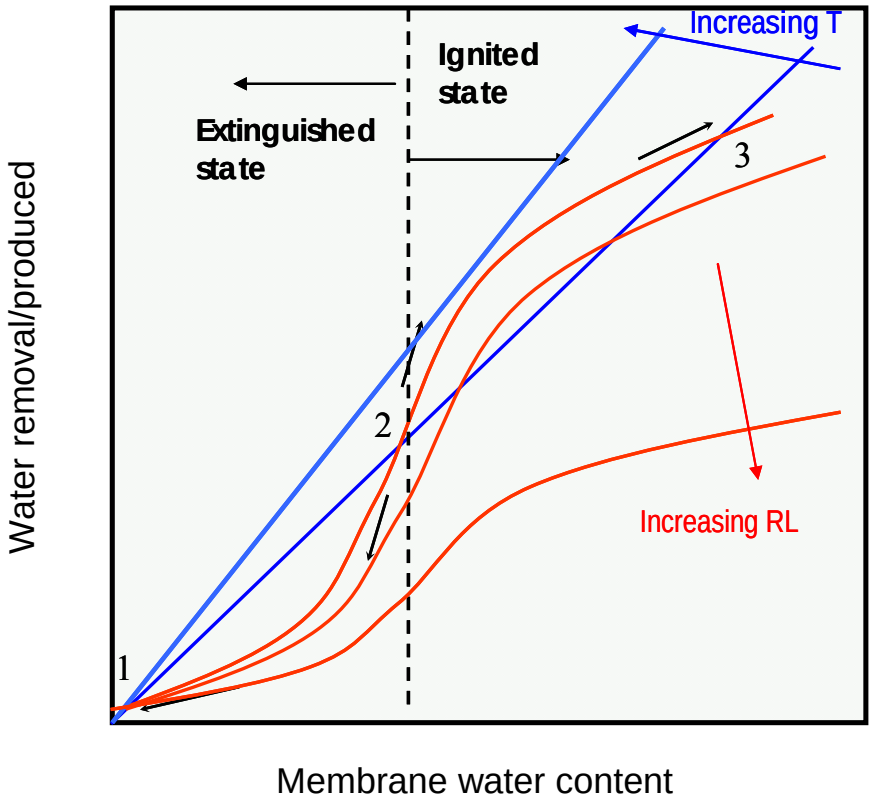

Figure 4.2: Steady state multiplicity in the STR-PEM fuel cell is analogous to the classic steady state multiplicity in the exothermic CSTR. In the STR-PEM fuel cell, the steady state multiplicity is characterized by a balance between water produced (sigmoidal curves) and water removed (straight lines) from the cell. Changing the controllable parameters will affect the intersections of the water production and water removal curves, thereby shifting the steady states. The stable steady states are marked as 1 (extinguished) and 3 (ignited) with the unstable steady state 2 in the middle.

streams. Recall that for sufficiently humidified hydrogen feed streams, the fuel cell current ignited. Changing the feed humidification in the STR-PEM fuel cell is analogous to changing the feed temperature in the exothermic CSTR. For the CSTR, the heat removal line shifts to the left or right with different feed temperatures. In a similar way, the different feed humidification shifts the water removal line as depicted in Figure 4.3. An increase in humidification shifts the water removal line to the right, resulting in only one intersection at the high membrane water content which corresponds to the ignited current state.

4.2 The Simplified Stirred Tank Reactor PEM Model

A schematic of the hydrogen-oxygen STR-PEM fuel cell is shown in Figure 4.4 (a) with hydrogen and oxygen gases fed into the anode and cathode chambers at inlet molar rates of $n_{H_2}^{in}$ and $n_{O_2}^{in}$ (mol/s) respectively. Hydrogen molecules are dissociatively adsorbed at the anode and oxidized to protons. Protons diffuse through the PEM under an electrochemical gradient to the cathode while electrons travel across an external load resistance R_L, (Ω). Oxygen molecules adsorbed at the cathode are reduced by the electrons and react with the protons to produce water.

Our version of the STR-PEM fuel cell model is an autohumidified one where no water vapor is contained in the feed gases and the membrane is humidified by the water produced. The anode and cathode chambers are modeled as two stirred tank reactors sandwiching the PEM. Figure 4.4 (b) is a simplified electrical circuit representation of

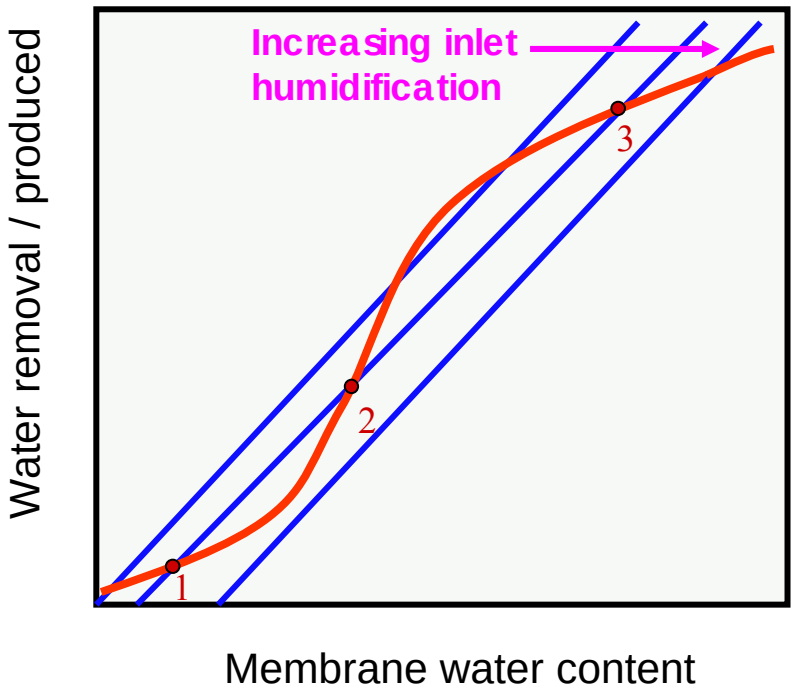

Figure 4.3: Humidification effect on the water balance in an STR-PEM fuel cell. The inlet humidification is analogous to the feed temperature in the exothermic CSTR. Humidifying the feed streams will shift the water removal line towards the right, resulting in a change in the water production and water removal intersections.

the fuel cell model where R_M (Ω) denotes the membrane resistance to proton transport and V (Volts) is the voltage associated with the chemical potential difference across the membrane. The operating parameters are the fuel cell temperature T (K), external load resistance R_L, and inlet molar rates $n_{H_2}^{in}$ and $n_{O_2}^{in}$. The rate of water production in the fuel cell is expressed through the cell current i (Amps).

The polymer electrolyte membrane serves as the medium for proton transport. A Nafion™ membrane, which is a partially substituted perfluoro-sulfonic acid ionomer is used. Water absorbed into the membrane ionizes the sulfonic acid groups, and facilitates proton transport via a hopping mechanism between fixed ions. Membrane humidification is essential since proton conductivity increases exponentially with membrane water content (Eikerling et al., 1997; Hsu and Gierke, 1982; Paddison, 2001; Thampan et al., 2000).

Our model is centered on the water balance in the cell, expressed in terms of a single *dynamic variable*: the dimensionless water activity in the membrane, a_w. At this level of modeling, this activity is assumed uniform over the membrane. This activity is defined as the gas partial pressure of water P_w, at equilibrium with the membrane divided by the vapor pressure of water at the cell temperature $P_w^o(T)$. This single dynamic variable determines the cell dynamics through the water content in the membrane $\lambda(a_w)$, and the membrane resistance to proton transport $R_M(a_w)$.

The membrane water content λ expressed in terms of water molecules per membrane sulfonic acid group, has been correlated experimentally by Yang (Yang et al., 2004) to a multilayer BET model (Thampan et al., 2000). Here λ_m represents the monolayer

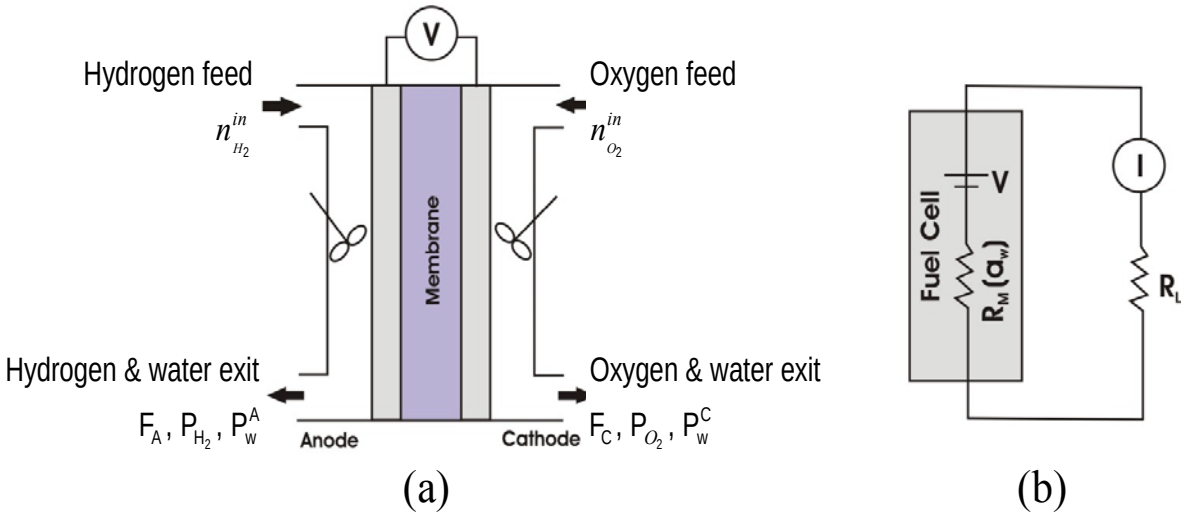

Figure 4.4: PEM fuel cell model. (a) The anode and cathode chambers in the PEM fuel cell are modeled as two stirred tank reactors in series. Non-humidified hydrogen and oxygen are fed into the reactor while the unreacted gases and product water exit from each chamber. (b) An electrical circuit equivalent of the PEM fuel cell model.

coverage of water on the sulfonic acid groups, n_L is the number of layers that can be adsorbed, and c depends on the chemical potential change due to water adsorption.

$$\lambda = \lambda_m \frac{[ca_w][1-(n_L+1)(a_w^{n_L}+n_L a_w^{n_L+1}]}{(1-a_w)[1+(c-1)a_w - ca_w^{n_L+1}]}; \quad \frac{[H_2O]}{[SO_3^-]} \qquad (4.1)$$
$$\lambda_m = 2;\ n_L = 9.2;\ c = 35$$

We use a simple polynomial fit to Yang's data to obtain the following expression for the water uptake λ:

$$\lambda = 14.9a_w - 44.7a_w^2 + 70.0a_w^3 - 26.5a_w^4 - 0.446a_w^5 \qquad (4.2)$$

Based on conductivity data, the membrane resistance to proton transport has been experimentally determined to have negligible temperature dependence. Therefore, the resistivity changes by less than a factor of 2 between 80-140°C, compared to a factor of 10^6 as the water activity varies between 0 and 1 (Yang et al., 2004). For a membrane of thickness l cm and area A cm^2, the membrane resistance decreases exponentially with the membrane water content and has been correlated as follows for an unconfined membrane (a membrane that is outside of the fuel cell; we address the confined membrane later in this chapter).

$$R_M(a_w) = 10^7 \exp(-14a_w^{0.2})\frac{l}{A} \quad [\Omega] \qquad (4.3)$$

From the electrical circuit representation of the fuel cell in Figure 4.4 (b), we can express the cell current (reaction rate) as

$$i = \frac{V}{R_M(a_w) + R_L} \qquad [\text{A}] \qquad (4.4)$$

The current depends on the sum of both the external load resistance and the membrane resistance. We see that the membrane water activity a_w affects the cell current through

the membrane resistance. The cell potential V is almost independent of reactant concentration as long as the reactant utilization is less than ~80%.

We neglect, for the moment, kinetic limitations for the transport of water between the membrane and the gas phase in the anode and cathode chambers, and assume that the water vapor pressure P_w is at equilibrium with the membrane water activity. The partial pressure of water in the two chambers is the product of the water vapor pressure at the cell temperature and the membrane water activity $P_w = P_w^o(T)\, a_w$. Experimental observations of comparable water outflows from both the anode and cathode chambers support this initial simplification. The cell mass balance for water is shown below in Equation 4.5, where $\mathcal{F}$ is Faraday's constant (96,500 C/mol), while V_A^g and V_C^g (L) represent the volume of gas in the anode and cathode chamber respectively. The accumulation of water in the membrane depends on the water uptake by the membrane itself and water in the gas phase. Water removal from the fuel cell depends on the exiting flow rates from each chamber.

$$\left[N_{SO_3} \frac{d\lambda(a_w)}{da_w} + (V_A^g + V_C^g)\frac{P_w^o}{RT} \right] \frac{da_w}{dt} = 0.5\frac{i(a_w)}{\mathcal{F}} - (F_A + F_C)P_w^o \frac{a_w}{RT} \quad (4.5)$$

water in the membrane *water in the gas phase* *water production* *water removal*

Mass transfer coefficients will be required at a subsequent level of modeling to quantify mass transfer rates between the membrane and the gas phase; water transport across the membrane will also result in differences in the water activity at the anode and cathode. We assume constant pressure operation (P_{tot} =1 bar, same in both chambers). In a further simplification, one may consider that the reactants enter the cell at dilute concentrations, so that the molar flow rate can be considered constant. We will also consider

the case where the reactant feeds are pure components. In this case, the exit flow rates F_A and F_C in the above equation are determined by the inlet molar flow rates, $n_{H_2}^{in}$ for the anode and $n_{O_2}^{in}$ for the cathode, the operating pressure P_{tot} and the reaction rate. Given our gas-membrane equilibrium assumption for water, which equipartitions the water produced between the two chambers, F_C is independent of the water activity, while, for the anode, F_A will now depend on a_w.

$$F_C = \frac{n_{O_2}^{in} RT}{P_{tot}} \qquad \text{[L/s]} \tag{4.6}$$

$$F_A = \frac{RT}{P_{tot}}\left[n_{H_2}^{in} - 0.25\frac{i(a_w)}{\mathcal{F}} \right] \qquad \text{[L/s]} \tag{4.7}$$

The water balance expressed in Equation 4.5, either with the flow rates F_A and F_C constant, or alternatively given by the expressions above is our initial working model. For pure feed operation, the gas phase pressure variation of hydrogen in the anode and oxygen in the cathode directly follow:

$$\frac{dP_{H_2}}{dt} = \frac{RT}{V_g^A}\left[n_{H_2}^{in} - F_A\frac{P_{H_2}}{RT} - 0.5\frac{i(a_w)}{\mathcal{F}} \right] \tag{4.8}$$

$$\frac{dP_{O_2}}{dt} = \frac{RT}{V_g^C}\left[n_{O_2}^{in} - F_C\frac{P_{O_2}}{RT} - 0.25\frac{i(a_w)}{\mathcal{F}} \right] \tag{4.9}$$

In the previous chapter, we presented experimental evidence that the initial membrane water content can either ignite or extinguish the fuel cell current. Here, we show that our model is capable of capturing the startup dynamics from different initial membrane water contents. In Figure 4.5, for low water contents (as indicated by λ), the fuel cell current extinguishes. Beyond a critical value of λ, the current increases up to the ig-

nited state. The time it takes to reach the high current steady state is shorter when the fuel cell starts up from an even higher λ.

To illustrate the water balance we graphically show, in Figure 4.6 (a) the water production and water removal curves (the first and second terms on the right-hand-side of Equation 4.5 respectively). For simplicity, we first consider the dilute reactant feed case where the molar flow rates of F_A and F_C are constant. The water removal curve is a straight line in this plot, while the experimentally correlated water production curve is sigmoidal, due to the exponential enhancement of proton transport with membrane water activity. Steady states correspond to the intersection of the two curves where stable (unstable) ones are marked with filled (empty) circles.

Slight perturbations around the middle (unstable) steady state will, in a fashion analogous to the autothermal reactor stability arguments discussed previously, drive the STR-PEM fuel cell towards the upper or lower stable steady states. For a pure feed under constant pressure operation, the anode and cathode outlet gas flow rates F_A and F_C are not constant and this causes changes in the curvature of the water removal curve. The slight curvature in the water removal line can be seen in Figure 4.6 (b) and (c). However, the qualitative sense of the results and their dependence on operating parameters provided by the diagram still holds.

The membrane resistance in Equation 4.3 is based on conductivity measurements of the membrane outside the fuel cell. When the membrane is sandwiched between the two electrodes and graphite flow channels, it is conceivable that the membrane is subjected to a mechanical stress. Figure 4.6 (c) shows water production predicted by a modified membrane resistance expression for the membrane in the confined state:

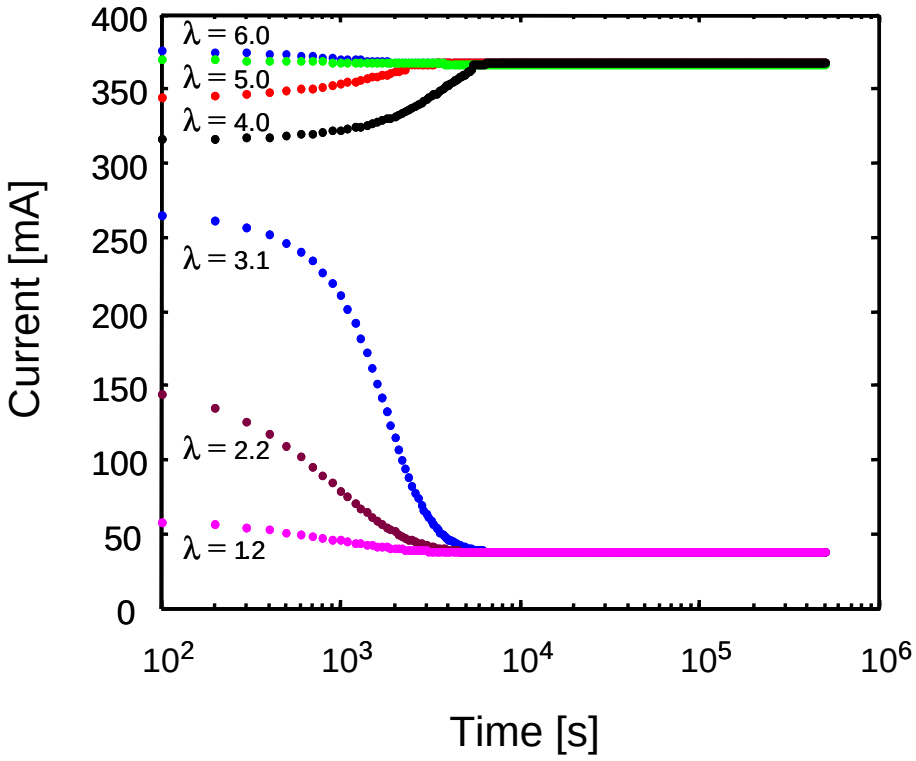

Figure 4.5: Predicting fuel cell startup with the simplified STR-PEM model. The STR-PEM model successfully captures the experimentally observed fuel cell startup behavior. For different initial membrane water contents as indicated by λ, the fuel cell current will ignite or extinguish.

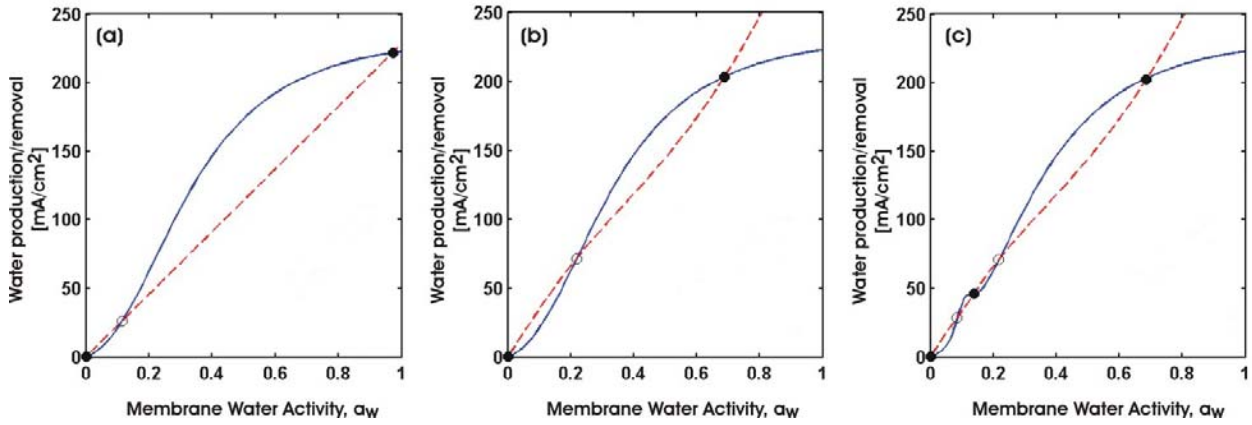

Figure 4.6: Water management and steady state multiplicity in a PEM fuel cell. Water production (solid curve) and removal (dashed curve) are illustrated as functions of the membrane water activity, a_w. The filled (empty) circles denote stable (unstable) steady states. (a) Dilute reactant feed with $T = 298$ K, $R_L = 1.2$ Ω, $F_A = F_C = 1.42\text{x}10^{-6}$ m^3/s; (b) Pure reactant feed with $T = 353$ K, $R_L = 1.2$ Ω, $P_T = 10^5$Pa, $n_{H2}^{in} = n_{O2}^{in} = 5.7 \text{ x } 10^{-6}$ mol/s (c) Pure reactant feed with a modified membrane resistance expression that gives rise to the occurrence of five steady states; three of which are stable. $T = 353$ K, $R_L = 1.2$ Ω, $P_T = 10^5$Pa, $n_{H2}^{in} = n_{O2}^{in} = 5.7 \text{ x } 10^{-6}$ mol/s.

$$R_M(a_w) = \left\{ 10^7 \exp(-14 a_w^{0.2}) - \left[y_o + \frac{\mu}{w\sqrt{\pi/2}} \exp\left[-2\left(\frac{a_w - x_c}{w} \right)^2 \right] \right] \right\} \frac{l}{A} \qquad (10)$$

This expression (with μ = 76, y_o = 0.01, w = 0.07, x_c = 0.08) attempts to capture the experimental observation of "pinning" of the membrane resistance over certain intermediate ranges of water activity. We believe that this pinning, which causes the membrane resistance to vary in a stepwise fashion as depicted in Figure 4.7, arises from the mechanical constraints the electrode assembly imposes on the swelling membrane. As Figure 4.6 (c) shows, this can lead to five total (three stable) steady states, consistent with experimental observations (Moxley et al., 2003).

The water balance diagrams in Figure 4.6 can be used to explore the dependence of cell ignition on operating parameters. Temperature mainly affects water removal through the water vapor pressure since higher temperatures are expected to increase the slope of the water removal curve. The load resistance, on the other hand alters water production such that increasing R_L depresses the water production curve, especially at high water activities. Higher reactant flow rates tilt the water removal curve higher. It is interesting to observe that prehumidification of the reactant feeds translates the water removal line/curve to the right. These considerations elucidate the way steady state multiplicity depends on parameters. Before a more systematic presentation of these results, a caveat: the validity of both the data and the model predictions is limited to water activities less than (possibly approaching) one. Predictions of our simplified model beyond this limit are invalid; they signal conditions under which condensation of liquid water will occur (something experimentally observed). An extension to a two-phase model will be required to quantify such operation.

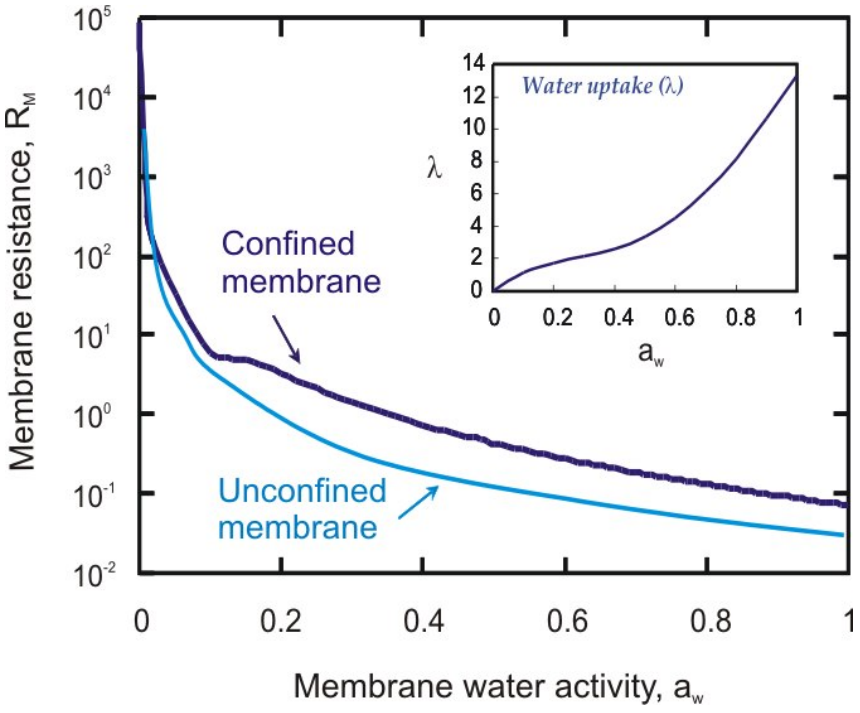

4. Figure 4.7: The membrane resistance based on conductivity measurements on an unconfined Nafion 115 membrane exponentially decreases with the membrane water activity. A membrane sandwiched in between the electrodes and graphite plates is subjected to an additional mechanical stress which gives rise to the plateau observed in the membrane resistance. The five steady states observed in an STR-PEM fuel cell are attributed to this membrane pinning phenomena.

A Computational Parametric Study

We use continuation/numerical bifurcation techniques implemented in the software AUTO to identify regions in parameter space where steady state multiplicity exists (Doedel, 1981). The four experimentally controllable parameters, T, R_L, $n_{H_2}^{in}$, and $n_{O_2}^{in}$ are varied in our computations. Since we assume that water in the membrane and water in the vapor phase are in equilibrium, constant pressure operation at 1 bar indirectly establishes a maximum temperature of 373 K that is allowable in the fuel cell.

The continuation results are organized in terms of three two-parameter bifurcation diagrams: T and R_L in Figure 4.8; T and $n_{H_2}^{in}$ in Figure 4.9 (a); $n_{O_2}^{in}$ and $n_{H_2}^{in}$ in Figure 4.9 (b). Regions of one, three, and five steady states are marked I, III and V respectively. Blowups of the first two diagrams are included as insets, to provide a better feeling of steady state multiplicity over larger parameter ranges. Representative one-parameter cuts, marked on the two-parameter diagrams by α and β, are included to illustrate the various ignition-extinction transitions involved. The ordinate of the one-parameter diagrams show the steady state cell current density which reflects water production in the fuel cell. Ignited branches are characterized by high current densities whereas extinguished branches are represented by lower current densities. Solid curves in the one-parameter bifurcation diagrams denote stable steady states while dashed curves correspond to unstable ones.

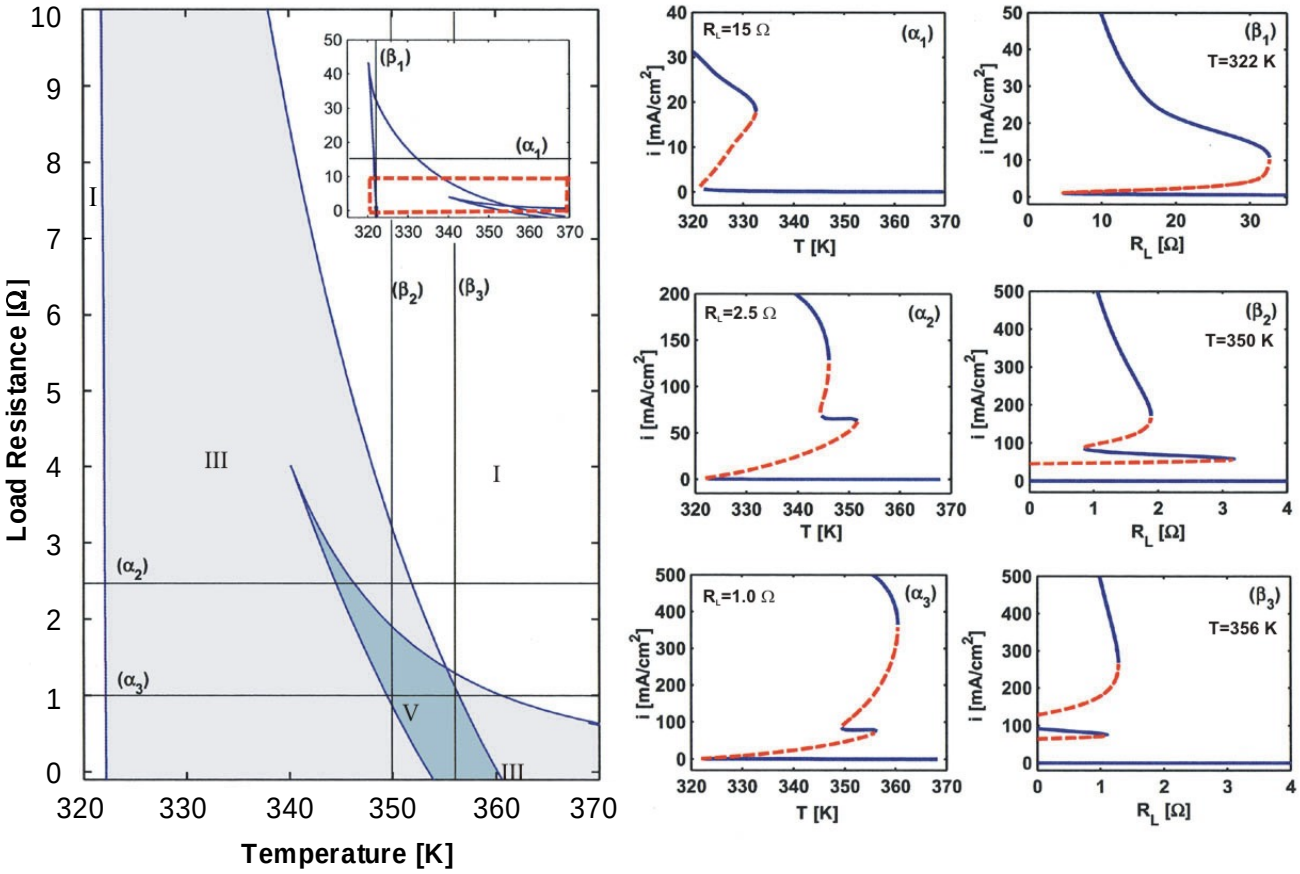

Figure 4.8: Two-parameter bifurcation diagram in T and R_L for $n_{H2}^{in} = n_{O2}^{in} = 5.7 \times 10^{-6}$ mol/s. Regions of one, three, and five steady states are marked by I, III, and V. Corresponding one-parameter continuation diagrams with respect to temperature and load resistance are shown in (α_1)-(α_3) and (β_1)-(β_3) respectively. The solid (dashed) curves denote stable (unstable) steady states.

Figure 4.8 depicts a two-parameter bifurcation diagram in the load resistance - temperature plane with inlet gas rates of 5.7 x 10^{-6} mol/s (10 mL/min). Figure 4.8 (α_1)-(α_3) constitute representative one-parameter diagrams with respect to temperature at load resistance values of 15 Ω, 2.5 Ω, and 1.0 Ω respectively. For all these resistances, going below a temperature of about 325 K will cause an ignition. At these low temperatures the vapor pressure of water is so low that water is not convected away by the gas and builds up in the membrane, resulting in ignition. Although five steady states (of which three are stable) are observed for the 2.5 Ω and 1.0 Ω load resistances, only a maximum of three steady states (with two stable) is attainable for the large load resistance of 15 Ω (α_1). In addition, the cell current density at the ignited state is significantly lower compared to current densities obtained for smaller load resistances.

Similar one-parameter continuation diagrams in the load resistance at different temperatures are shown in Figure 4.8 (β_1)-(β_3) for temperatures of 322 K, 350 K, and 356 K respectively. From the cut at β_1, which intersects regions with one and three steady states, we see that the multiplicity region at 322 K spans the largest range of load resistances even though the current is lower. These one parameter cuts in temperature also indicate that for all temperatures, the fuel cell current extinguishes above a critical load resistance.

A two-parameter continuation of turning points in the hydrogen feed and temperature plane is shown in Figure 4.9 (a). Note that the dotted curve in Figure 4.9 has been shifted a little to the right to increase visibility of the two smaller three steady state

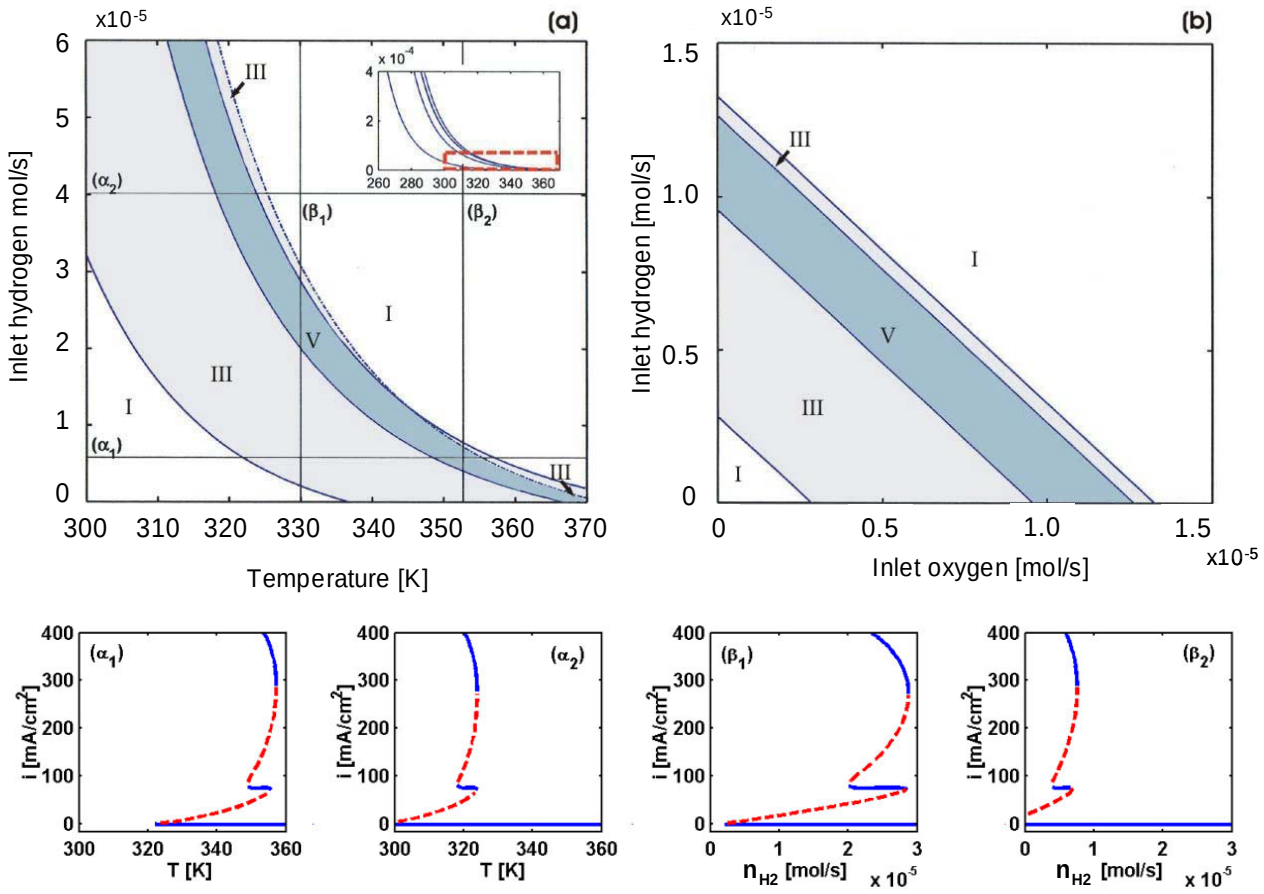

Figure 4.9: Two-parameter bifurcation diagram
(a) T and n_{H2}^{in} for R_L=1.2 Ω , n_{O2}^{in} = 5.7 x 10^{-6} mol/s (b) n_{O2}^{in} and n_{H2}^{in} for T=353 K, R_L=1.2 Ω. Corresponding one-parameter continuation with respect to temperature and to hydrogen feed are shown in (α_1)-(α_2) and (β_1)-(β_2) respectively.

regions. Representative one-parameter continuation diagrams with respect to temperature are shown at constant hydrogen feed rates of 5.7 x 10^{-6} mol/s (α_1) and 4.0 x 10^{-5} mol/s (α_2). Corresponding one-parameter diagrams with respect to hydrogen feed are depicted for fixed temperatures of 330 K (β_1) and 353 K (β_2).

Increasing the hydrogen feed convects the water product out faster, resulting in a drier membrane. Therefore, a comparison of the one parameter cuts in α_1 and α_2 indicate that the multiplicity region shifts towards lower temperatures when the hydrogen feed flow rate is increased. Since the vapor pressure of water increases with higher temperatures, from the one parameter cuts at β_1 and β_2, the final extinction is observed at lower hydrogen flow rates. In the one-parameter continuation with respect to temperature shown in Figure 4.9 (α_1)-(α_2), the most noticeable feature is the proximity of the two ignition points apparent in each. Cusp points and double-limit points (suggestive of a swallowtail organizing center) appear in our study (Guckenheimer and Holmes, 1983). No codimension two bifurcations were visible in the two-parameter diagram in the inlet hydrogen and inlet oxygen feed rate planes in the region covered in Figure 4.9 (b).

4.4 Summary

We have demonstrated, through a simplified but physically reasonable model of an STR-PEM, the occurrence of steady state multiplicity in PEM fuel cells. The steady state multiplicity is caused by the autocatalytic nature of the interplay between water that is produced in the fuel cell and the reaction rate itself, which is enhanced through membrane humidification. This creates a succinct analogy with the energy balance of an

autocatalytic CSTR: water activity in the STR-PEM corresponds to temperature in the CSTR.

Water production and removal are analogous to heat production and removal, and the corresponding straight removal line and sigmoidal production curve remarkably persist in the analogy. Inlet feed humidification in the STR-PEM is analogous to inlet feed temperature for a CSTR while the load resistance in the STR-PEM is analogous to reaction enthalpy in a CSTR. Another similarity is that the feed flow rates convect away the reaction product in both cases. Membrane swelling against mechanical constraints adds a five steady state "twist" to the STR-PEM dynamics, reminiscent of the richness of dynamics of exothermic reactions in series in a CSTR.

We have shown preliminary experimental results of sustained periodic and even chaotic oscillations in the differential STR-PEM fuel cell. In an integral PEM fuel cell reactor there is evidence of high-current, high local water content "wet spots," clearly analogous to tubular reactor "hot spots." The CSTR model presented here can be extended and effectively employed as "tanks in series" models of complex fuel cell geometries. Effective control for fuel cell vehicles will not be possible until the physical mechanisms and time scales of these complicated dynamics are understood.

Chapter 5

The STR-PEM Fuel Cell as a Reactor Building Block

In this chapter, we explore how the STR-PEM fuel cell (a differential reactor) can serve as a building block to approximate the more common integral type PEM fuel cells that contain more complicated flow channels. The approximation consists of connecting several of the STR-PEM fuel cells physically in series to each other. Here, we describe the rationale behind using the STR-PEM fuel cell as a reactor building block and present results that illustrate the existence of a water front within the fuel cell.

5.1 Tanks in Series

We have previously established that the STR-PEM fuel cell is a differential reactor which contains well mixed reactants and products throughout the anode and cathode chambers. Having a STR-PEM fuel cell simplified the experimental and modeling efforts since the spatial variations in concentration within the fuel cell was effectively removed. Recall that the only concentration gradient is transverse to the membrane in a STR-PEM fuel cell and it is effectively one dimensional. Because the STR-PEM fuel

cell is a differential reactor, we can connect several of these fuel cells physically in series to mimic the integral type PEM fuel cells (two dimensional PEM fuel cells) that contain spatial variations in current along the membrane. The concept of connecting STR-PEM fuel cells stems from the classic chemical engineering example of chemical reactors in series; CSTRs have routinely been linked in series to mimic plug flow reactors (PFRs) (Aris, 1965; Froment and Bischoff, 1979).

The STR-PEM fuel cells are connected such that the exiting flow streams from one tank become the inlet streams to the subsequent tank as depicted in Figure 5.1. The reactants can be fed into the tanks in a co-current flow scheme or they can be fed into the first and last tank such that the anode and cathode flows are counter-current to each other. Physically connecting the STR-PEM fuel cells in series enables us to monitor the changes in reactant and product concentration between the feed and exit streams which result in current variations along the membrane surface. Depending on the adopted flow pattern, flow rates, operating temperature, and external load resistance, in addition to the fuel cell orientation (vertical or horizontal), concentrations from tank to tank differ.

5.2 The Segmented Anode Parallel Channel Fuel Cell

Instead of physically connecting several individual STR-PEM fuel cells to model the integral reactor, we designed the tanks in series fuel cell as one unit as shown in Figure 5.2 (a). The membrane electrode assembly (MEA) is sandwiched between two Teflon blocks that contain graphite inserts. The Teflon blocks are placed between two aluminum blocks that were heated with stainless steel sheath cartridge heaters. A CN9000A Omega Engineering autotune temperature controller was used to monitor and control the

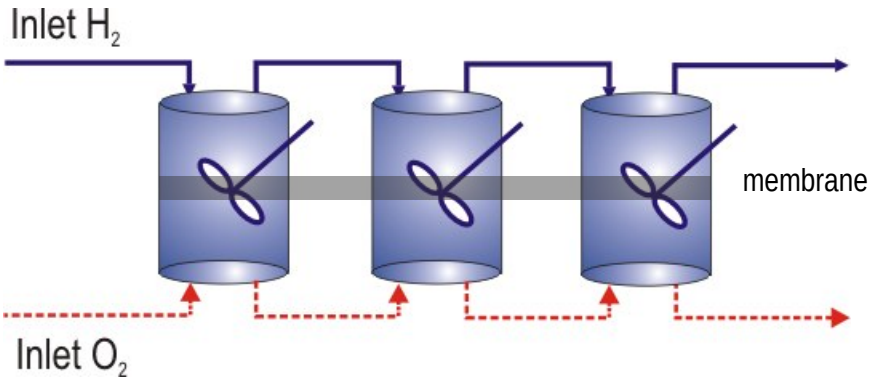

Figure 5.1: Schematic representation of several stirred tanks in series shown here with the inlet feeds to the same tank (co-current flow). Transport through the membrane is coupled from tank to tank.

fuel cell temperature. Reactant gases were fed from the same end into the anode and cathode flow channels (co-current) or fed from opposite ends of the fuel cell (counter-current). Exit flows from the fuel cell were fed into two graduated flow channels that contained water to prevent reactant backflow into the flow channels. Omega FMA A2400 mass flow controllers for hydrogen and oxygen were used to control reactant flow rates into the fuel cell between 1 and 10 mL/min.

The fuel cell was constructed with graphite flow channels that are 2 mm x 2 mm x 30 mm. Three of these flow channels were machined in parallel on the graphite which was inserted into a supporting Teflon block. The anode side, more appropriately referred to as the *segmented anode,* consisted of six individual graphite pieces separated by Teflon spacers as shown in Figure 5.2 (b). Each of these graphite segments effectively acted as an individual stirred tank reactor. The remaining reactant gases and product flows that exit from each segment become the inlet flow to the subsequent segment. The MEA consisted of two E-TEK electrodes that were hot pressed onto a Nafion 115 membrane. The membranes were coated with a platinum catalyst loading of 0.6 mg/cm^2 before hot pressing at 130°C and 1000 kg force for 90 seconds.

Copper sheets were placed on the back of the graphite pieces and lead wires were soldered onto these sheets. The wires extended from the copper sheet through the Teflon and aluminum blocks and were each connected to a 0.2 Ω sensing resistor. All six wires were then connected together with the common lead connected to a 10 turn 0 to 20 Ω potentiomenter (external load resistance). The circuit was connected to a CYDAS 1001DAP data acquisition board with 8 differential inputs to record the current measurements for each segment. We utilized separate graphite pieces for the anode because

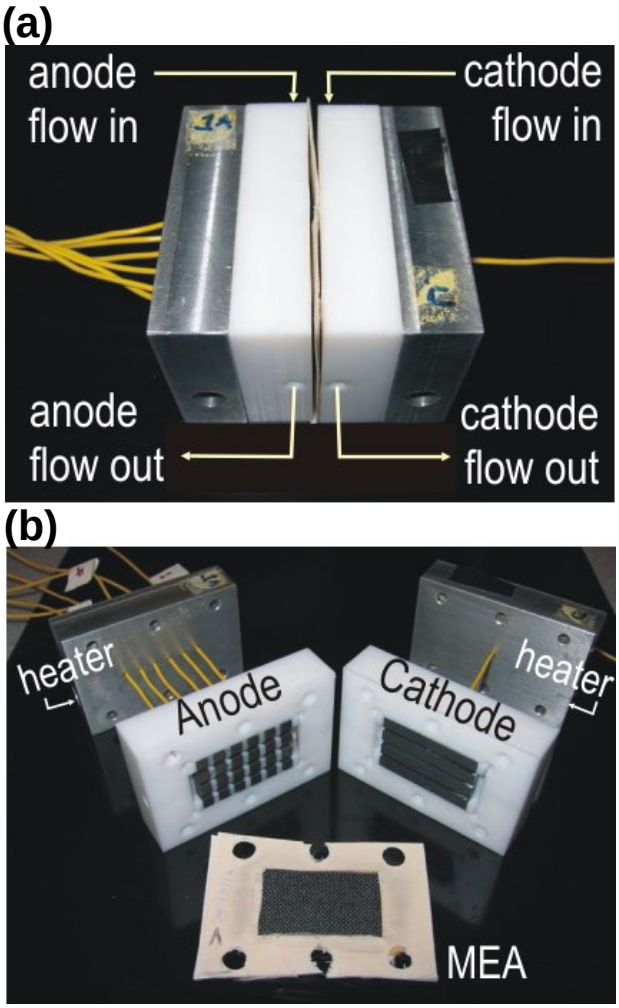

Figure 5.2: The segmented anode parallel channel fuel cell. The tanks in series version of the PEM fuel cell consists of six segmented graphite pieces in the anode that are separated by Teflon spacers and one complete graphite piece in the cathode that are sandwiching the MEA. The graphite pieces are inserted into two Teflon blocks that are pressed against heated aluminum blocks. Three flow channels are machined in parallel onto the graphite pieces. The wires extending from the back of the graphite are connected to a data acquisition board.

we needed to keep them electrically disconnected to obtain individual current measurements through each of the anode segments and voltage across the external load. The current measurements provided an indication of the amount of water produced in each segment and the current profile downstream from the anode inlet.

Although these segments are physically connected in series, they are electrically connected in parallel to each other as illustrated in Figure 5.3 (a) where R_M^i represents the membrane resistance associated with each tank. One can visualize the tanks (segments) in series as one large resistor with an equivalent resistance calculated according to resistances in parallel such that

$$R_M^{eq} = \frac{1}{\sum_{i=1}^{N} \frac{1}{R_M^i}} \tag{5.1}$$

The external load resistance R_L can be seen to be electrically in series with the equivalent resistance R_M^{eq} in Figure 5.3 (b). The current passing through the external load resistance is the sum of the currents from each tank.

The segmented anode fuel cell could be positioned with the gas flow channels in a horizontal or vertical orientation as illustrated in Figure 5.4 with reactant flows through the fuel cell in a co-current or counter-current scheme. When the flow channels were oriented vertically, both reactants were fed from the top in the co-current scheme but the feed into the anode was fed from the bottom in the counter-current flow scheme. Feed flow into the cathode remained from the top to bottom in both flow schemes to ease

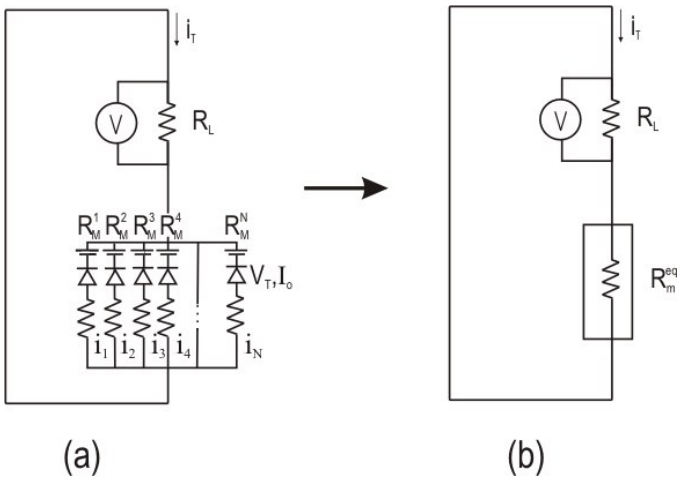

Figure 5.3: Equivalent electrical circuit for the segmented anode fuel cell. (a) Each segment is associated with an internal membrane resistance which is electrically connected in parallel to other segments (b) The equivalent resistance for these six segments is electrically in series with the external load resistance.

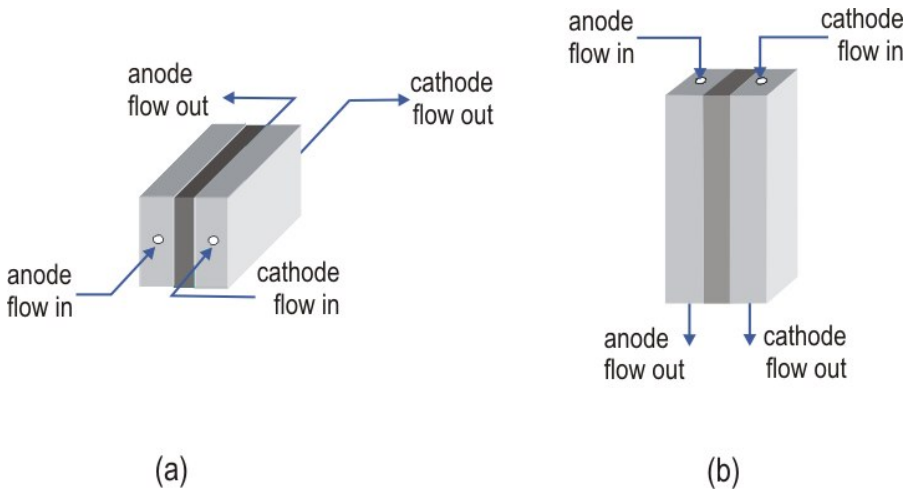

Figure 5.4: The segmented anode fuel cell configuration. The flow channels can be oriented (a) horizontally or (b) vertically. The fuel cell configuration is an important consideration when there is liquid water formation.

transport of liquid water out of the fuel cell. Under conditions where liquid water formation occurred, we found that the gas flow channel orientation was an important consideration. The segments are numbered from 1 thru 6 beginning with the segment closest to the anode inlet.

5.3 Current Evolution

We first monitored the current evolution in the segmented anode parallel channel fuel cell in a horizontal position (see Figure 5.5) and as expected, found measurable differences in currents downstream from the anode inlet. The MEA was equilibrated at room temperature conditions before it was assembled into the segmented anode fuel cell. Upon assembling the fuel cell, hydrogen and oxygen flows were started at 5 mL/min and fed co-current to the fuel cell with the external load resistance fixed at 3.5 Ω. For this initial run, the fuel cell was not heated. The membrane was sufficiently hydrated at the start so that we were able to measure a current as soon as we began operating the fuel cell.

Over the first several hours, the fuel cell equilibrated slowly to the new operating conditions and the currents in each segment were observed to reach a slight plateau. During this time, the current in the second segment was largest at 41 mA while the current in the last tank was the lowest at about 20 mA. This type of current distribution is expected for a fuel cell operating with co-current flows because more reactant reaches the front portion of the fuel cell (the part that is closer to the anode inlet). Since the initial membrane water content is uniform throughout the entire fuel cell, the initial current production is dependent on the amount of reactant reaching the electrodes within each segment.

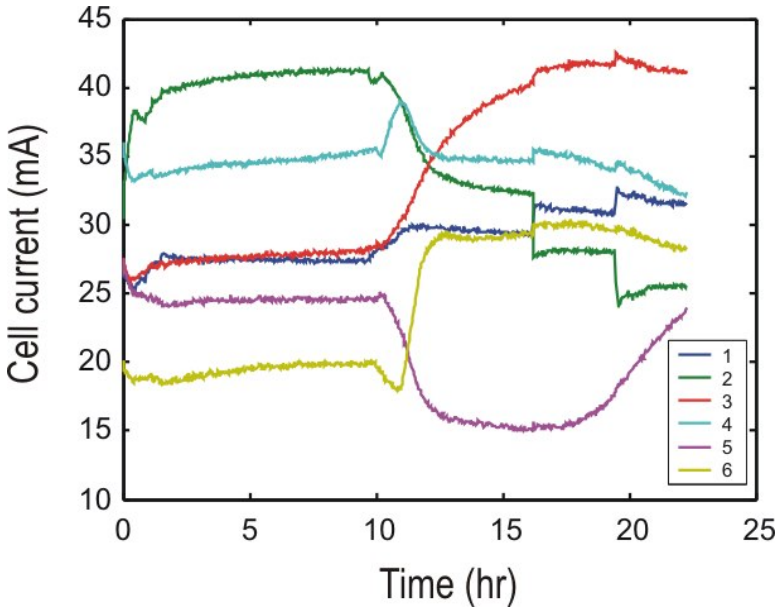

Figure 5.5: Current profiles in each segment over time for the fuel cell equilibrated at room temperature with reactant flow rates of 5 mL/min fed in co-current configuration and an external load resistance of 3.5 Ω. The gas flow channels were oriented horizontally.

Despite maintaining fixed operating conditions, the currents in each segment are observed to change somewhat dramatically after 10 hrs. We observed a rather sharp decline in the current in the second and fifth segments which was accompanied by an increase in current for the third and sixth segments. We believe that this change in current is attributable to a shift in the membrane water content downstream. With the larger initial current in the second segment, more water was produced in this segment resulting in a wetter portion of the membrane. Over time, the portion of the membrane in the second segment becomes saturated with water. Eventually, the water content in the neighboring portion of the membrane, the third segment, will also experience an increase in water content. This autocatalytically drives the reaction further and results in the increased current production there in the third segment. The decrease and increase in current observed for the fifth and sixth segments respectively are attributed to a similar effect of water transport in the portion of the membrane from the fifth to the sixth segment. The total current over the 24 hr period increased from 166 mA to 182 mA.

5.3.1 Ignition Fronts and Propagation

We studied ignition fronts for the fuel cell in both the horizontal and vertical flow channel configurations under both co- and counter-current reactant flows. The fuel cell was started up from an extinguished current state and the current profiles were monitored over time. The fuel cell was equilibrated with a hydrogen flow rate of 4 mL/min and an oxygen flow rate of 6 mL/min.

In the first study, the fuel cell current was previously extinguished at 75°C with reactants in counter-current flow. After extinguishing the current, the fuel cell temperature was lowered to room temperature while the load resistance was set to 20 Ω (to pre-

vent the cell from igniting during cooling). When the cell had reached room temperature, the external load resistance was set to a low load of 0.25 Ω to facilitate ignition. A color plot of the current profile downstream from the anode inlet as a function of time is presented in Figure 5.6 (a). From this plot, we observe that the fuel cell remained extinguished for some time and eventually started to ignite from the middle of the fuel cell. The sudden increase in current first occurred in the third segment and propagated outwards to the front (anode inlet) and back (anode exit). The darker red regions in the plot represent regions of high current and are *wet spots* in our fuel cell that are reminiscent of *hot spots* in the classic textbook examples of plug flow reactors (Aris, 1965; Froment and Bischoff, 1979). These wet spots are observed to move across the fuel cell over time. After the current in segment three reaches a maximum of 100 mA, the current production there begins to decline, while the current production increases downstream. The current profile across the fuel cell continues to evolve as the fuel cell strives to maintain a suitable balance between water production and water removal.

For the co-current operation under hydrogen and oxygen flow rates of 6 mL/min and 4 mL/min, ignition was recorded for the fuel cell equilibrated at a higher temperature of 60°C. Under the co-current flow scheme, the fuel cell was observed to ignite nearer to the anode exit in comparison to counter-current flow. As shown in Figure 5.6 (b) ignition was first observed in segment 5 and the current then propagated out towards the front and end of the fuel cell. Segment 4 ignited later than expected and the current in this segment was lower than the currents recorded for the neighboring segments 3 and 5.

Note that in Figure 5.6 (b), the red colored region appears divided by the low current in segment 4. The low current recorded for segment 4 is attributed to a reduced

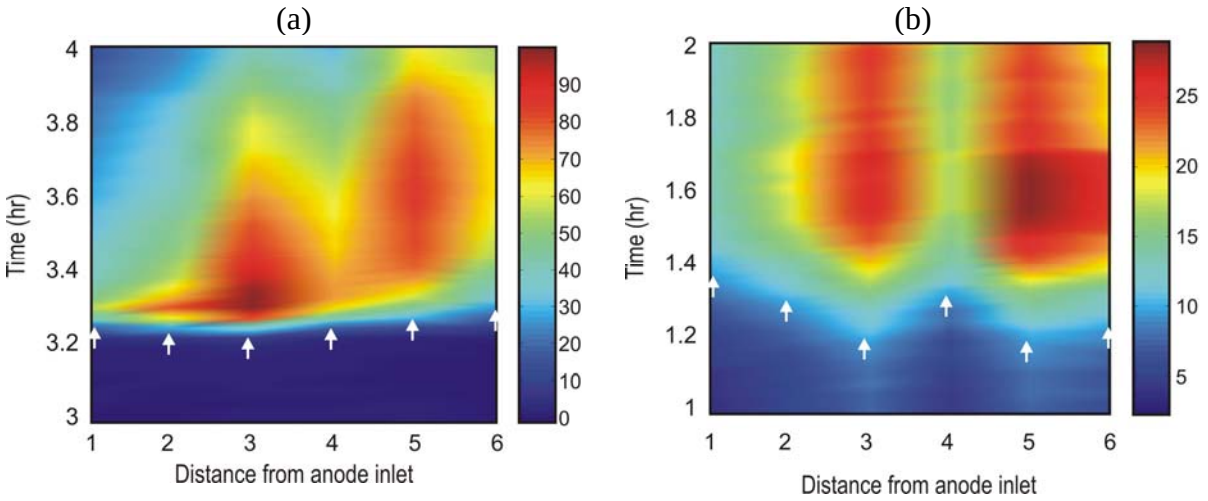

Figure 5.6: Ignition fronts for a horizontally oriented flow channel fuel cell with hydrogen and oxygen flow rates of 4 mL/min and 6 mL/min respectively. The colors represent the different intensities in cell current (mA). The cell current in each segment is plotted downstream from the anode inlet as a function of time: (a) Counter-current flows at 25°C. The current in segment 3 is the earliest to ignite and the front propagates to the edges; (b) Co-current flows at 60°C. Ignition first occurred in segment 5.

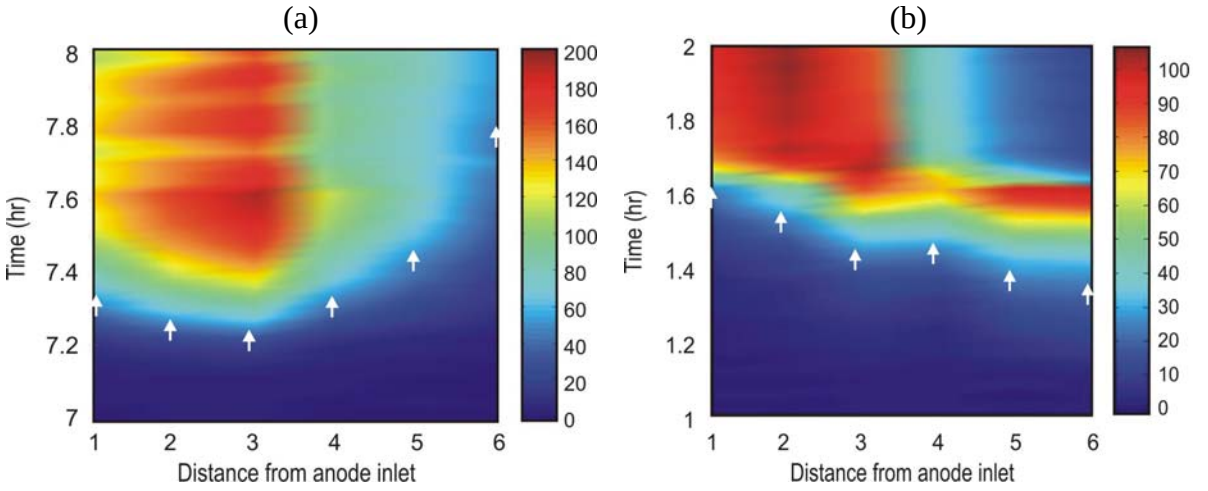

Figure 5.7: Ignition fronts for the vertically oriented flow channel with equal hydrogen and oxygen flow rates of 3.5 mL/min at 25°C: (a) Counter-current flow; (b) Co-current flow.

contact between the anode graphite insert and copper sheets. Note that the graphite and Teflon inserts are pushed into the Teflon backing, which sandwiches the MEA with the cathode piece. Wires were soldered onto the copper sheets so that the wire contacts the graphite insert. Both the anode and cathode blocks are fastened on each side with 6 nuts. If a portion of the fuel cell is slightly loose, the anode graphite insert at this loose portion will be slightly raised from the copper sheet, reducing contact with the wire.

In addition, operating the fuel cell with the gas flow channels configured horizontally was not optimal since liquid water could accumulate in the lowest flow channel, preventing the transport of reactants to available reaction sites there. As a result of the undesirable water build-up in the lower channels, we operated the fuel cell with the gas flow channels oriented vertically. In this configuration, any liquid water formed in the cathode compartment would drain downwards. In addition, the oxygen supply was fed into the cathode from the top to aid water removal by pushing the liquid down. We also recorded ignition effects in this configuration for both the counter-current and co-current flow scheme. The fuel cell was first extinguished with a high external load resistance of 20 Ω (to mimic open circuit conditions) at a high temperature of 75°C with hydrogen and oxygen flow rates of 10 mL/min into the fuel cell.

To observe ignition, the fuel cell was first cooled to room temperature. After the fuel cell was maintained at 25°C, the external load resistance was lowered back to 0.25 Ω with hydrogen and oxygen flows of 3.5 mL/min in counter-current. Ignition in the vertically oriented flow channels with counter-current gas flows occurred after an induction period of about several hours as shown in Figure 5.7 (a). Similar to the previous example of counter-current ignition in the horizontally oriented gas flow channels, we again ob-

serve that the fuel cell current first ignited in the third segment. The current then fanned out to the front end and the back end of the cell. However, in comparison to the horizontally oriented segmented anode fuel cell, the current generated in the vertical configuration was significantly larger. Focusing on the third segment alone, we see that a maximum current of 200 mA is produced in comparison to the 100 mA obtained from the horizontally oriented fuel cell.

By comparing the color plots in Figures 5.6 (a) and 5.7 (a) and considering the different range in current intensities (as indicated by the color bar to the right of each plot), the current generated in all the ignited segments of the vertically oriented fuel cell is larger than that produced in the horizontally oriented fuel cell. Since we operated the fuel cell at room temperature, it is conceivable that liquid water formed in the fuel cell. Figure 5.7 (a) indicates that the currents in the portion of the fuel cell closer to the anode inlet remained higher, suggesting that liquid water formed in the cell indeed accumulated near the bottom of the cell and hindered reactant mass transfer there (as suggested by the lower currents in the segments nearer to the anode exit). In addition, the larger current regions remained relatively fixed around the second and third segments.

Ignition fronts for the vertically configured flow channels with co-current reactant flows were also recorded. The fuel cell was extinguished with the same pre-treatment described for the counter-current fuel cell in the vertical configuration. We later cooled the fuel cell to 25°C, lowered the external load resistance to 0.25 Ω, and supplied hydrogen and oxygen gases at 3.5 mL/min to the anode and cathode in co-current. Both feeds were supplied from the top of the fuel cell. Unlike ignition fronts observed for the counter-current flow scheme, here we see that ignition first occurred in the segment far-

thest away from the anode inlet in segment 6 and propagated towards the inlet as shown in Figure 5.7 (b).

The wet spots that initially appear in the back portion of the fuel cell also propagate towards the front of the cell. The starkly different ignition fronts for the two different flow schemes are not surprising. In the co-current flow, it is easier for the portion of the membrane associated with segments that are farther away from the inlet streams to accumulate enough water for ignition since the flow is downwards from the top. Recall that the segments are numbered starting from the anode inlet. However, once the different segments have ignited, current production is higher for segments that are closer to the inlet streams. This increased current production near the inlet can be attributed to:

(i) liquid water accumulation in the gas channels of segments closer to the bottom of the fuel cell hinders mass transport of the reactants to the electrodes.

(ii) more reactant reaching and consumed in the front portion of the cell

When the fuel cell has equilibrated to the operating conditions after ignition, the co-current flow fuel cell produces a total current of 360 mA; much smaller than the total current produced in the counter-current flow fuel cell of about 620 mA in the same vertical configuration (see Figure 5.8). If one were to only measure the total current produced, ignition fronts in the segmented anode fuel cell would be overlooked as well as the differences in current downstream from the anode inlet.

5.3.2 Extinction Fronts

In addition to the ignition fronts, extinction fronts for the fuel cell were recorded for the horizontally oriented flow channel fuel cell with counter-current flows and the

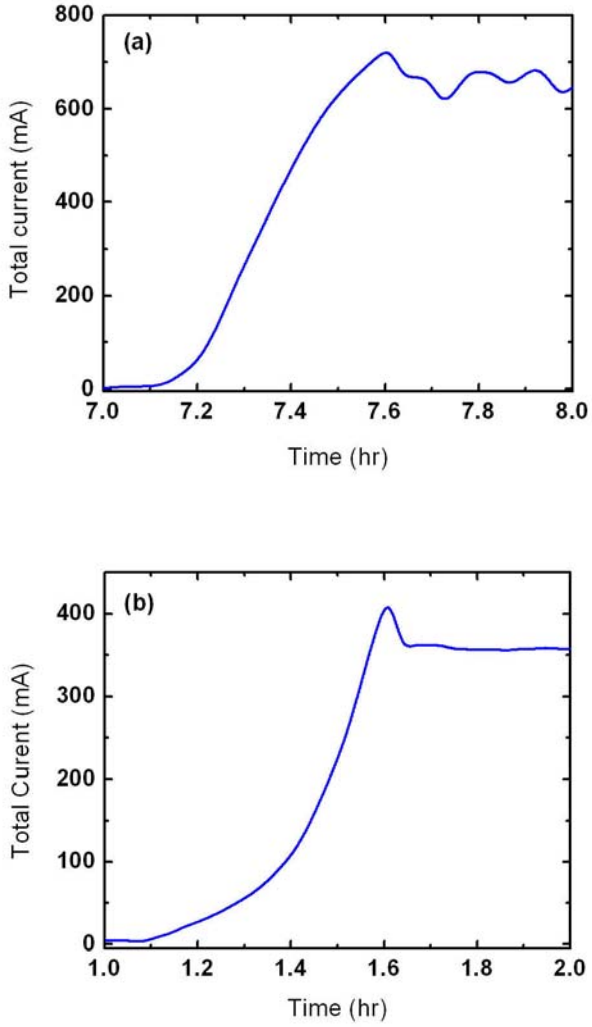

Figure 5.8: Total current profiles during ignition for the vertically oriented fuel cell with reactants fed in: (a) counter-current; (b) co-current. The total current generated for the counter-current flow fuel cell is higher than that generated in the co-current fuel cell under identical operating conditions.

the vertically oriented fuel cell with co-current flows. The extinction front in Figure 5.9 (a) was observed for the horizontally oriented fuel cell with counter-current flows of equal hydrogen and oxygen flow rates of 5.4 mL/min. The fuel cell was previously equilibrated at 60°C with an external load resistance of 10 Ω. Keeping the external load and flow rates fixed, the temperature was increased to 80°C to extinguish the current. By increasing the fuel cell temperature, we increased the water vapor pressure, resulting in more water flow out of the fuel cell. From Figure 5.9 (a), the current extinguished first in the segment closest to the anode inlet after 3 hours and the extinction propagated towards the back. Segments that produced less current at the start were the first to extinguish.

The extinction front shown in Figure 5.9 (b) was observed for the fuel cell configured vertically with co-current flows. The fuel cell was operated overnight at 70°C with reactant flow rates of 10 mL/min and an external load resistance of 2 Ω. The fuel cell currents were observed to be declining when the external load resistance was lowered to 0.25 Ω. The color plot in Figure 5.9 (b) depicts the fuel cell current extinction shortly after lowering the load resistance to 0.25 Ω. Despite lowering the external load resistance, the current production was not sufficiently large to prevent the fuel cell from extinguishing.

5.4 Extended Operation Results

5.4.1 Polarization Curves

Polarization curves for the segmented anode fuel cell were obtained by varying the load resistance from 0 Ω to 20 Ω over a period of about 100 seconds. Since the load

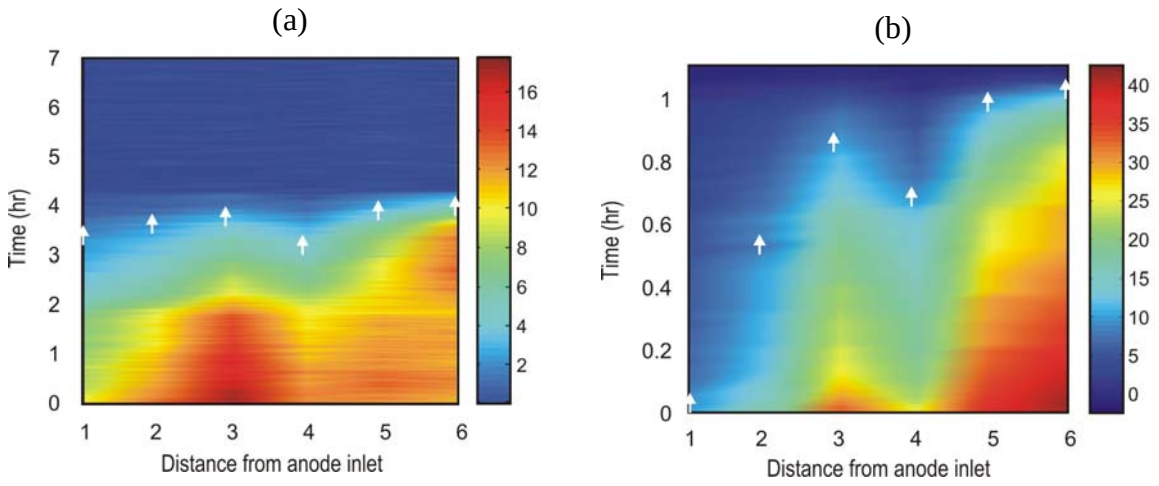

Figure 5.9: Extinction fronts: (a) Horizontally oriented flow channel fuel cell with counter-current reactant flow rates of 5.4 mL/min at 10 Ω and 80°C; (b) Vertically oriented fuel cell with co-current reactant flow rates of 10 mL/min at 0.1 Ω and 70°C.

resistance was changed over this relatively short time period, the obtained polarization curve is referred to as an *instantaneous* polarization curve where the membrane water content is expected to remain unchanged. Benziger et al. have shown that plotting the power produced by the fuel cell as a function of the load resistance is a more insightful representation of the polarization data (Benziger et al., in press). The power in the fuel cell can be expressed as

$$P = I^2 R_L = \left(\frac{V}{R_M^{eq} + R_L} \right)^2 R_L \, .$$

At the maximum power, we find that the load resistance associated with the peak power in the power performance curve is equal to the equivalent fuel cell membrane resistance. In this case, R_M^{eq} represents the equivalent membrane resistance for all six segments that are electrically connected in parallel.

$$\frac{dP}{dR_L} = \left(\frac{V}{R_M^{eq} + R_L} \right)^2 - \frac{2V^2 R_L}{\left(R_M^{eq} + R_L \right)^3}$$

$$\frac{dP}{dR_L} = 0 \rightarrow R_M^{eq} = R_L$$

A plot of the power performance as a function of the external load resistance is provided in Figure 5.10 (a) for the vertically configured segmented anode fuel cell previously equilibrated at 50°C and 4 Ω external load resistance with counter-current flows of hydrogen and oxygen at 10 mL/min and 5 mL/min respectively. From the plot, the equivalent membrane resistance is relatively small, at about 0.6 Ω. A more conventional polarization plot of voltage versus current is shown in Figure 5.10 (b). The different slopes

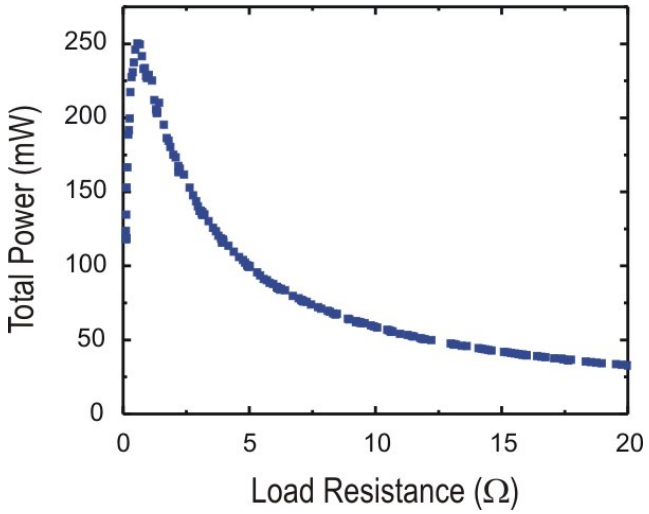

Figure 5.10: (a) Overall power performance curve for the fuel cell. The load resistance at peak power is equal to the equivalent membrane resistance for all six electrically parallel segments.

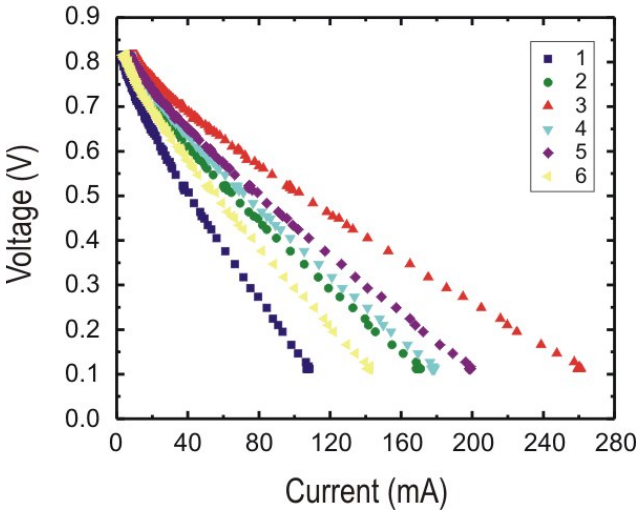

Figure 5.10: (b) Polarization curves for all six segments taken after equilibration at 50°C and 4 Ω with 10 mL/min of hydrogen and 5 mL/min of oxygen in counter-current flow. The different slopes indicate that each segment is associated with a different membrane resistance.

observed for each line indicates that the membrane resistance is slightly different within each segment.

5.4.2 Hydrogen Crossover Effect

In addition to observing ignition/extinction fronts in the segmented anode fuel cell, the fuel cell response to changes in other operating parameters such as the flow rates, temperature, and the external load resistance were monitored. Although it is a combination of the operating parameters that affect the membrane water content, we can generalize that it is optimal to operate under moderate flow rates and temperatures to prevent membrane dehydration. We were unable to sustain the fuel cell current when the reactant flow rates were too large because the increased reactant flow through the channels resulted in a greater rate of water removal, thereby drying the membrane more rapidly. We have also shown that increasing the fuel cell temperature can sometimes lead to the current extinguishing.

In one experiment, the segmented anode fuel cell was equilibrated to an increase in the load resistance after every hour and the current evolution in each segment was recorded as shown in Figure 5.11. Reactant flow rates of 5 mL/min to the anode and cathode were fed in counter-current flow. The fuel cell was oriented horizontally with the operating temperature set to 60°C. In general, the fuel cell current in each segment decreased with the higher load for the first five hours. However, negative currents were surprisingly measured in the last two segments of the fuel cell (segments 5 and 6). Following the start of these negative currents, subsequent increases in the load resistance did not result in any substantial change in the currents in each segment. When the load resis-

tance was changed to 20 Ω a little after 9 hours, the currents changed very slightly. Several autonomous steps in the current were observed at 11 hrs, 14.5 hr, and 21 hours.

Puzzled by these observed negative currents, we proceeded to decrease the load resistance in a similar stepwise fashion as shown in Figure 5.12. As we decreased the load, the negative currents in segments 5 and 6 became less negative. When the load resistance was lowered to 4 Ω, the current in segment 5 jumped up to 10 mA. The remaining negative current in segment 6 became positive when the load was further decreased to 0 Ω after 6 hours. At that same point in time, a slight decline in current was observed following the sharp increase in current for all segments. Several other autonomous changes in current were observed over time despite fixing all other operating parameters.

We observed negative currents for several other conditions and were rather perplexed by this phenomenon. However, we now believe that the negative currents arise due to hydrogen crossover from the anode to the cathode. Crossover is not a new occurrence and has been observed in direct methanol fuel cells with thin membranes (Heinzel and Barragan, 1999; Ren et al., 2000a; Ren et al., 2000b). Hydrogen crossover causes a decrease in the open circuit voltage for the PEM fuel cell. Hydrogen crossover in segments 5 and 6 of our segmented anode fuel cell brings excess hydrogen to the cathode which is unreacted with the oxygen at the cathode. The hydrogen is then oxidized and driven backwards across the membrane, resulting in the negative currents. Note that crossover is undesirable because it bypasses the electrical circuit, its normal reaction path, to produce water directly at the cathode and therefore does not produce usable power.

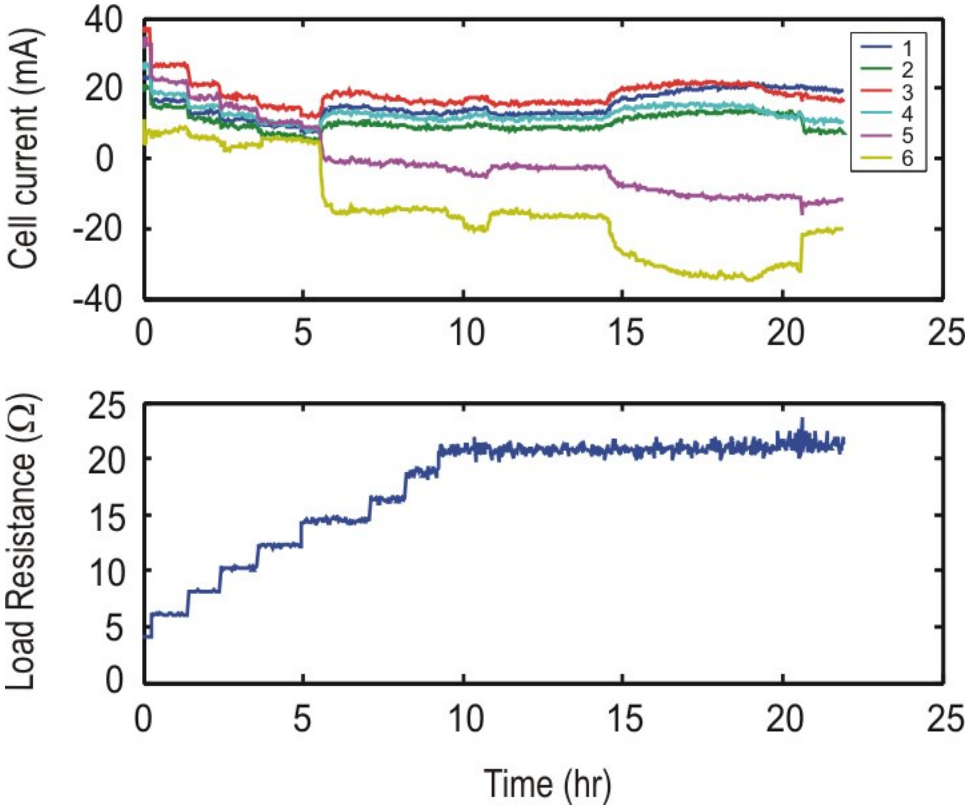

Figure 5.11: The external load resistance effect on current. For a fuel cell with counter-current reactant flow rates of 5 mL/min at 60°C, the external load resistance was manually increased after each hour. We discovered the occurrence of negative currents in the last two segments of the fuel cell.

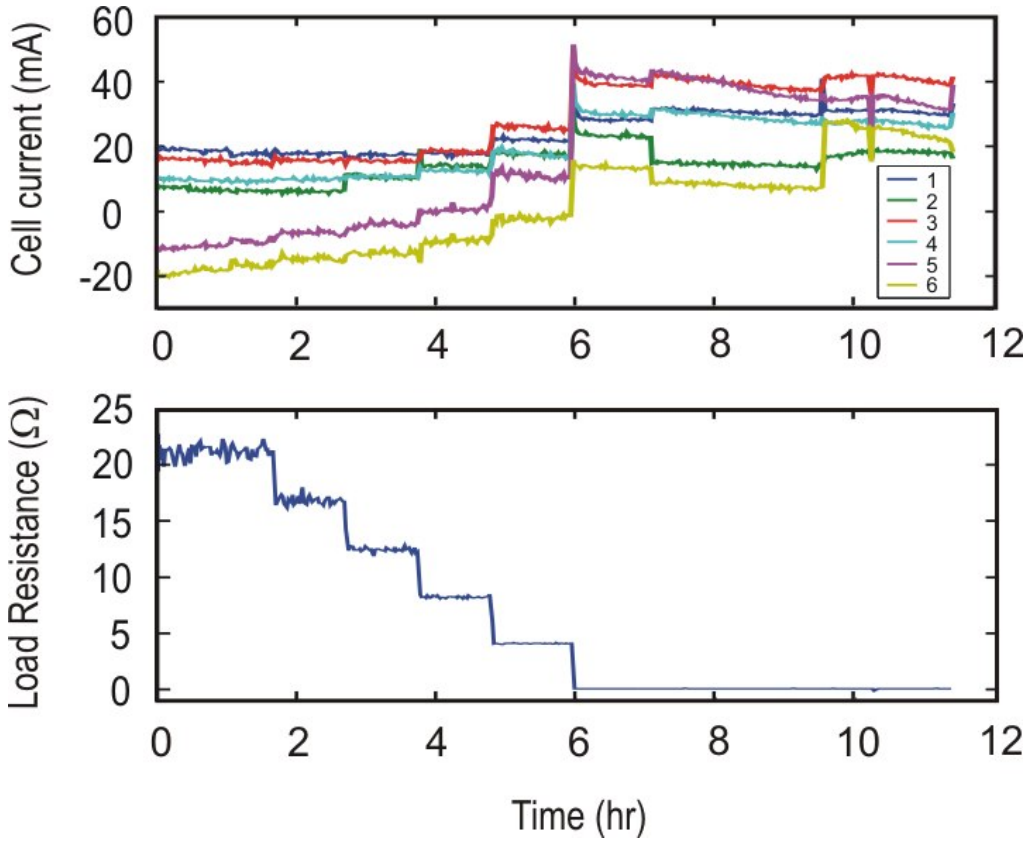

Figure 5.12: The effect of decreasing the external load resistance on the segmented anode fuel cell. Under the same operating conditions (60°C, 5 mL/min reactants) in counter-current flow, the external load resistance was decreased in a stepwise fashion from 20 Ω to 0 Ω. The fuel cell current in segments five and six became less negative with the increasing load resistance and eventually returned to positive at 4 Ω.

As we increased the external load resistance, the current production in each segment decreased, and we inadvertently promoted hydrogen crossover due to the unused hydrogen available in the anode flow channel. Therefore, in the latter experiment where we decreased the external load resistance, we increased hydrogen consumption, reduced hydrogen crossover and returned the fuel cell to its normal state.

5.4.3 Current Oscillations

After tracking the fuel cell response to step changes in the load resistance as described above, we resumed studying the fuel cell extinction front. For the fuel cell with the flow channels in the horizontal orientation, the cell temperature and external load resistance were increased to 75°C and 20 Ω while the hydrogen and oxygen flow rates were 5.2 mL/min and 6 mL/min respectively in co-current scheme. Instead of observing an extinction front, negative currents in tanks 5 and 6 were recorded along with autonomous oscillations in the fuel cell current as shown in Figure 5.13. None of the operating parameters were changed during the duration in which the oscillations were observed. The current oscillations were rather regular with a period of about two hours.

Since the oscillations in current were observed for the horizontally oriented fuel cell, we believe that they arise due to liquid water flowing out of the fuel cell. As mentioned previously, when the flow channels are horizontal, some liquid water might accumulate in the lowest flow channel, creating additional mass transport limitations. During the experiment, plugs of water were observed to periodically flow out of the effluent tubes of the fuel cell. When the plugs of water successfully exit the cell, a rise in the fuel cell current is observed since the mass transport resistance for the reactant is decreased.

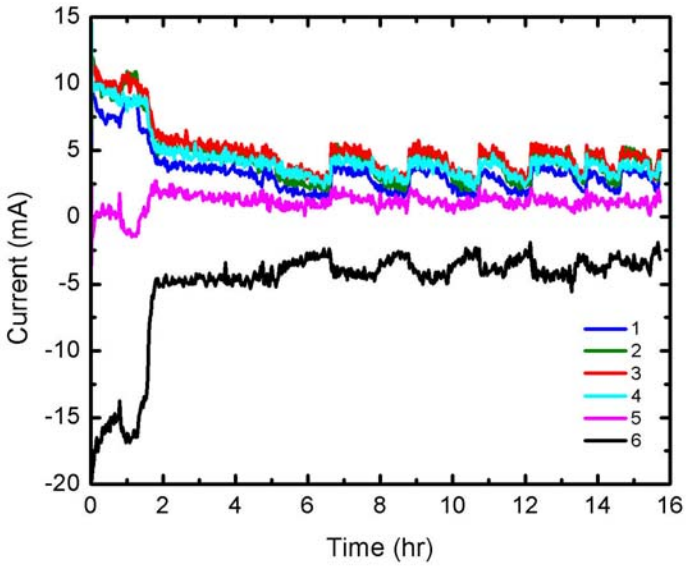

Figure 5.13: Autonomous oscillations observed for the horizontally oriented parallel channel fuel cell with co-current reactant flow rates of 5.2 mL/min of hydrogen and 6.0 mL/min of oxygen. The fuel cell temperature and external load resistance were set to 75°C and 20 Ω.

5.5 Summary

We have introduced here a unique version of the PEM fuel cell which utilizes the features of an STR-PEM fuel cell as an initial approximation of the more common two dimensional serpentine type fuel cells that frequently contain concentration variations over the membrane. By constructing and operating the segmented anode parallel channel fuel cell, we successfully captured the current variations downstream from the anode inlet. This was possible because the segmented graphite pieces in the anode were electrically connected in parallel to each other. Individual measurements of the current in each segment enabled us to observe the power production from the various segments.

From the color plots of current production across the different segments over time, we observed the existence of wet spots (corresponding to regions of large current) in the fuel cell that are analogous to hot spots in the familiar tubular reactor. The segmented anode fuel cell has also provided an exclusive view of the ignition and extinction fronts within the fuel cell. Differences in these fronts depend on the operating conditions (flow rates, operating temperature, external load resistance), the adopted flow pattern (co- or counter-current), as well as the flow channel configuration (horizontally or vertically oriented flow channels).

We have also found that pre-equilibration conditions can affect the ignition profile. While we were often able to extinguish the fuel cell by increasing the temperature, we were not always successful in getting the fuel cell to reignite by lowering the operating temperature. This is attributed to the differences in water content that arise when the fuel cell membrane equilibrates at various operating conditions. Recall that the membrane acts as a reservoir for water and for some instances the membrane water content is

insufficient for ignition to occur. The segmented anode parallel channel fuel cell is advantageous because it enables us to pinpoint which segments are first to ignite and extinguish.

The segmented anode parallel channel fuel cell has provided a remarkable insight into the polymer electrode membrane fuel cell which will aid in efforts to identify optimal operating parameters. Individual current measurements in each segment led to the discovery of negative currents within the fuel cell that are believed to result from hydrogen crossover. If we had only measured the total current, which remained positive during the changes in external load resistance, we would have overlooked this crossover effect inside the fuel cell. Understanding ignition/extinction as well as how the fronts move will enable us to improve the existing fuel cell design. Potential modifications include a distributed feed design where the reactants are fed along different segments of the fuel cell to optimize the utilization.

Chapter 6

Modeling the Tanks in Series Fuel Cell

We have used the single stirred tank PEM fuel cell as a building block to approximate more conventional integral (plug flow) type fuel cell reactors. By connecting several STR-PEM fuel cells in series, the effects of the four operating parameters (temperature, external load resistance, inlet hydrogen and oxygen flow rates) on the current evolution in each tank can be monitored. In the previous chapter, we introduced the segmented anode parallel channel fuel cell as an approximation to the stirred tanks in series PEM fuel cell. Here, we develop the tanks in series (segmented anode parallel channel) model based on a modified version of the existing single stirred tank reactor model presented in Chapter 4.

6.1 The Modified Stirred Tank Reactor PEM Model

Recall that the flow channels are modeled as stirred tank reactors to which hydrogen and oxygen are fed at fixed flow rates of F_A^{in} and F_C^{in}. These inlet flow rates along with both the external load resistance R_L and the fuel cell temperature T are controllable

quantities which appear as operating parameters in our model.* While the current through and the voltage drop across the external load resistance are directly measurable quantities, the membrane resistance R_M is not directly measurable. The membrane resistance represents the resistance to proton transport and is a strong function of water but only weakly dependent on temperature (Eikerling et al., 1997; Hsu and Gierke, 1982; Paddison, 2001; Thampan et al., 2000; Yang, 2003; Yang et al., 2004).

In the modified STR-PEM fuel cell model proposed here, we develop a more detailed view of the cathode so that we may incorporate mass transfer effects there. Specifically, we have focused on modeling four regions within the PEM fuel cell as illustrated in Figure 6.1. This diagram highlights the important mass transport processes occurring within the anode flow channel, membrane, cathode side catalyst/gas diffusion layer, and the cathode flow channel. The variables within each region include the hydrogen and water partial pressures in the anode flow channel, P_{H_2} and P_w^A (Pa), the membrane water activity a_w, the moles of water in gas diffusion layer $n_{w,gdl}$ (mol), and the partial pressures of oxygen and water in the cathode flow channel, P_{O_2} and P_w^C (Pa).

The anode catalyst/gas diffusion layer mass transport effects are lumped into the effective mass transfer coefficient k (1.3 x 10^{-2} mol/m^2-s) that governs the rate of water transport between the membrane and the anode flow channel. This rate of water transport is determined by the gradient in water activity as expressed by

$$kA\left(a_w - a_w^A\right) \tag{6.1}$$

where a_w is the membrane water activity and a_w^A is the anode flow channel water activity.

* For the single fuel cell models, the temperature gradients are small. The assumption of constant temperature must be relaxed for fuel cell stacks.

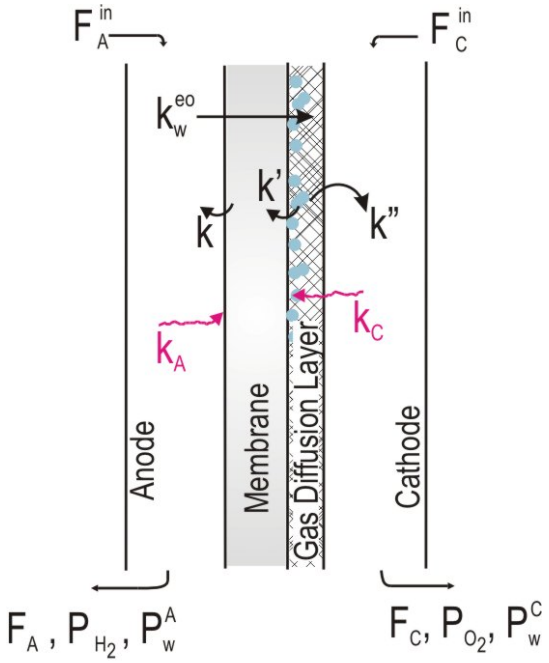

Figure 6.1: Water Transport Processes. The model consists of four regions with water being produced in the cathode catalyst layer (effectively part of the cathode GDL). The anode GDL is ignored here since in these studies the fuel cell operates under dry anode conditions.

The anode flow channel water activity is expressed as the ratio of the water partial pressure in the anode flow channel P_w^A to the water vapor pressure at the fuel cell temperature P_{wo} as

$$a_w^A = P_w^A / P_{wo} \tag{6.2}$$

The model also includes an electro-osmotic drag of water from the anode flow channel through the term $k_w^{eo} \frac{i}{\mathcal{F}}$. The electro-osmotic mass transfer coefficient depends on the water activity in the anode flow as

$$k_w^{eo} = 2(a_w^A)^4 = 2(P_w^A / P_{wo})^4 \tag{6.3}$$

We will refer to the cathode catalyst/gas diffusion layer as the cathode GDL. Water produced at the cathode catalyst (effectively part of the GDL), can enter the membrane or the cathode flow channel. The rate of water transport between the cathode GDL and the membrane depends on the gradient in water activity between the GDL and the membrane as described by

$$k'A\left(a_{gdl} - a_w\right) \tag{6.4}$$

where a_{gdl} is the GDL water activity and k' (5.6 x 10^{-2} mol/m^2-s) is the effective mass transfer coefficient for water transport between the GDL and the membrane. Similarly, water from the GDL is transported to the cathode flow channel at a rate

$$k''A\left(a_{gdl} - a_w^C\right) \tag{6.5}$$

where k'' (1.6 x 10^{-2} mol/m^2-s) is the corresponding mass transfer coefficient. This rate depends on the difference between GDL water activity and cathode flow channel water

activity, a_w^C. The latter can be expressed in terms of the water partial pressure in the cathode flow channel as

$$a_w^C = P_w^C / P_{wo} \tag{6.6}$$

Transport between the four respective regions is summarized in Table 6.1 below.

6.2 Flooding Effects at the Cathode

The mass transfer coefficients that govern the rate of hydrogen transport to the anode catalyst and oxygen transport to the cathode catalyst are k_A (5.8 x 10^{-6} mol/m^2-s-Pa) and k_C (mol/m^2-s-Pa) respectively. At steady state the rate of mass transfer to the catalyst must equal the rate of reaction occurring at the catalyst surface; the reactant partial pressures at the electrode/electrolyte interface $P_{H_2}^{cat}$ and $P_{O_2}^{cat}$ (Pa) are reduced from those in the flow channels due to mass transfer across the GDL and can be expressed as

$$P_{H_2}^{cat} = P_{H_2} - \frac{i}{2\mathcal{F}k_A A} \tag{6.7}$$

$$P_{O_2}^{cat} = P_{O_2} - \frac{i}{4\mathcal{F}k_C A} \tag{6.8}$$

where $\mathcal{F}$ represents Faraday's constant (96,500 C/mol).

Water is produced on the cathode side; we limit our model to conditions where there is no liquid water in the flow channels at the anode side, so that k_A remains constant. At the cathode, our model allows for liquid water to accumulate within the catalyst layer, creating an additional mass transport resistance for O_2. We modeled the decrease in the mass transfer coefficient by assuming that the pores in the cathode GDL will be uniformly filled with water. The oxygen goes through the cathode GDL pores which are

Rate of Transport	Expression
Water transport between the membrane and the anode flow channel	$kA\left(a_w - a_w^A\right)$
Electro-osmotic drag of water from the anode flow channel	$k_w^{eo} = 2(a_w^A)^4 = 2(P_w^A / P_{wo})^4$
Water transport between the cathode GDL and the membrane	$k'A\left(a_{gdl} - a_w\right)$
Water transport from the GDL to the cathode flow channel	$k''A\left(a_{gdl} - a_w^C\right)$
Hydrogen transport to the anode catalyst	$k_A A_{eff}\left(P_{H_2} - P_{H_2}^{cat}\right)$
Oxygen transport to the cathode catalyst	$k_C A_{eff}\left(P_{O_2}^{cat} - P_{O_2}\right)$

Table 6.1: Relevant transport processes in the updated STR-PEM fuel cell model. The model consists of four regions with water being produced in the cathode catalyst layer (effectively part of the cathode GDL). The anode GDL is ignored since the fuel cell operates under dry anode conditions.

filled sequentially with water from the electrode/electrolyte interface to the cathode GDL flow channel interface.

Without liquid water, the mass transfer of oxygen to the catalyst k_C is at the maximum possible rate of $k_C^{\max}$ (5.8 x 10^{-7} mol/m^2-s-Pa). However, k_C decreases significantly at the onset of liquid water formation at the cathode GDL and approaches a minimum rate of $k_C^{\min}$ (5.8 x 10^{-10} mol/m^2-s-Pa) when the GDL is completely filled with liquid water at $n_w^{\max}$ (8.3 x 10^{-4} mol). Here, the maximum moles of water in the gaseous phase is expressed as $n_w^{G,\max} = P_{wo}V_{gdl} / RT$ where V_{gdl} is the GDL volume (7.5 x 10^{-8} m^3). Therefore, k_C is expressed as a function of the moles of liquid water present in the GDL n_w^L (mol) and has values between $k_C^{\min}$ and $k_C^{\max}$ as depicted schematically in Figure 6.2.

$$k_C = \frac{k_c^{\max}}{1 + \frac{n_w^L}{n_w^{\max}}\left(\frac{k_c^{\max} - k_c^{\min}}{k_c^{\min}}\right)} \tag{6.9}$$

The battery voltage V_b depends on the thermodynamic potential at standard conditions V_o (1.23 V), the compositions in both the anode and cathode, and the total pressure in each flow channel P_T (10^5 Pa). The electron transfer reactions at the anode and cathode are equivalent to chemical diodes which capture the typical Butler-Volmer kinetics. From the equivalent electrical circuit, the diode effect is captured in the second term in the following equation (where V_T =0.05 V is the diode threshold voltage while I_o = 0.002 A is the diode saturation current). The effective fuel cell voltage V_{FC} (Volt) is derived electrically as

$$V_{FC} = V_b - V_T ln\left(1 + {}^{i}\!/\!_{I_O}\right) \tag{6.10}$$

where the battery voltage is expressed as

$$V_b = V_o + \frac{RT}{4\mathcal{F}} ln \frac{\left(P^{cat}_{H_2,anode}/P_T\right)^2 \left(P^{cat}_{O_2,cathode}/P_T\right)}{\left(a_{gdl}\right)^2} \tag{6.11}$$

6.3 Mass Balances for the Stirred Tank Reactor PEM

Previously we have shown that the membrane resistance depends strongly on the membrane water activity (Yang, 2003). For a membrane with thickness l (1.27 x 10^{-4} m) and area A (1.5 x 10^{-4} m^2) the membrane resistance is correlated as

$$R_M(a_w) = 10^5 exp(-14a_w^{0.2}) \frac{l}{A} \tag{6.12}$$

Electrically, the fuel cell current (based on Ohm's law) is expressed as

$$i = \frac{V_{FC}}{R_M(a_w) + R_L} \tag{6.13}$$

Writing the mass balances for relevant species in each respective region, we obtain the following set of equations. Equations (6.16) and (6.17) describe the balance of hydrogen in the anode and oxygen in the cathode while equations (6.18) and (6.19) describe the inventory of water in the membrane and GDL respectively.

When there is only water vapor present in the GDL, the water activity is the ratio of the partial pressure of water in the GDL to the water vapor pressure,

$$a_{gdl} = P_w^{gdl}/P_{wo} \tag{6.14}$$

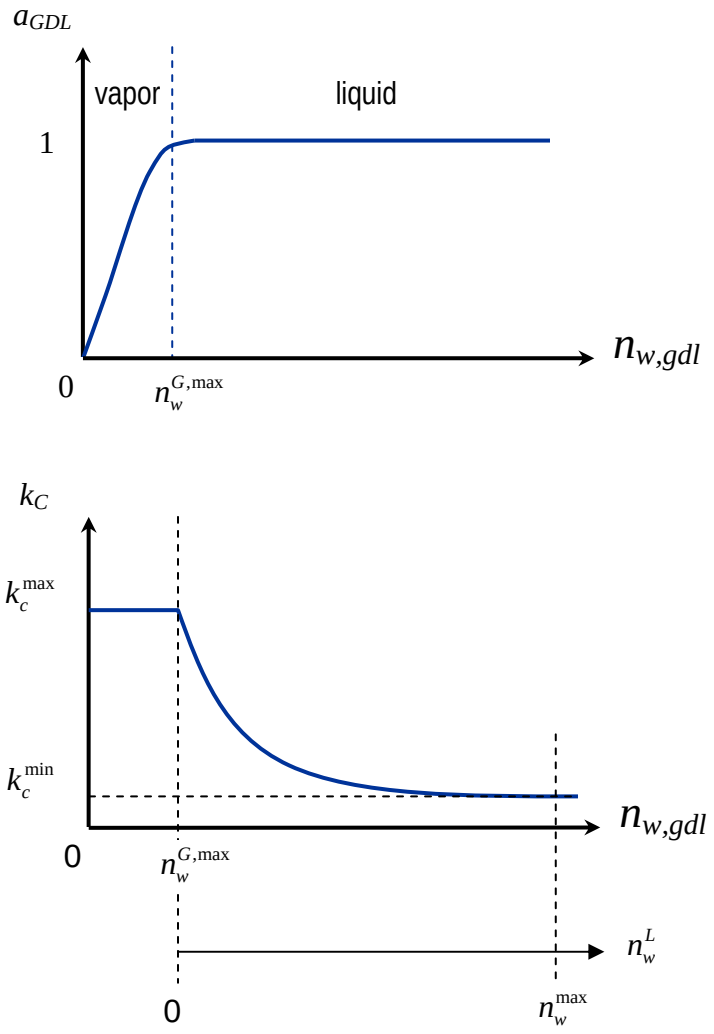

Figure 6.2: Cathode GDL mass transfer. Oxygen mass transport to the cathode electrode decreases rapidly after the onset of liquid water formation. When liquid water appears within the layer (so that a_{gdl} is 1), k_C will start decreasing and eventually will approach $k_C^{\min}$.

The partial pressure of water in the GDL can be related to the moles of water in the GDL ($n_{w,gdl}$) such that the activity can be expressed as

$$a_{gdl} = \left(n_{w,gdl} RT\right) / \left(V_{gdl} P_{wo}\right) \tag{6.15}$$

The GDL water activity is equal to 1 when there is liquid water present (see Figure 6.2). In the following equations, N_{SO_3} is the moles of sulfonic acid groups in the membrane (3.5×10^{-5} mol), λ is the membrane water content defined as the number of water molecules per sulfonic acid group (Yang, 2003), while V_g^A and V_g^C are the anode and cathode flow channel volumes (2×10^{-7} m^3).

$$\frac{V_g^A}{RT}\frac{dP_{H_2}}{dt} = F_A^{in}\frac{P_{H_2}^{in}}{RT} - F_A\frac{P_{H_2}}{RT} - \frac{i}{2\mathcal{F}} \tag{6.16}$$

$$\frac{V_g^C}{RT}\frac{dP_{O_2}}{dt} = F_C^{in}\frac{P_{O_2}^{in}}{RT} - F_C\frac{P_{O_2}}{RT} - \frac{i}{4\mathcal{F}} \tag{6.17}$$

$$N_{SO_3}\frac{d\lambda}{da_w}\frac{da_w}{dt} = k'A(a_{gdl} - a_w) - kA\left(a_w - \frac{P_w^A}{P_{wo}}\right) \tag{6.18}$$

$$\frac{dn_{w,gdl}}{dt} = \frac{i}{2\mathcal{F}} - k'A(a_{gdl} - a_w) - k''A\left(a_{gdl} - \frac{P_w^C}{P_{wo}}\right) + k_w^{eo}\frac{i}{\mathcal{F}} \tag{6.19}$$

Our estimates of the mass transfer coefficients are determined from fitting auto-humidified stirred tank reactor PEM fuel cell data (Moxley et al., 2003). Based on resistances in series, the expressions for the fluxes of water out from the cathode (N_w^C) and anode (N_w^A) can be written as

$$\begin{aligned} k''(a_w^{GDL} - a_w^C) &= N_w^C \\ \frac{kk'}{k+k'}(a_w^{GDL} - a_w^A) &= N_w^A \end{aligned} \tag{6.20}$$

We assumed that liquid water is present in the cathode GDL such that the water activity there is equal to 1. From the experimental data, *k"* and the lumped mass transfer coefficient for *k* and *k'* were determined to be on order of 10^{-6} mol/cm^2-s. This was consistent with the data from Moxley which indicated that the water produced in the fuel cell was equipartitioned between the anode and the cathode.

We will consider the case of constant pressure operation in each flow channel (P_T =10^5 Pa) with pure reactant inlet flow rates specified by F_A^{in} and F_C^{in}. Therefore, the partial pressures of water in the anode and cathode can be expressed as

$$P_w^A = P_T - P_{H_2} \tag{6.20}$$

$$P_w^C = P_T - P_{O_2} \tag{6.21}$$

The exit flow rates on both the anode and cathode sides are F_A and F_C (m^3/s). In the anode, the respective terms in the expression for F_A represent the moles of hydrogen entering the fuel cell, the rate of water transferred between the membrane and the anode flow channel, the rate of water electro-osmotically dragged away from the anode, and the rate of water production. Similarly, F_C in the cathode depends on the moles of oxygen entering the cathode flow channel, the rate of water transferred between the cathode GDL and the cathode flow channel, in addition to the rate of oxygen consumption.

$$F_A = \left[F_A^{in} \frac{P_T}{RT_{in}} + kA\left(a_w - \frac{P_w^A}{P_{w0}} \right) - \frac{i}{\mathcal{F}}\left(k_w^{eo} + 0.5 \right) \right] \frac{RT}{P_T} \tag{6.22}$$

$$F_C = \left[F_C^{in} \frac{P_T}{RT_{in}} + k''A\left(a_{gdl} - \frac{P_w^C}{P_{wo}} \right) - 0.25\frac{i}{\mathcal{F}} \right] \frac{RT}{P_T} \tag{6.23}$$

6.4 The Tanks in Series Model

Figure 6.3 (a) depicts how the STR-PEM fuel cell (a differential element), when connected in series, can be used to model other more complicated flow fields. We will illustrate the flow effects by feeding the reactants from opposite ends (counter-current) and from the same end (co-current). The fuel cells are physically connected in series but electrically, the fuel cell membrane resistances are parallel to each other (see Figure 6.3 (b)). In the co-current flow scheme, the anode and cathode exit streams from tank *j-1* are also the inlet streams into tank *j*. Therefore, the exiting flow rates in the anode and cathode for each tank depend on the flow rates of the previous tank. In addition, water can be transported through the membrane from tank to tank, and the corresponding coupling term is modeled by

$$k_m A_m (a_{w(j-1)} - a_{w(j)}) \tag{6.24}$$

where k_m (0.5 mol/m^2-s) is the mass transfer coefficient for water through the membrane between different tanks and A_m (1 x 10^{-6} m^2) is the cross sectional area of the membrane available for longitudinal water transport.

Similar to the single STR-PEM fuel cell, we operate under constant total pressure such that the partial pressures of water in the anode and cathode for each tank is

$$P^A_{w(j)} = P_T - P_{H_2(j)} \tag{6.25}$$

$$P^C_{w(j)} = P_T - P_{O_2(j)} \tag{6.26}$$

For several STR-PEM fuel cells connected in co-current flow, the equations are written as the following for tanks *j=1* to *j=N*.

$$\frac{V_g^A}{RT}\frac{dP_{H_2(j)}}{dt} = F_{A(j-1)}\frac{P_{H_2(j-1)}}{RT} - F_{A(j)}\frac{P_{H_2(j)}}{RT} - \frac{i_{(j)}}{2\mathcal{F}} \tag{6.27}$$

$$\frac{V_C}{RT}\frac{dP_{O_2(j)}}{dt} = F_{C(j-1)}\frac{P_{O_2(j-1)}}{RT} - F_{C(j)}\frac{P_{O_2(j)}}{RT} - \frac{i_{(j)}}{4\mathcal{F}} \tag{6.28}$$

$$N_{SO_3}\frac{d\lambda}{da_{w(j)}}\frac{da_{w(j)}}{dt} = k'A(a_{gdl(j)} - a_{w(j)}) - kA\left(a_{w(j)} - \frac{P_{wA(j)}}{P_{w0}}\right) + k_m A(a_{w(j-1)} - a_{w(j)}) - k_m A(a_{w(j)} - a_{w(j+1)}) \tag{6.29}$$

$$\frac{dn_{gdl(j)}}{dt} = \frac{i_{(j)}}{2\mathcal{F}} - k'A(a_{gdl(j)} - a_{w(j)}) - k''A\left(a_{gdl(j)} - \frac{P_{wC(j)}}{P_{w0}}\right) + k_{w(j)}^{eo}\frac{i_{(j)}}{\mathcal{F}} \tag{6.30}$$

$$F_{A(j)} = \left[F_{A(j-1)}\frac{P_T}{RT} + kA\left(a_{w(j)} - \frac{P_{w(j)}^A}{P_{w0}}\right) - \frac{i_{(j)}}{\mathcal{F}}\left(k_{w(j)}^{eo} + 0.5\right)\right]\frac{RT}{P_T} \tag{6.31}$$

$$F_{C(j)} = \left[F_{C(j-1)}\frac{P_T}{RT} + k''A\left(a_{gdl(j)} - \frac{P_{w(j)}^C}{P_{w0}}\right) - 0.25\frac{i_{(j)}}{\mathcal{F}}\right]\frac{RT}{P_T} \tag{6.32}$$

$$V_{FC(j)} = V_o + \frac{RT}{4\mathcal{F}}\ln\frac{\left(P_{H_2(j)}^{cat}/P_T\right)^2\left(P_{O_2(j)}^{cat}/P_T\right)}{\left(a_{gdl(j)}\right)^2} - V_T\ln\left(1 + {}^{i_{(j)}}\!/_{I_o}\right) \tag{6.33}$$

$$i_{(j)} = \frac{V_{FC(j)} - V}{R_{M(j)}} \tag{6.34}$$

$$V = R_L\sum_{j=1}^{N} i_{(j)} \tag{6.35}$$

6.5 Results

6.5.1 The Single Stirred Tank Reactor

The STR-PEM fuel cell will equilibrate to different steady states depending on the operating conditions. Increasing the temperature would increase the rate of water removal while increasing the load resistance would decrease the rate of water production.

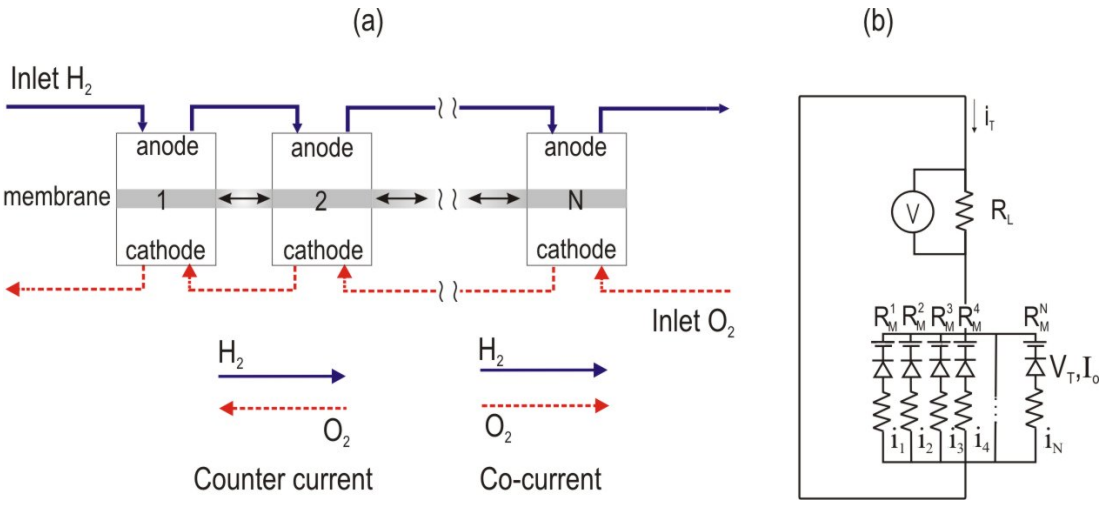

Figure 6.3: Building blocks. (a) Several STR-PEM fuel cells can be connected in series to approximate more complicated, spatially distributed, flow schemes; (b) STR-PEM fuel cell electrical circuit equivalent, with the fuel cell membrane resistances electrically connected in parallel to one another.

In Figure 6.4, we study a single STR-PEM fuel cell, which has initially been equilibrated to a steady state membrane water content of a_w = 0.1. The fuel cell was then set to operate at 353 K with 8.33 x 10^{-8} m^3/s reactant feed flow rates for two different load resistances: 5 Ω and 3 Ω. As shown in Figure 6.4(c), a lower steady state current is achieved when operating the fuel cell at R_L=5 Ω in comparison to R_L=3 Ω. Although the 3 Ω case yields a larger steady state current, partial flooding effects in the cathode GDL impede oxygen transfer to the catalyst surface. The onset of liquid water formation as depicted in Figure 6.4(a) is accompanied by a distinct drop in $P_{O_2}^{cat}$ in Figure 6.4(b).

From continuation techniques in the software AUTO, we determined regions of multiplicity in parameter space (the four controllable parameters T, R_L, F_A^{in}, F_C^{in}). The results are presented in three two-parameter bifurcation diagrams (T and R_L in Figure 6.5 (a), T and F_A^{in} in Figure 6.5 (b), F_C^{in} and F_A^{in} in Figure 6.6 (a)). Regions of three steady states are marked by III while regions with only one steady state are indicated by I. Bifurcation results from the current model (solid lines) are plotted in comparison to the results from the initial model (dotted line) (Chia et al., 2004). The multiplicity regions from the current, augmented model correspond more closely to experimentally observed regions in parameter space, suggesting an improvement from previous work.

Selected parameter cuts across the two-parameter diagrams, illustrating the ignition-extinction transitions, are included in Figures 6.5 (c) and 6.6 (b). The solid curves in the one parameter cuts represent stable steady states while the dashed curves represent unstable steady states. For low temperatures or low inlet oxygen flow rates, the current in the upper stable branch is observed to decrease due to the flooding in the cathode GDL. Since the stable steady states can be determined experimentally, one could generate the

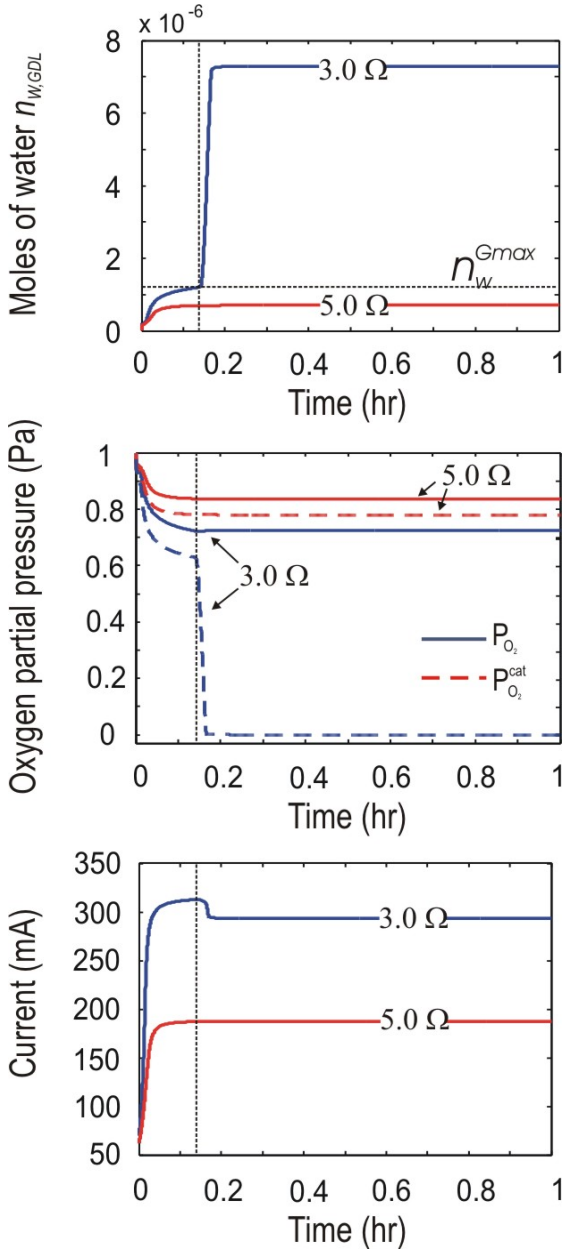

Figure 6.4: Flooding effects in the cathode. The transient fuel cell behavior at R_L=5 Ω (dry cathode) and R_L=3 Ω (wet cathode); T=353 K; $F_A^{in}=F_C^{in}=8.33 \times 10^{-8}$ m^3/s. For the 3 Ω case: (a) The onset of liquid water formation; (b) The presence of liquid water leads to a drop in $P_{O_2}^{cat}$; (c) The current decreases due to the limited oxygen reaching the catalyst surface.

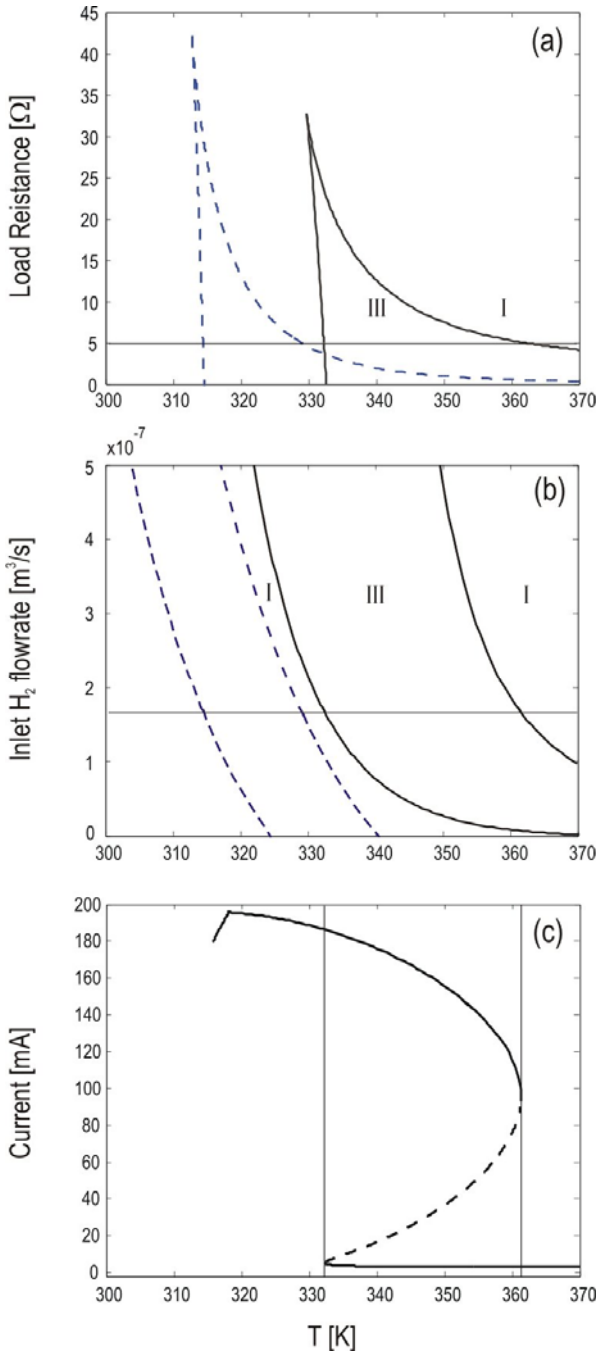

Figure 6.5: Two-parameter bifurcation diagrams for the single STR-PEM fuel cell with GDL flooding. (a) T and R_L [F_A^{in} = 1.67 x10^{-7} m^3/s, F_C^{in} = 2.5 x10^{-7} m^3/s]; (b) T and F_A^{in} [F_C^{in} = 2.5 x10^{-7} m^3/s, R_L = 5 Ω]; (c) Corresponding one parameter continuation for R_L = 5 Ω, marked in panel (a) [F_A^{in} =1.67 x10^{-7} m^3/s, F_C^{in} = 2.5 x10^{-7} m^3/s]. Solid (dashed) curves denote stable (unstable) steady states.

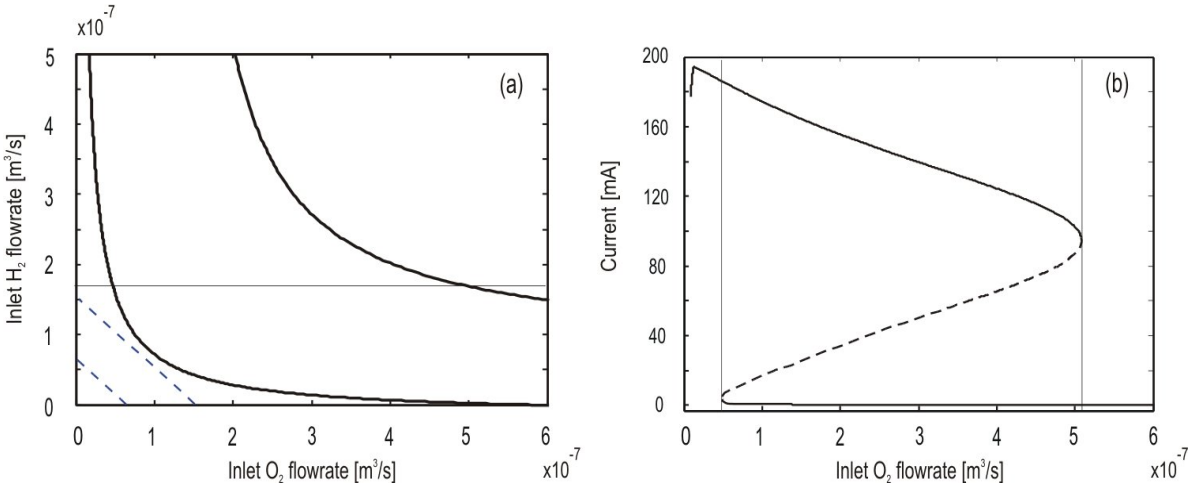

Figure 6.6: Two parameter bifurcation diagram for the single STR-PEM fuel cell with GDL flooding. (a) F_A^{in} and F_C^{in} [T=353 K, R_L = 5 Ω]; the region of steady state multiplicity lies between the curve pairs (curves of saddle-node bifurcations); (b) Representative one parameter continuation in F_C^{in} for F_A^{in}=1.67 x10^{-7} m^3/s as marked in (a) where solid (dashed) curves denote stable (unstable) steady states.

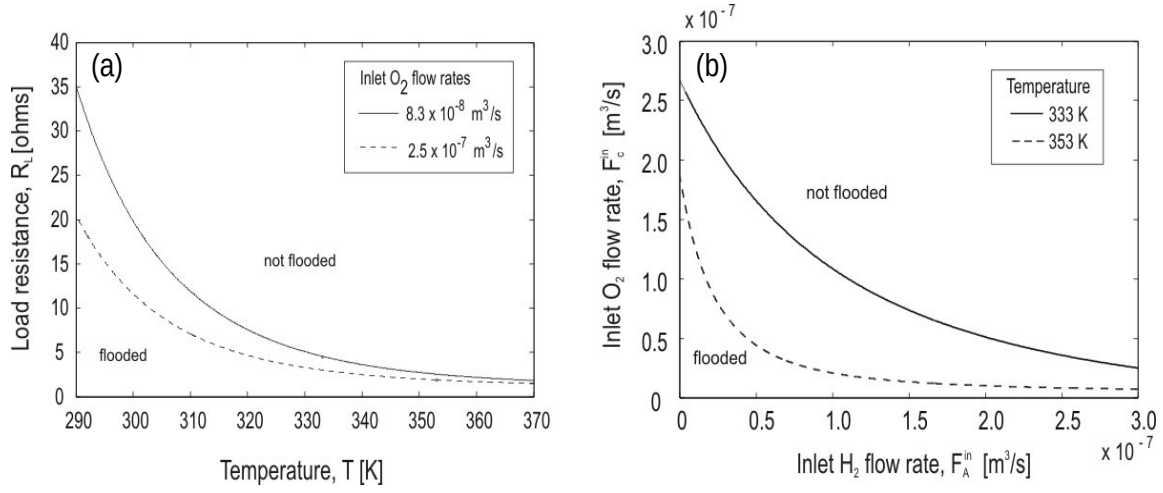

Figure 6.7: Flooding Regions in Parameter Space.
(a) T and R_L [F_A^{in}=1.67 x10^{-7} m^3/s] (b) F_A^{in} and F_C^{in} [R_L = 5 Ω]

stable branches of these one parameter cuts by manually changing one of the controllable parameters slowly. The fuel cell would then be allowed to equilibrate to the new controllable parameter before the current is recorded.

We have also identified regions in parameter space where flooding occurs via continuation. In Figure 6.7, the lines represent the onset of flooding boundary and correspond to conditions where the water activity in the cathode GDL, a_{gdl} is equal to 1. From Figure 6.7 (a), we observe that we can avoid flooding by operating the fuel cell with larger inlet oxygen flow rates F_C^{in}. From Figure 6.7 (b), we see that the flooded region decreases significantly when the fuel cell temperature is increased. These diagrams indicate that both higher operating temperatures and larger flow rates facilitate water removal, thereby reducing the flooded region. Overall, the continuation results obtained based on the model are important in helping us determine suitable experimental operating conditions for the fuel cell

6.5.2 Multiple STR-PEM fuel cells in series

In the case of several connected STR-PEM fuel cells, the flow pattern alone can change the current profiles in the tanks. In Figure 6.8, we present data for two STR-PEM fuel cells connected in series operating under co-current flow and counter-current flow. The fuel cells have been pre-equilibrated to a membrane water content of a_w = 0.1 before operating at T=353 K, R_L=5 Ω, $F_A^{in} = F_C^{in}$ =1.67 x 10^{-7} m^3/s. Under these conditions, although both flow patterns lead to the same total current (155 mA), the current profiles differ significantly. For the co-current flow, the current in the second tank evolves to a much larger current (124 mA) in comparison to the current in the first tank (31.2 mA)

.

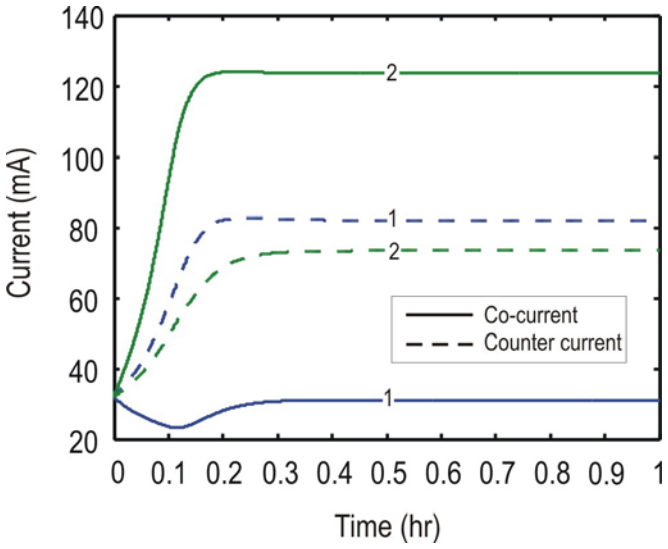

Figure 6.8: Flow pattern effect on ignition for two STR-PEM fuel cells in series [T=353 K; R_L=5.0 Ω; F_A^{in}= 1.67 x10^{-7} m^3/s; F_C^{in}= 1.67x10^{-7} m^3/s]. Current profiles for tanks 1 and 2 in the co-current and counter-current flow scheme.

In contrast, for counter-current flow, the currents in both tanks evolve closer together and at steady state, the currents in the first and second tanks are 82 mA and 73.4 mA respectively. These effects arise because the flow pattern affects the water content in the membrane. The counter-current flow scheme sustains a higher water content in the fuel cell, since water produced in tank 2 is brought back into tank 1 and successfully prevents the current in tank 1 from extinguishing.

Using several STR-PEM fuel cells in series, we demonstrate that we can alter the ignition locations and form wet spots at different locations in the fuel cell array. For a series of six STR-PEM fuel cells in co-current flow (at T =338 K, $F_A^{in} = F_C^{in}$ =1.33 x 10^{-7} m^3/s), with each tank initially pre-equilibrated at a membrane water content of a_w = 0.1, we observe the current evolution for all six tanks under two different loads, R_L=6 Ω and R_L=3 Ω. As expected, a larger total current (325 mA) is observed for the smaller load of 3.0 Ω, in contrast to the total current for 6 Ω (157 mA). However, it is interesting to see that the current profiles are very different for both load resistance values.

In Figure 6.9 (a), the steady state current is largest in the last tank and lowest in the first. In contrast, when the tanks are operating at 3 Ω, the steady state current is smallest in the last tank and largest in tank 2. The difference in the current profiles is the result of different membrane water contents along the cell array. The water activities at the cathode GDL (a_{gdl}) are equal to 1 when there is liquid water present in the GDL. At 6 Ω, all six tanks remain dry, but at 3 Ω, partial flooding occurs initially in the last tank, as indicated by the sudden increase in $n_{w,gdl}$ for tank 6 in Figure 6.9 (c). The increased liquid water level propagates to tank 5 and subsequently even tanks 4 and 3 flood partially.

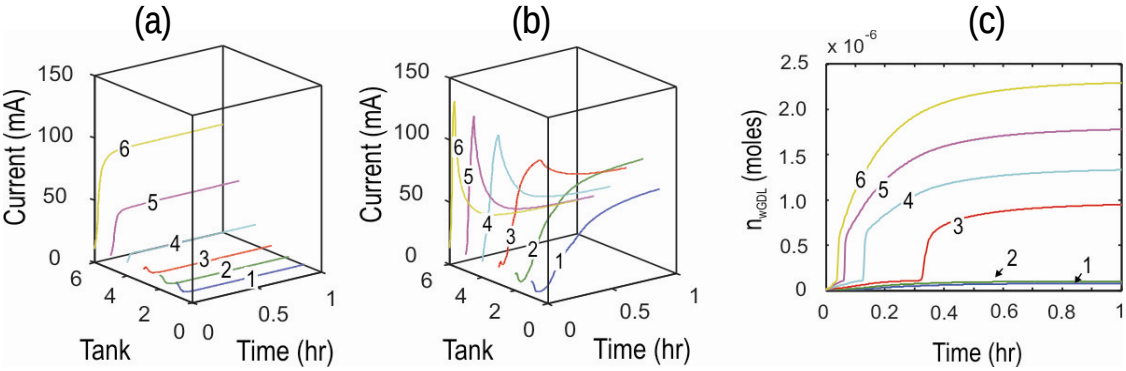

Figure 6.9: Six tanks in *co-current* flow. Transient current profiles (T=338 K; $F_A^{in}=F_C^{in}=1.33 \times 10^{-7}$ m^3/s) in each tank for: (a) R_L=6 Ω, all tanks remain dry; (b) R_L=3.0 Ω, current decreases in the end tanks; (c) R_L=3 Ω, liquid water formation occurs initially in the tanks at the outflow end.

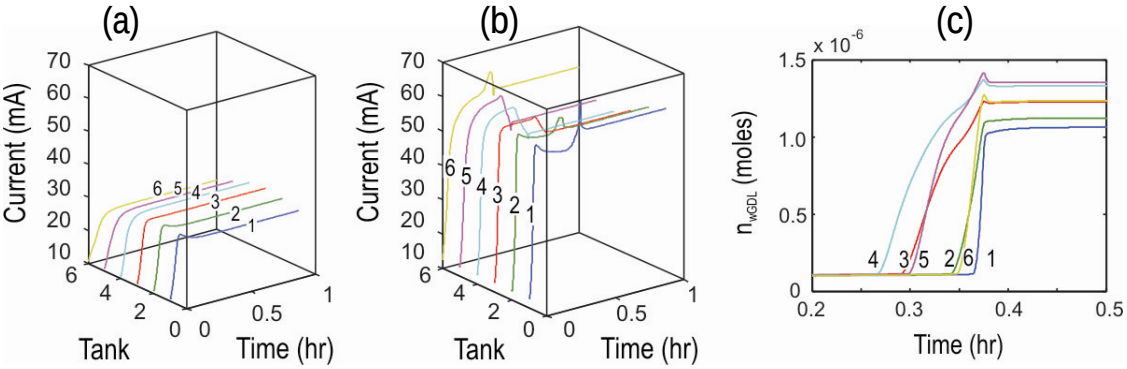

Figure 6.10: Six tanks in *counter-current* flow. Transient current profiles (T=338 K; $F_A^{in}=F_C^{in}=1.33 \times 10^{-7}$ m^3/s) in each tank for (a) R_L=6 Ω: all tanks remain dry; (b) R_L=3 Ω current decreases in the middle tanks; (c) R_L=3 Ω: liquid water first forms in the tanks in the middle.

The steady state current in tanks 3, 4, 5, and 6 are much lower in comparison to the steady state current obtainable from these tanks had they remained dry.

The current evolution also differs between the 6 Ω and 3 Ω cases in a counter-current scheme with the same initial membrane water content in each tank (a_w = 0.1). For the fuel cell operating at 6 Ω, as shown in Figure 6.10(a), the steady state currents in all six tanks are smaller in comparison to the currents in Figure 6.10(b). For the lower load resistance of 3 Ω, the steady state currents in the middle of the array (tanks 3, 4 and 5) are lower in comparison to the currents in the tanks at the array ends. In the counter-current scheme, flooding initially occurs in the middle, beginning in tank 4. Although some tanks are partially flooded, the level of liquid is not enough to completely flood the GDL and inhibit all oxygen transport to the catalyst (and subsequently extinguish the current).

6.5.3 Computational Ignition Fronts

Figures 6.11(a) and (b) are current profiles for a six cell array segmented anode parallel channel fuel cell in co-current and counter-current flow based on the model. The model results were obtained at 328 K and 5 Ω external load, with flow rates of 8.33 x 10^{-8} m^3/s and 1.17 x 10^{-7} m^3/s of hydrogen and oxygen respectively. For both flow regimes, the model successfully captures the ignition point and front propagation. Similar to the experimentally observed ignition fronts presented in Chapter 5, the model results show that when the gas flow is co-current, ignition occurs at the outlet of the flow channel. On the other hand, when the gas flow is counter-current, ignition occurs in the middle of the cell and propagates sideways.

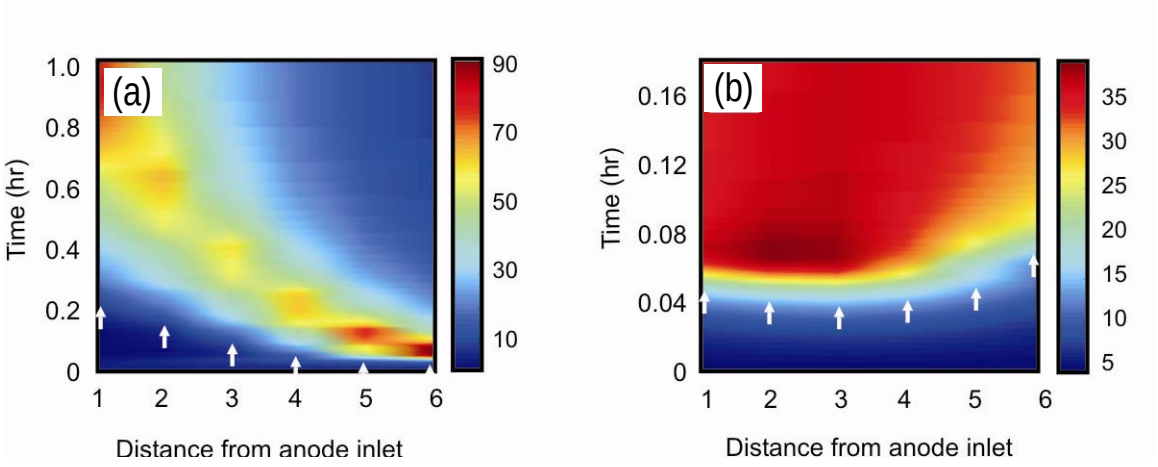

Figure 6.11: The computed ignition fronts in a segmented anode PEM fuel cell for co-current and counter-current flow. In co-current flow the current ignites at the exit to the flow channels and propagates upstream to the flow channel entrance. In counter-current flow ignition occurs at the center of the flow channels.

In co-current flow, the small amount of water produced upstream is conducted towards the outlet where it slowly accumulates in the membrane. When the water content increases to the point where the local membrane resistance becomes comparable to the external load resistance the current increases rapidly, hydrating the membrane and causing ignition. The water activity in the membrane approaches unity and liquid water begins to accumulate in the cathode GDL. The water in the membrane moves upstream through the membrane itself, causing the ignition to propagate upstream. The current subsequently decreases in the downstream part of the fuel cell because liquid water accumulates in the cathode GDL causing the current to decrease in the downstream elements.

When the gases flow in counter-current fashion, the water formed at the cathode is carried towards the anode inlet in the cathode flow channel. At the same time water formed at the cathode is transported across the membrane to the anode where it is transported towards the anode outlet by convection. Water accumulates fastest towards the middle of the flow channels which results in ignition at the center. Changing the ratio of the flow rates between the anode and cathode will shift the ignition point; increasing the anode flow rate relative to the cathode flow rate shifts the ignition point towards the anode outlet. After ignition, water accumulates in the cathode GDL and the membrane. The transport of water through the membrane from high concentration at the middle of the flow channel towards the ends results in the ignition fronts fanning out.

The model does not capture all the features of the experiment; in particular the experiment and model deviate at longer times after ignition. Liquid water was observed leaving the flow channels 30-40 minutes after ignition. Gravity plays a key role in how

the liquid water moves through the flow channels and can alter the results dramatically if the gas flow in the flow channel is counter to the liquid flow due to gravity. The model only considers conditions with water vapor up to where the GDL fills with liquid, but water does not enter the flow channel. Thus the model can capture the ignition and front propagation, but the model begins to break down at longer times when liquid water forms in the flow channels. The model simulations were done at a higher temperature than the experiment because at 298 K the model could not properly account for the predicted liquid water.

6.6 Summary

Previously (Benziger et al., 2004; Chia et al., 2004) we had shown, through a simplified yet physically reasonable model of the STR-PEM fuel cell, that steady state multiplicity occurs in the cell due to the autocatalytic nature of the water transport coupled to the water production. Here, we have extended the model so that it retains the multiplicity features of the original model while accounting for key transport processes in the fuel cell. Incorporating mass transport processes in the gas diffusion layer accounts more realistically for current drops that are a result of an increased mass transport resistance due to flooding. We have also demonstrated (through both the single and multiple STR-PEM fuel cells in series) that the cathode GDL flooding is marked by an increased level of liquid water which obstructs the mass transfer of oxygen to the cathode catalyst surface. Multiple tanks in series studies are able to capture flow pattern effects on the cell dynamics. Using arrays of several tanks in series, we were able to detect current het-

erogeneities along the cell array; regions of higher current correspond to wet spots in the fuel cell array. Ignition/extinction phenomena as observed through the updated STR-PEM fuel cell model depend on the controllable parameters (T, R_L, F_A^{in}, F_C^{in}). Parametric continuation computations offer insight into suitable operating parameter settings by identifying the flooding regions in parameter space.

The water balance in the STR-PEM fuel cell is analogous to the heat balance in the autocatalytic CSTR. By extending our *differential* model to the tanks in series scheme, we are able to mimic the *integral* reactor; we see that the flow pattern alone is capable of determining whether or not the fuel cell can sustain a sufficient level of water to ensure ignition (operation at a high steady state current). We have demonstrated the occurrence of high water content regions within the STR-PEM fuel cell (wet spots) that are directly analogous to high temperature regions (hot spots) in the classic tubular reactor. Changing the flow pattern, in addition to manipulating the controllable parameters, can alter the spatial location of the transient ignitions as well as the ultimate steady state current pattern in a cell array. Initial experimental observations appear to support these theoretical predictions (Benziger et al., 2005b).

Chapter 7

Conclusion

We have studied the PEM fuel cell from a chemical reaction engineering perspective and have developed a differential (stirred tank reactor) version of the fuel cell through both experimental and computational work. The simplicity of the STR-PEM fuel cell enables us to focus on the essential physics that give rise to rich dynamical behavior resulting from the balance between water production and water removal in the fuel cell. This balance is remarkably analogous to the heat balance in the classical exothermic stirred tank reactor (Aris, 1965; Perlmutter, 1972; Schmitz, 1975; Uppal et al., 1974; van Heerden, 1953). Water production within the fuel cell improves proton transport through the membrane and thereby autocatalytically accelerates the reaction. We have shown that the unique balance between water production and water removal in the STR-PEM fuel cell gives rise to multiple steady states – as indicated by the intersections of both the water removal and water production curves.

The dynamic STR-PEM fuel cell responses to changes in operating parameters (external load resistance, operating temperature, reactant feed flow rates) are indicative of

the membrane's role as a reservoir for water. Several characteristic times are associated with the various physical processes in the fuel cell. The characteristic times for water absorption into the membrane and water produced to cross the membrane are on the order of hundreds of seconds. These characteristic times are most notable because they are contrary to the common assumption that PEM fuel cell response times are instantaneous. The experiments affirm that the balance between water removal and water production are disrupted when any operating parameter is altered, resulting in a different membrane water content – extinction is possible if the membrane water activity is not sufficiently high. Another remarkable experimental finding is the occurrence of autonomous oscillations within a range of operating parameters. The oscillations arise due to the interplay between the polymer membrane relaxation and membrane electrode interfacial resistance. The novel STR-PEM fuel cell design allows us to observe these oscillations since the spatial variations are uncoupled from the temporal ones.

As an initial approximation of the conventional serpentine type PEM fuel cell, the STR-PEM fuel cell was used as a building block in a *tanks in series* mode to capture current variations between tanks (that mimic spatial variations downstream). This was implemented via a segmented anode parallel flow channel fuel cell design. In addition to the operating conditions, the reactant flow pattern (co- or counter-current) and the flow channel orientation (horizontal or vertical) were observed to affect the current profiles and ignition in the fuel cell. The experimental results showed that current variations downstream from the anode inlet exist and also indicated that the ignition profiles in co-current and counter-current flows are different. In the co-current scheme, ignition occurs at the segment farthest away from the reactant inlet and propagates towards the front of

the cell. In contrast, in counter-current flow, ignition started from the middle segment and fanned out towards the sides.

In the modeling aspect of our work, by extending the classic exothermic stirred tank reactor to one that is based on water production and water removal in the STR-PEM fuel cell, our mathematical model captured the experimentally observed steady state multiplicity. A positive feedback on the transport effects in the fuel cell is analogous to the positive feedback on the reaction kinetics in the exothermic stirred tank reactor. As the reaction proceeds, the increased water production humidifies the membrane, resulting in greater proton conductivity which drives the reaction even further. Thus the autocatalyticity in the fuel cell model is captured though the strong dependence of the membrane conductivity on the membrane water content. Regions of multiplicity were identified via continuation in the operating parameters.

Our initial STR-PEM fuel cell model was later modified to incorporate key mass transport processes in the cathode side catalyst/gas diffusion layer. Flooding effects were incorporated based on the assumption that water uniformly fills the pores in the cathode GDL. In a subsequent extension, the modified model was also employed as a building block in the tanks in series scheme to mimic the integral type PEM fuel cell. In comparison to existing gas diffusion layer models (Jeng et al., 2004; Lin et al., 2004; Pasaogullari and Wang, 2004), our methodology was a simpler and more straightforward approach which enabled us to study the PEM fuel cell dynamics.

We have demonstrated that the cathode GDL flooding is marked by the increased level of liquid water which prevents the mass transfer of oxygen to the cathode catalyst surface. We have also offered more insight into suitable operating parameters by identi-

fying the onset of flooding in parameter space. Consistent with the experimental results from the segmented anode parallel channel fuel cell presented in Chapter 5, high water content regions in the tanks in series scheme are observed. These high water content regions (wet spots) are directly analogous to high temperature regions (hot spots) in the classic tubular reactor. One may easily change the flow pattern to alter the ignition locations.

Once again, it is the strong exponential dependence of the proton conductivity with membrane water content in the polymer electrolyte membrane in addition to the dynamics of water absorption into the membrane itself that successfully captures the ignition and front propagation effects. The model reaffirms that variations in the current density along the fuel cell flow channels and the local water content in the polymer membrane exist. The model predictions for the effects of reactant flow rates, cell temperature and load resistance on ignition are qualitatively consistent with the experimental results. The model is only semi-quantitative because the variability of the membrane-electrode-assemblies alters the electrode/electrolyte interfacial resistance and gas transport between the flow channels and the electrode/electrolyte interface. The model also does not account for liquid water in the flow channels.

Although the segmented anode parallel channel version of the STR-PEM fuel cell captures the current variations downstream, there are several limitations to the present design. During the segmented anode operation, we observed plugs of liquid water exiting in the effluent tubes. When the flow channels were positioned horizontally, it was hardest for liquid water accumulated in the lowest channel to flow out of the cell, creating a region of high oxygen mass transport resistance. This undesirable water accumulation in

the lowest channel is largely due to the inlet and outlet tubing being positioned on the same level as the center flow channel. While switching the flow channel orientation to a vertical one was a remedy, a future design with a single flow channel would be optimal. In addition, the fuel cell should be designed with larger aluminum and graphite dimensions so that it is easier to handle. The small graphite inserts in the anode were prone to chipping and cracking. A systematic study of the operating parameter effects on ignition and extinction profiles in addition to steady state operation should be conducted for the newer design.

From a modeling perspective, to make the model another step closer to the experimentally operated fuel cell, the model should include the fuel cell configuration effects on the operation. A future modification of the model should incorporate gravitational effects that arise when the flow channel is oriented vertically. The gravitational term should capture the effects of water flowing out of the fuel cell in the vertical orientation.

Since the cathode GDL flooding in the current model is based on the assumption that the GDL pores are uniformly filled with water, it would be interesting to see whether a different pore filling mechanism would be more appropriate (Benziger et al., 2005a). For example, the larger pores can be modeled to fill up faster than the smaller pores, making reactant transport through the smaller pores still feasible. This would account for the conditions where some pores are partially flooded and other pores remain dry.

Although it would be desirable to incorporate the oscillatory behavior into the model, a more systematic experimental study of the oscillations is needed. In addition, a better understanding of membrane swelling and relaxation is necessary before the kinet-

ics associated with these processes can be extracted. The membrane behavior should be characterized under similar confined conditions because the actual Nafion membrane in a fuel cell remains sandwiched between the electrodes and graphite plates. A potential method would be to use magnetic resonance imaging of an operating fuel cell to specifically focus on the Nafion membrane.

However, the PEM fuel cell need not be limited to the Nafion membrane alone. In fact, the STR-PEM fuel cell is versatile enough to accommodate other membrane electrode assemblies. Recent work in our group with composite membranes has shown quite promising results. Therefore, it would also be interesting to see how the current profiles along the membrane differ in comparison to the conventional Nafion membrane. In addition, one can also study whether the autonomous oscillations are observed with composite membranes.

From both the experimental and modeling efforts for the tanks in series fuel cell, the ignition locations differed depending on the flow scheme (co- versus counter-current). In addition to the flow pattern effects, it would be interesting to have a systematic study of humidification effects on the ignition location. The anode reactant feed (hydrogen) can be humidified to various levels by passing the reactant into a heated bubbler before it is fed into the anode.

Although we have used the STR-PEM fuel cell as a tool to observe the rich dynamical behavior, the fuel cell can be made applicable to conventional demands. A control loop can be implemented around the fuel cell to study how the reactant feeds should be regulated to maintain a desired current (meet a power requirement) (Benziger et al., 2005b).

References

"EG&G Services, Parsons, Inc," Fuel Cell Handbook (Fifth Edition), U.S Department of Energy, Morgantown, 2000.

Acres, G. K., "Recent advances in fuel cell technology and its applications," *J. of Power Sources*, 100, 60-66, 2001.

Agrawal, R., Offutt, M., and Ramage, M. P., "Hydrogen Economy - An Opportunity for Chemical Engineers?," *AIChE J*, 52(6), 1582-1589, 2005.

Amphlett, J. C., Baumert, R. M., Mann, R. F., Peppley, B. A., Roberge, P. R., and Rodrigues, A., "Parametric Modeling of the Performance of a 5-Kw Proton-Exchange Membrane Fuel-Cell Stack," *J. of Power Sources*, 49(1-3), 349-356, 1994.

Amphlett, J. C., Mann, R. F., Peppley, B. A., Roberge, P. R., Rodrigues, A., and Salvador, J. P., "Simulation of a 250 kW diesel fuel processor PEM fuel cell system," *J. Power Sources*, 71(1-2), 179-184, 1998.

Aris, R., *Introduction to the Analysis of Chemical Reactors*, Prentice-Hall, Englewood Cliffs, 1965.

Balakotaiah, V., and Luss, D., "Exact Steady-State Multiplicity Criteria for Two Consecutive or Parallel Reactions in Lumped-Parameter Systems," *Chem. Eng. Sci*, 37, 443, 1982a.

Balakotaiah, V., and Luss, D., "Structure of the Steady-state Solutions of Lumped-Parameter Chemically Reacting Systems," *Chem. Eng. Sci*, 37, 1611, 1982b.

Baughman, R. H., Zakhidov, A. A., and de Heer, W. A., "Carbon nanotubes - the route toward applications," *Science*, 297(5582), 787-792, 2002.

Benziger, J., Chia, E., Moxley, J. F., and Kevrekidis, I. G., "The dynamic response of PEM fuel cells to changes in load," *Chem. Eng. Sci*, 60(6), 1743-1759, 2005a.

Benziger, J., Chia, E. J., and Kevrekidis, I. G., "Ignition Front Propagation in Polymer Electrolyte Membrane Fuel Cells," (in preparation), 2005b.

Benziger, J., Nehlsen, J., Blackwell, D., Brennan, T., and Itescu, J., "Water flow in the gas diffusion layer of PEM fuel cells," *J. Membrane Science*, 261(1-2), 98-106, 2005c.

Benziger, J. B., Bocarsly, A., Chia, E. J., and Kevrekidis, I. G., "A Lumped Parameter Dynamic Model of the Water Balance in a PEM Fuel Cell," *J. Power Sources*, submitted.

Benziger, J. B., Chia, E. J., Karnas, E., Moxley, J., Teuscher, C., and Kevrekidis, I. G., "The Stirred Tank Reactor Polymer Electrolyte Membrane Fuel Cell," *AIChE J.*, 50(8), 1889-1900, 2004.

Benziger, J. B., Satterfield, M. B., Hogarth, W. H. J., Nehlsen, J. P., and Kevrekidis, I. G., "The power performance curve for engineering analysis of fuel cells," *J. Power Sources*, (in press), 2005d.

Bernardi, D. M., "Water-Balance Calculations for Solid-Polymer-Electrolyte Fuel-Cells," *J. Electrochem. Soc.*, 137(11), 3344-3350, 1990.

Bernardi, D. M., and Verbrugge, M. W., "Mathematical-Model of a Gas-Diffusion Electrode Bonded to a Polymer Electrolyte," *AIChE J*, 37(8), 1151-1163, 1991.

Bernardi, D. M., and Verbrugge, M. W., "A Mathematical-Model of the Solid-Polymer-Electrolyte Fuel-Cell," *J. Electrochem. Soc.*, 139(9), 2477-2491, 1992.

Bevers, D., Wohr, M., Yasuda, K., and Oguro, K., "Simulation of a polymer electrolyte fuel cell electrode," *J. of App. Electrochem.*, 27(11), 1254-1264, 1997.

Bogdanovic, B., Brand, R. A., Marjanovic, A., Schwickardi, M., and Tolle, J., "Metal-doped sodium aluminium hydrides as potential new hydrogen storage materials," *J. of Alloys and Compounds*, 302(1-2), 36-58, 2000.

Chambers, A., Park, C., Baker, R. T. K., and Rodriguez, N. M., "Hydrogen storage in graphite nanofibers," *J. Phys. Chem. B*, 102(22), 4253-4256, 1998.

Chia, E. J., Benziger, J. B., and Kevrekidis, I. G., "Water Balance and Multiplicity in a Polymer Electrolyte Membrane Fuel Cell," *AIChE J.*, 50(9), 2320-2324, 2004.

Chu, D., and Jiang, R. Z., "Comparative studies of polymer electrolyte membrane fuel cell stack and single cell," *J. Power Sources*, 80(1-2), 226-234, 1999.

Deluga, G. A., Salge, J. R., Schmidt, L. D., and Verykios, X. E., "Renewable Hydrogen from Ethanol by Autothermal Reforming," *Science*, 303, 993-997, 2004.

Dillon, A. C., Jones, K. M., Bekkedahl, T. A., Kiang, C. H., Bethune, D. S., and Heben, M. J., "Storage of hydrogen in single-walled carbon nanotubes," *Nature*, 386(6623), 377-379, 1997.

Doedel, E. J., "AUTO: A Program for the Automatic Bifurcation Analysis of Autonomous Systems," *Proceedings 10th Manitoba Conference on Numerical Mathematics and Computation*, Winnipeg.

Eikerling, M., and Kornyshev, A. A., "Modelling the performance of the cathode catalyst layer of polymer electrolyte fuel cells," *J. Electroanalytical Chem.*, 453(1-2), 89-106, 1998.

Eikerling, M., Kornyshev, A. A., and Stimming, U., "Electrophysical Properties of Polymer Electrolyte Membranes: A Random Network Model," *J. Phys. Chem. B*, 101, 10807, 1997.

Eisenberg, A., "Clustering of ions in organic polymers, a theoretical approach," *Macromolecules*, 3, 147, 1970.

Farr, W. W., and Aris, R., "Yet Who Would Have Thought The Old Man to Have Had so Much Blood in Him: Reflections on the Multiplicity of Steady-States of the Stirred Tank Reactor," *Chem. Eng. Sci*, 41, 1385, 1986.

Froment, G. F., and Bischoff, K. B., *Chemical reactor analysis and design*, Wiley, New York, 1979.

Fuller, T. F., and Newman, J., "Water and Thermal Management in Solid-Polymer-Electrolyte Fuel-Cells," *J. Electrochem. Soc.*, 140(5), 1218-1225, 1993.

Gierke, T. D., Munn, G. E., and Wilson, F. C., "The Morphology in Nafion Perfluorinated Membrane Products, as Determined by Wide-Angle and Small-Angle X-Ray Studies," *J. Polymer Sci.*, 19(11), 1687, 1981.

Gottesfeld, S., and Pafford, J., "A New Approach to the Problem of Carbon-Monoxide Poisoning in Fuel-Cells Operating at Low-Temperatures," *J. Electrochem. Soc.*, 135(10), 2651-2652, 1988.

Grant, P. M., "Hydrogen lifts off -- with a heavy load," *Nature*, 424, 129-130, 2003.

Gregory, D. P., "The Hydrogen Economy," *Scientific American*, 228(1), 13-21, 1973.

Grubb, W. T., and Niedrach, L. W., "Batteries with solid ion-exchange membrane electrolytes. 2. Low-temperature hydrogen-oxygen fuel cells," *J. Electrochem. Soc.*, 107, 131, 1960.

Guckenheimer, J., and Holmes, P., *Nonlinear Oscillations, Dynamical Systems, and Bifurcations of Vector Fields*, Springer, Harrisonburg, 1983.

Gurau, V., Barbir, F., and Liu, H. T., "An analytical solution of a half-cell model for PEM fuel cells," *Journal of the Electrochemical Society*, 147(7), 2468-2477, 2000.

Gurau, V., Liu, H. T., and Kakac, S., "Two-dimensional model for proton exchange membrane fuel cells," *AIChE J.*, 44(11), 2410-2422, 1998.

Hamelin, J., Agbossou, K., Laperriere, A., Laurencelle, F., and Bose, T. K., "Dynamic behavior of a PEM fuel cell stack for stationary applications," *International Journal of Hydrogen Energy*, 26(6), 625-629, 2001.

Heinzel, A., and Barragan, V. M., "A review of the state-of-the-art of the methanols crossover in direct methanol fuel cells," *J. Power Sources*, 84(1), 70-74, 1999.

Hsing, I. M., and Futerko, P., "Two-dimensional simulation of water transport in polymer electrolyte fuel cells," *Chem. Eng. Sci*, 55(19), 4209-4218, 2000.

Hsu, W. Y., and Gierke, T. D., "Ion Clustering and Transport in Nafion Perfluorinated Membranes," *J. Electrochem. Soc.*, 129, C121, 1982.

Janssen, G. J., "A Phenomenological Model of Water Transport in a Proton Exchange Membrane Fuel Cell," *J. Electrochem. Soc.*, 148, A1313, 2001.

Jeng, K. T., Lee, S. F., Tsai, G. F., and Wang, C. H., "Oxygen mass transfer in PEM fuel cell gas diffusion layers," *J. of Power Sources*, 138, 41-50, 2004.

Kreuer, K. D., "On the development of proton conducting polymer membranes for hydrogen and methanol fuel cells," *J. Membrane Science*, 185(1), 29-39, 2001.

Lee, J. H., and Lalk, T. R., "Modeling fuel cell stack systems," *J. Power Sources*, 73(2), 229-241, 1998.

Lin, G., He, W., and Nguyen, T. V., "Modeling Liquid Water Effects in the Gas Diffusion and Catalyst Layers of the Cathode of a PEM Fuel Cell," *J. Electrochem. Soc.*, 151(12), A1999-A2006, 2004.

Liu, C., Fan, Y. Y., Liu, M., Cong, H. T., Cheng, H. M., and Dresselhaus, M. S., "Hydrogen storage in single-walled carbon nanotubes at room temperature," *Science*, 286(5442), 1127-1129, 1999.

Liu, F. Q., Yi, B. L., Xing, D. M., Yu, J. R., and Zhang, H. M., "Nafion/PTFE composite membranes for fuel cell applications," *J. Membrane Science*, 212(1-2), 213-223, 2003.

Mann, R. F., Amphlett, J. C., Hooper, M. A. I., Jensen, H. M., Peppley, B. A., and Roberge, P. R., "Development and application of a generalised steady-state electrochemical model for a PEM fuel cell," *J. Power Sources*, 86(1-2), 173-180, 2000.

Moxley, J. M., Tulyani, S., and Benziger, J. B., "Steady-state multiplicity in the autohumidification polymer electrolyte membrane fuel cell," *Chem. Eng. Sci*, 58, 4705, 2003.

Nakajima, H., and Honma, I., "Proton-conducting hybrid solid electrolytes for intermediate temperature fuel cells," *Solid State Ionics*, 148(3-4), 607-610, 2002.

Nguyen, T. V., and White, R. E., "A Water and Heat Management Model for Proton-Exchange-Membrane Fuel-Cells," *J. Electrochem. Soc.*, 140(8), 2178-2186, 1993.

Okada, T., Xie, G., and Meeg, M., "Simulation for water management in membranes for polymer electrolyte fuel cells," *Electrochimica Acta*, 43(14-15), 2141-2155, 1998.

Paddison, S. J., "The modeling of molecular structure and ion transport in sulfonic acid based ionomer membranes," *J. New. Mat. Electrochem. Systems*, 4, 197, 2001.

Pasaogullari, U., and Wang, C. Y., "Liquid Water Transport in Gas Diffusion Layer of Polymer Electrolyte Fuel Cells," *J. Electrochem. Soc.*, 151(3), A399-A406, 2004.

Perlmutter, D. D., *Stability of Chemical Reactors*, Prentice-Hall, Englewood Cliffs, 1972.

Perry, M. L., and Fuller, T. F., "A Historical Perspective of Fuel Cell Technology in the 20th Century," *J. Electrochem. Soc.*, 149(7), S59-S67, 2002.

Pisani, L., Murgia, G., Valentini, M., and D'Aguanno, B., "A Working Model of Polymer Electrolyte Fuel Cells," *J. Electrochem. Soc.*, 149(7), A898-A904, 2002.

Raistrick, I. D., "Modified Gas-Diffusion Electrodes for Proton-Exchange Membrane Fuel-Cells," *J. Electrochem. Soc.*, 133(3), C123-C123, 1986.

Ralph, T. R., Hards, G. A., Keating, J. E., Campbell, S. A., Wilkinson, D. P., Davis, M., StPierre, J., and Johnson, M. C., "Low cost electrodes for proton exchange

membrane fuel cells - Performance in single cells and Ballard stacks," *J. Electrochem. Soc.*, 144(11), 3845-3857, 1997.

Ren, X., Springer, T. E., and Gottesfeld, S., "Water and methanol uptake in Nafion membranes and membrane effects on direct methanold cell performance," *J. Electrochem. Soc.*, 147(1), 92-98, 2000a.

Ren, X. M., Zelenay, P., Thomas, S., Davey, J., and Gottesfeld, S., "Recent advances in direct methanol fuel cells at Los Alamos National Laboratory," *J. Power Sources*, 86(1-2), 111-116, 2000b.

Rikukawa, M., and Sanui, K., "Proton-conducting polymer electrolyte membranes based on hydrocarbon polymers," *Progress in Polymer Science*, 25(10), 1463-1502, 2000.

Rosi, N. L., Eckert, J., Eddaoudi, M., Vodak, D. T., Kim, J., O'Keeffe, M., and Yaghi, O. M., "Hydrogen storage in microporous metal-organic frameworks," *Science*, 300(5622), 1127-1129, 2003.

Schlapbach, L., and Zuttel, A., "Hydrogen-storage materials for mobile applications," *Nature*, 414, 353-358, 2001.

Schmitz, R. A., "Multiplicity, Stability, and Sensitivity of States in Chemically Reacting Systems - A Review," *Chem. Eng. Rev.*, 148, 156, 1975.

Springer, T. E., Rockward, T., Zawodzinski, T. A., and Gottesfeld, S., "Model for polymer electrolyte fuel cell operation on reformate feed - Effects of CO, H-2 dilution, and high fuel utilization," *J. Electrochem. Soc.*, 148(1), A11-A23, 2001.

Springer, T. E., Wilson, M. S., and Gottesfeld, S., "Modeling and Experimental Diagnostics in Polymer Electrolyte Fuel-Cells," *J. Electrochem. Soc.*, 140(12), 3513-3526, 1993.

Springer, T. E., Zawodzinski, T. A., and Gottesfeld, G., "Polymer electrolyte fuel-cell model," *J. Electrochem. Soc.*, 138, 2334, 1991.

Srinivasan, S., Dave, B. B., Murugesamoorthi, K. A., Parthasarathy, A., and Appleby, A. J., "Overview of Fuel Cell Technology," Fuel Cell Systems, L. J. M. J. Blomen and M. N. Mugerwa, eds., Plenum Press, New York, 1993.

Standaert, F., Hemmes, K., and Woudstra, N., "Analytical fuel cell modeling," *J. Power Sources*, 63(2), 221-234, 1996.

Thampan, T., Malhotra, S., Tang, H., and Datta, R., "Modeling of conductive transport in proton-exchange membranes for fuel cells," *J. Electrochem. Soc.*, 147, 3242, 2000.

Thirumalai, D., and White, R. E., "Mathematical modeling of proton-exchange-membrane fuel-cell stacks," *J. Electrochem. Soc.*, 144(5), 1717-1723, 1997.

Uchida, M., Aoyama, Y., Eda, N., and Ohta, A., "Investigation of the microstructure in the catalyst layer and effects of both perfluorosulfonate ionomer and PTFE-Loaded carbon on the catalyst layer of polymer electrolyte fuel cells," *J. Electrochem. Soc.*, 142(12), 4143-4149, 1995.

Uppal, A., Ray, W. H., and Poore, A. B., "Dynamic Behavior of Continuous Stirred Tank Reactors," *Chem. Eng. Sci*, 29, 967, 1974.

van Heerden, C., "Authothermic Processes: Properties and Reactor Design," *Ind. Eng. Chem*, 45, 1243, 1953.

Washington, G. B., "Hydrogen cars fuel debate on basic research," *Nature*, 422, 104, 2003.

Watkins, D. S., "Research, Development, and Demonstration of Solid Polymer Fuel Cell Systems," Fuel Cell Systems, L. J. M. J. Blomen and M. N. Mugerwa, eds., Plenum Press, New York, 1993.

Wilson, M. S., Derouin, C. R., Valerio, J. A., and Gottesfeld, S., "Electrocatalysis Issues in Polymer Electrolyte Fuel Cells," *Intersociety Energy Conversion Engineering Conference*, Atlanta, GA, 1203-1208.

Wilson, M. S., and Gottesfeld, S., "High-Performance Catalyzed Membranes of Ultra-Low Pt Loadings for Polymer Electrolyte Fuel-Cells," *J. Electrochem. Soc.*, 139(2), L28-L30, 1992.

Wolf, J., "Liquid hydrogen technology for vehicles," *MRS bulletin*, 684-687, 2002.

Yang, C. R., "Performance of Nafion/Zirconium Phosphate Composite Membranes in PEM Fuel Cells," Princeton University, Princeton 2003.

Yang, C. R., Srinivasan, S., Bocarsly, A. B., Tulyani, S., and Benziger, J. B., "A Comparison of Physical Properties and Fuel Cell Performance of Nafion and Zirconium Phosphate/Nafion Composite Membranes," *J. Membrane Science*, 237, 145-161, 2004.

Yeager, H. L., and Steck, A., "Cation and Water Diffusion in Nafion Ion-Exchange Membranes -- Influence of Polymer Structure," *J. Electrochem. Soc.*, 128(9), 1880-1884, 1981.

Zaluski, L., Zaluska, A., and StromOlsen, J. O., "Nanocrystalline metal hydrides," *J. Alloys and Compounds*, 253, 70-79, 1997.

Zawodzinski, T. A., Derouin, C., Radzinski, S., Sherman, R. J., Smith, V. T., Springer, T. E., and Gottesfeld, S., "Water-Uptake by and Transport through Nafion(R) 117 Membranes," *J. Electrochem. Soc.*, 140(4), 1041-1047, 1993.

Appendix

Summary of experimental records

A. STR-PEM Fuel Cell

FILENAME	DESCRIPTION
	Effect of tightening the fuel cell sandwich on the performance 10 mL/min H_2; 5 mL/min O_2; 80^{o}C – humidified streams
	½ turn:
Step421	Equilibrate at 10 ohm
IVhlf1a, IVhlf1b	Polarization curves
	Finger tight:
Stbntl	Equilibrate at 10 ohm
IVntrl1a, IVntrl1b	Polarization curves
Stepntl	Run at 20 ohm, then step back to 10 ohm
IVntrl2a, IVntrl2b	Polarization curves
	Tight:
Stbtight	Equilibrate at 10ohm
IVtght1a, IVtght1b	Polarization curves
Steptght0408	Run at 20 ohm, step back to 10 ohm
IVtght2a, IVtght2b	Polarization curves
Steptght20409	Continue operating at 10 ohm
Stptght3	Run at 20 ohm, step back to 10 ohm

	Effect of tightening the fuel cell sandwich on the performance 10 mL/min H_2; 5 mL/min O_2; 80°C – dry streams
	<u>Finger tight</u>:
Stb0501	Equilibrate at 10 ohm
IV0502a, IV0502b	Polarization curves
Step0502	Run at 20 ohm, step back to 10 ohm
IV0503a, IV0503b	Polarization curves
	<u>½ turn</u>:
Stb0503	Equilibrate at 10 ohm
IV0503a, IV0504b	Polarization curves
Step0504	Run at 20 ohm, step back to 10 ohm
IV0505a, IV0505b	Polarization curves
Stb0505, stb0506	Run at 10 ohm
	<u>Tight</u>:
Stb0507	Equilibrate at 10ohm
IV0508a, IV0508b	Polarization curves
Stb0508	Run at 10 ohm overnight
IV0509a, IV0509b	Polarization curves
Stb0509	Resume operation at 10 ohm
IV0512a, IV0512b	Polarization curves
	<u>Tightest</u>:
Stb0512	Stabilize at 4.9 ohms overnight
IV0513a, IV0513b	Polarization curves
Stb0513	Run at 5 ohms overnight
IV0514a, IV0514b	Polarization curves
Stb0514	Stabilize at 2 ohms overnight
IV0515a, IV0515b	Polarization curves
Stb0515	Resume operation at 2 ohms overnight
IV0516a, IV0516b	Polarization curves
Stb0516	Stabilize at 1 ohm overnight
IV0517a, IV0517b	Polarization curves
Stb0517	Resume operation at 1 ohm overnight
IV0519a, IV0519b	Polarization curves: obtained at large current
IV0519c, IV0519d	Polarization curves: obtained at low current
Stb0519c	Stabilize at 0.7 ohm
IV0520a, IV0520b	Polarization curves: obtained at low current
IV0520c, IV0520d	Polarization curves: obtained at large current

	½ Tight:
	Load Resistance Effect
Stb0520	Equilibrate overnight at 0.9 ohm, 80 deg C: 90 mA amplitude, 1 hr period
IV0521c, IV0521d	Polarization curves: obtained at large current
IV0521a, IV0521b	Polarization curves: obtained at low current
Stb0521	Equilibrate overnight at 2 ohm, 80 deg C: 70 mA amplitude, 1 hr period
IV0522a, IV0522b	Polarization curves: obtained at low current
IV0522c, IV0522d	Polarization curves: obtained at large current
Stb0522	Equilibrate overnight at 5 ohm, 80 deg C: 20 mA amplitude, 1 hr period
IV0523a, IV0523b	Polarization curves: obtained at low current
IV0523c, IV0523d	Polarization curves: obtained at large current
	Temperature Effect at R_L =5 ohm
Stb0523b	Run at 5 ohm, 90 deg C (no oscillation)
IV0523e, IV0523f	Polarization curves
Stb0523c	Run at 5 ohm, 70 deg C: 25 mA amplitude, 90 min period
IV0524a, IV0524b	Polarization curves
Stb0524b	Run at 5 ohm, 90 deg C (no oscillation)
IV0525a, IV0525b	Polarization curves
Stb0525	Run at 5 ohm, 85 deg C (no oscillation)
IV0526a, IV0526b	Polarization curves
Stb0526	Run at 5 ohm, 60 deg C: 20 to 30 mA amplitude, 2 hr period
IV0527a, IV0527b	Polarization curves
	Temperature Effect at R_L = 2 ohm
Stb0527	Run at 2 ohm, 70 deg C: 80 mA amplitude, 68 min period
IV0528a, IV0528b	Polarization curves: obtained at large current
IV0528c, IV0528d	Polarization curves: obtained at low current
Stb0530	Run at 2 ohm, 60 deg C: oscillations died
IV0531a, IV0531b	Polarization curves, after oscillations subsided
Stb0531	Run at 2 ohm, 90 deg C: no oscillations
IV0601a, IV0601b	Polarization curves
Stb0528	Run at 5 ohm, 50 deg C: oscillations in the beginning but they fade
IV0529a, IV0529b	Polarization curves
Stb0529	Run at 10 ohm, 80 deg C: 3 mA amplitude, 42 min period
IV0530a, IV0530b	Polarization curves
	Oxygen flow rate Effect at R_L = 5 ohm, T= 80 deg C
Stb0601	7 mL/min H_2, 3.5 mL/min O_2: no oscillations
IV0602a, IV0602b	Polarization curves
Stb0602	10 mL/min H_2, 7.5 mL/min O_2: no oscillations
IV0604a, IV0604b	Polarization curves
Stb0604	10 mL/min H_2, 3.0 mL/min O_2: 15 mA amplitude, 48 min period
IV0605a, IV0605b	Polarization curves: obtained at low current
IV0605c, IV0605d	Polarization curves: obtained at high current

Stb0605	10 mL/min H_2, 1.0 mL/min O_2: 14 mA amplitude, 1 hr period
IV0606a, IV0606b	Polarization curves: obtained at low current
IV0606c, IV0606d	Polarization curves: obtained at high current
	Hydrogen flow rate Effect at R_L = 5 ohm, T= 80 deg C
Stb0606	5 mL/min H_2, 5 mL/min O_2: no oscillations
IV0607a, IV0607b	Polarization curves
Stb0607	5 mL/min H_2, 2.5 mL/min O_2: no oscillations
IV0608a, IV0608b	Polarization curves
Stb0608	5 mL/min H_2, 7.5 mL/min O_2: no oscillations
Stb0609	Reset load to 5 ohm
IV06100, IV06101	Polarization curves
IV06110, IV06111	5 mL/min H_2, 1.0 mL/min O_2: no oscillations
	Relative humidity sensors affixed in exit streams
	Run at 5 ohms, 90 deg C, 10 mL/min H_2, 10 mL/min O_2:
Stb0801	- 8 mA amplitude
Stb0804	- Fuel cell tightened to the max tightness
Stb0806	- t > 12000s, increase R_L to 20 ohm (attempt to extinguish oscillations but they persist with an amplitude of ~ 3 mA)
Stb0807	Run at 20 ohms, 70 deg C, 10 mL/min H_2, 10 mL/min O_2
Stb0808	Run at 20 ohms, 90 deg C, 10 mL/min H_2, 5 mL/min O_2 (oscillations persist)
Stb0809	Run at 10 ohms, 90 deg C, 10 mL/min H_2, 5 mL/min O_2 (loosened the fuel cell)
Stb0929	Run at 10 ohms, 65 deg C, 10 mL/min H_2, 5 mL/min O_2 (water condensed in exiting cathode tube)
Stb0930a	Run at 10 ohms, 70 deg C, 5.5 mL/min H_2, 10.2 mL/min O_2
IV1003a, IV1003b	Polarization curves: R_M too large, possible membrane degradation
Stb1003	Run at 5 ohms, 70 deg C
Stb1005	Run at 20 ohms, 70 deg C: prolonged operation at 20 ohms dehydrated the membrane
Stb1006	Run at 2 ohms, 70 deg C, 8.2 mL/min H_2, 10 mL/min O_2
IV1007a, IV1007b	Polarization curves: low current
Tmp1008	Resume operation at previous conditions
IV1008a, IV1008b	Polarization curves: high current
	Reversed anode/cathode feeds
Stb1010	Run at 2 ohms, 70 deg C, 10 mL/min H_2, 10 mL/min O_2
Stb1019	Run at 10 ohms, 70 deg C, 5 mL/min H_2, 10 mL/min O_2 (no oscillations)
Impedancedata2.xls	Impedance data

IV1020a, IV1020b	Polarization curves
Stb1020	Resume equilibration and prior operating conditions (no oscillations)
Stb1022	Run at 5 ohm, 80 deg C, 5 mL/min H_2, 10 mL/min O_2 (attached tubes to the outlet)
Stb1024	Run at prior conditions
Stb1027	Run at 5 ohm, 80 deg C, 5 mL/min H_2, 10 mL/min O_2 (Oscillations observed again)
IV1028a, IV1028b	Polarization curves: high current
Stb1028a	Resume operation at prior equilibration conditions
IV1028c, IV1028d	Polarization curves: low current
	Swapped out new membrane
Stb0123	Run at 5 ohms, 35 deg C, 5 mL/min H_2, 10 mL/min O_2
IV0124a, IV0124b	Polarization curves
Stb0124	Equilibrate overnight at 15 ohms
IV0125a, IV0125b	Polarization curves
Stb0125	Run at 2 ohms, 35 deg C, 5 mL/min H_2, 10 mL/min O_2
IV0127a, IV0127b	Polarization curves
Stb0128	Run at 20 ohms, 35 deg C, 5 mL/min H_2, 10 mL/min O_2
Stb0206	Run at 20 ohms, 70 deg C, 5 mL/min H_2, 10 mL/min O_2 - high membrane resistance (possible membrane dehydration)
IV0209a, IV0209b	Polarization curves
Stb0209	Run at 0 ohm, 75 deg C, 5 mL/min H_2, 10 mL/min O_2 - attempted to rehydrate membrane
Stb0210	Run at 10 ohm, 75 deg C, 5 mL/min H_2, 10 mL/min O_2
Stb0213	Run at 20 ohm, 70 deg C, 5 mL/min H_2, 10 mL/min O_2
IV0214a, IV0214b	Polarization curves
	Run at 20 ohm, 75 deg C, 5 mL/min H_2, 10 mL/min O_2
IV0220a, IV0220b	Polarization curves
Stb0220	Run at 20 ohm, 75 deg C, 5 mL/min H_2, 10 mL/min O_2
IV0224a, IV0224b	Polarization curves
Stb0224	Run at 0 ohm, 65 deg C, 5 mL/min H_2, 10 mL/min O_2
IV0225a, IV0225b	Polarization curves
Stb0225	Run at 0 ohm, 65 deg C, 5 mL/min H_2, 10 mL/min O_2
IV0304a, IV0304b	Polarization curves
Stb0304	Run at 5 ohms, 65 deg C, 5 mL/min H_2, 10 mL/min O_2
Stb0525	Run at 5 ohm, 60 deg C, 7.2 mL/min H_2, 7.2 mL/min O_2
Stb0526	Run at 5 ohm, 60 deg C, 7.2 mL/min H_2, 7.2 mL/min O_2
IV0527a, IV0527b	Polarization curves

B. Segmented Anode Fuel Cell

FILENAME	DESCRIPTION
	Co-current, horizontal configuration:
030905stdst	3.5 ohms, Troom, 5 mL/min H_2, 5 mL/min O_2
030905iva, b	Polarization curves
	Co-current, vertical configuration:
031005stdst	3.5 ohms, Troom, 5 mL/min H_2, 5 mL/min O_2
031005iva, b	Polarization curves
031105stdstA	Troom, 5 mL/min H_2, 5 mL/min O_2 Run at 4ohm for 2 hr 40 min, increase load to 5.6 ohm
031105stdstB	Run at 2 ohm overnight Load changed to 6.24 ohms after 11 hr 45 min Load changed to 2.5 ohms after 15 hr 6 min
031105iva, b	Polarization curves
	Counter-current, horizontal configuration:
031205stdst	3.5 ohm, Troom, 5 mL/min H_2, 5 mL/min O_2
031205iva, b	Polarization curves
031305stdst	8 ohm, Troom, 10 mL/min H_2, 5 mL/min O_2
031305iva, b	Polarization curves
	Counter-current, vertical configuration:
031405stdst	4 ohm, Troom, 5 mL/min H_2, 5 mL/min O_2
031405iva, b	Polarization curves
	Counter-current, horizontal configuration
031505iva, b	Polarization curve recorded after heating at various temperatures
031605stdst	20 ohm, 10 mL/min H_2, 10 mL/min O_2
031605iva, b	Polarization curves
	Co-current, vertical configuration:
031705stdst	20 ohm, Troom, 10 mL/min H_2, 10 mL/min O_2 (dry)
031805stdst	4 ohm, Troom, 10 mL/min H_2, 10 mL/min O_2 (rehydrate)
032105iva, b	Polarization curves
032205stdst	10 ohm, Troom, 10 mL/min H_2, 10 mL/min O_2
032205iva, b	Polarization curves
	Counter-current, vertical configuration, H_2 feed from segment 6:
032205bstdst	10 ohm, Troom, 5 mL/min H_2, 5 mL/min O_2 Heat with lower watt cartridge heaters, change to horizontal configuration. Tune temperature controller.

032205cstdst	Counter-current, horizontal configuration 10 ohm, 80 deg C, 10 mL/min H_2, 5 mL/min O_2
032205ivabriefT80	IV curve taken during initial cooling
032305stdst	Resume operation at 4ohm
032305iva, b	Polarization curve
032405stdst	4 ohm, 65 deg C, 10 mL/min H_2, 5 mL/min O_2
032505stdst	Counter-current, horizontal configuration Response to heating from 65-75 deg C 4 ohm, 10 mL/min H_2, 5 mL/min O_2
032505iva, b	Polarization curve
032605stdst	4 ohm, 75 deg C, 2.2 mL/min H_2, 1.4 mL/min O_2
032705	4 ohm, 75 deg C, 3.7 mL/min H_2, 6 mL/min O_2 Current drops after 7 hours
	Counter-current, horizontal configuration
032905steady11	Load was changed to 0 ohm to rehydrate the cell: *ignition* 0 ohm, 25 deg C, 3.7 mL/min H_2, 6 mL/min O_2
033005steady12	Load stepped from 0 – 3 ohm after 5 hrs 75 deg C, 3.7 mL/min H_2, 6 mL/min O_2
033005steady13	Dry the fuel cell 20 ohm, 75 deg C, 3.7 mL/min H_2, 6 mL/min O_2 Attempt to reignite after 4 hrs at 3ohm
033105steady15	Lower temp to 50 deg C, ignition occurred At 4 hrs, increase temp to 75 deg C to dry out at 20 ohm
040105stdst	20 ohm, 85 deg C, 4 mL/min H_2, 4 mL/min O_2
040205stdst	0 ohm, 85 deg C, 4 mL/min H_2, 4 mL/min O_2 At 3 hr 30 min, flow rates changed to 5 mL/min Load increased to 4 ohm at 6 hrs, 8 ohm at 8.5 hrs
040205stdstAignite	2 ohm, 85 deg C, 5 mL/min H_2, 5 mL/min O_2 After 2 hrs: 75 deg C After 5 hrs: 60 deg C, 4 ohm
040305stdstB	60 deg C, 4 ohm, 5 mL/min H_2, 5 mL/min O_2
040305iva, b	Polarization curve
040305stdstRL	60 deg C, 4 ohm, 5 mL/min H_2, 5 mL/min O_2 Resume operation at equilibrated conditions. Extinguish fuel cell by increasing the load resistance. Segments 5 and 6 extinguished.
040405stdstdecRL	Reignite by decreasing the load resistance

	Co-current, horizontal configuration
040505DstdstDryOsciT75	20 ohm, 75 deg C, 5 mL/min H_2, 6 mL/min O_2 Some small oscillatory behavior
040605coign	20 ohm, 85 deg C, 5 mL/min H_2, 6 mL/min O_2 After 2 hrs: 0 ohm, After 3 hrs: 60 deg C Ignition order: segments 3 5 2 4 6 1
	Counter-current, horizontal configuration
040703cntrign20ohm	20 ohm, 85 deg C, 5 mL/min H_2, 5 mL/min O_2
040805RL5newMEA	5 ohm, 60 deg C, 5 mL/min H_2, 5 mL/min O_2
040905stdRL2	2 ohm, 60 deg C, 5 mL/min H_2, 5 mL/min O_2
041005stdRL10	10 ohm, 60 deg C, 5.4 mL/min H_2, 5.4 mL/min O_2
041105extRL2	10 ohm, 80 deg C, 5.4 mL/min H_2, 5.4 mL/min O_2
041405std	0 ohm, 80 deg C, 5.3 mL/min H_2, 5.3 mL/min O_2 (tried to dry out completely)
041505stdIgTroomCntr	20 ohm, 25 deg C, 5.3 mL/min H_2, 5.3 mL/min O_2
	Co-current, horizontal configuration
041605std	Attempt to reignite at 50 deg C, 0 ohm, 50 deg C, 5.3 mL/min H_2, 5.3 mL/min O_2
	Co-current, vertical configuration
041805coignT25	0 ohm, 25 deg C, 3.5 mL/min H_2, 3.5 mL/min O_2
042005ignco2	0 ohm, 25 deg C, 3.5 mL/min H_2, 3.5 mL/min O_2
042005a, b	Polarization curves
042005stdBco	5 ohm, 25 deg C, 10 mL/min H_2, 10 mL/min O_2 Negative currents observed after temperature was increased to 75 deg C. Load resistance was subsequently decreased to 0 ohms, and increased back up to 2 ohm.
042105iva, b	Polarization curves for fuel cell pre-equilibrated at 70 deg C, 2 ohm, 10 mL/min H_2, 10 mL/min O_2
042105ext.txt	Fuel cell current extinguished
	Counter-current, vertical configuration
042305cntr2ign	0 ohm, 25 deg C, 3.5 mL/min H_2, 3.5 mL/min O_2
042305iva, b	Polarization curve
042405std	0 ohm, 50 deg C, 10 mL/min H_2, 5 mL/min O_2
042505iva, b	Polarization curve
042505std	4 ohm, 50 deg C, 10 mL/min H_2, 5 mL/min O_2
042605iva, b	Polarization curve
042605 std	4 ohm, 50 deg C, 10 mL/min H_2, 5 mL/min O_2 (heating) Fuel cell heated to 70 deg C after 6 hr 26 min
042705std	4 ohm, 70 deg C, 10 mL/min H_2, 5 mL/min O_2
042805std	4 ohm, 70 deg C, 10 mL/min H_2, 5 mL/min O_2 (cooling) Temperature set to 50 deg C after 1 hr 14 min

	Counter-current, vertical configuration
042905std	1 ohm, 50 deg C, 10 mL/min H_2, 5 mL/min O_2 VwA=6 mL, VwC=6 mL – initial liquid volume Measured the volume of liquid produced from each outlet
050105std	VwA=8.2 mL, VwC=10.3 mL
050205std	1 ohm, 50 deg C, 10 mL/min H_2, 5 mL/min O_2 VwA=5 mL, VwC=5 mL – initial liquid volume VwA=5.8 mL, VwC=6.5 mL
050305std	1 ohm, 70 deg C, 5 mL/min H_2, 5 mL/min O_2 VwA=5 mL, VwC=5 mL – initial liquid volume VwA=6.3 mL, VwC=6.5 mL
050605std	Switched graphite pieces an copper backing 20 ohm, 50 deg C, 5 mL/min H_2, 5 mL/min O_2 Fuel cell current extinguished
050805std	Cooled to room temperature 3.5 mL/min H_2, 3.5 mL/min O_2
050905stda	Swapped out MEA, resumed operation at previous conditions
051005std	25 deg C, 5 mL/min H_2, 5 mL/min O_2 Load resistance increased periodically to extinguish the fuel cell current
051105iva, b	Polarization curves
051105stdA	0 ohm, 45 deg C, 5 mL/min H_2, 5 mL/min O_2 Load increased to 20 ohm after 4 hours
051105stdB	0 ohm, 55 deg C, 5 mL/min H_2, 5 mL/min O_2 Load increased to 20 ohm after 18 hours Current in segments 1 thru 3 much larger than 4 thru 6 Current did not extinguish
051205std	0 ohm, 65 deg C, 5 mL/min H_2, 5 mL/min O_2 Load increased to 20 ohm after 14 hours Current not extinguished
051305std	0 ohm, 65 deg C, 5 mL/min H_2, 5 mL/min O_2 Oscillatory behavior attributed to plugs of water flowing out of the fuel cell periodically.
051505std	0 ohm, 70 deg C, 5 mL/min H_2, 5 mL/min O_2 Load increased to 20 ohm after 15 hours Current did not extinguish completely
	Counter-current, flat configuration (cathode on top)
051605std	0 ohm, 60 deg C, 5 mL/min H_2, 5 mL/min O_2
051705std	0 ohm, 70 deg C, 10 mL/min H_2, 5 mL/min O_2 5:25pm – VwA=6.8 mL, VwC=5.8 mL 10:00am – VwA=8.9 mL, VwC=6.5 mL

	Counter-current, vertical configuration
051805std	2 ohm, 75 deg C, 9.8 mL/min H_2, 5 mL/min O_2
	Oxygen flow increased to 9 mL/min after 3 hrs
	1:55pm – VwA=5.7 mL, VwC=5.2 mL
	11:51am – VwA=8.9 mL, VwC=10 mL
051905std	6 ohm, 75 deg C, 10 mL/min H_2, 10 mL/min O_2
052105std	4 ohm, 50 deg C, 9 mL/min H_2, 9 mL/min O_2
052205std	4 ohm, 50 deg C, 9.2 mL/min H_2, 4.6 mL/min O_2
	10:55am – VwA=5.2 mL, VwC=5.2 mL
052305iva, b	9:50am – VwA=5.9 mL, VwC=5.5 mL
052305std	5 ohm, 50 deg C, 9.2 mL/min H_2, 9.3 mL/min O_2
	Co-current, vertical configuration
052305stdCO	5 ohm, 50 deg C, 9.2 mL/min H_2, 9.3 mL/min O_2
	t = 0 – VwA=6.0 mL, VwC=7.0 mL
	t = 17 hr 40 min – VwA=6.4 mL, VwC=7.1 mL
052405stdCO	5 ohm, 65 deg C, 9.2 mL/min H_2, 9.2 mL/min O_2
052405stdB	5 ohm, 60 deg C, 5 mL/min H_2, 5 mL/min O_2
	t = 0 – VwA=6.5 mL, VwC=7.1 mL
	t =17.5 hr– VwA=6.9 mL, VwC=7.4 mL
052505std	5 ohm, 60 deg C, 3.5 mL/min H_2, 3.5 mL/min O_2
	t = 0 – VwA=6.9 mL, VwC=7.4 mL
	t =23 hr – VwA=7.5 mL, VwC=7.8 mL
052605std	5 ohm, 60 deg C, 9.2 mL/min H_2, 9.2 mL/min O_2
	t = 0 – VwA= 5 mL, VwC= 5 mL
	t =7.5 hr – VwA=5.1 mL, VwC=5 mL
052605stdB	5 ohm, 70 deg C, 9.2 mL/min H_2, 9.3 mL/min O_2
	t = 0 – VwA=5.1 mL, VwC=5.0 mL
	t =6.5 hr – VwA=5.25 mL, VwC=5.05 mL
052605stdC	5 ohm, 25 deg C, 9.2 mL/min H_2, 9.2 mL/min O_2
	t = 0 – VwA=5.25 mL, VwC=5.0 mL
	t = 11 hr – VwA=5.3 mL, VwC=5.15 mL
053005std	5 ohm, 40 deg C, 9.2 mL/min H_2, 9.3 mL/min O_2
	t = 0 – VwA=5.65 mL, VwC=6.15 mL
	t =23.5 hr – VwA=6.05 mL, VwC=6.40 mL
053105std	5 ohm, 35 deg C, 9.2 mL/min H_2, 9.3 mL/min O_2
	t = 0 – VwA=6.05 mL, VwC=6.40 mL
	t =6.5 hr – VwA=6.35 mL, VwC=6.60 mL
	Counter-current, vertical configuration
060205std	5 ohm, 25 deg C, 9.2 mL/min H_2, 9.3 mL/min O_2
060305std	5 ohm, 25 deg C, 9.2 mL/min H_2, 9.3 mL/min O_2
	t = 0 – VwA=3.95 mL, VwC=5.0 mL
	t = 21 hr – VwA=4.15 mL, VwC=5.9 mL
060505std, 060605std	5 ohm, 40 deg C, 9.2 mL/min H_2, 9.3 mL/min O_2
060705std	5 ohm, 50 deg C, 9.2 mL/min H_2, 9.3 mL/min O_2

	t = 0 – VwA=4.9 mL, VwC=6.2 mL t = 28.5 hr – VwA=5.3 mL, VwC=6.5 mL
060805std	5 ohm, 60 deg C, 9.2 mL/min H_2, 9.3 mL/min O_2 t = 0 – VwA=5.0 mL, VwC=6.5 mL t = 25 hr – VwA=5.3 mL, VwC=6.6 mL
060905std	5 ohm, 70 deg C, 9.2 mL/min H_2, 9.3 mL/min O_2 t = 0 – VwA=5.3 mL, VwC=6.6 mL t = 23 hr – VwA=5.8 mL, VwC=6.9 mL
061005std	5 ohm, 70 deg C, 9.2 mL/min H_2, 9.3 mL/min O_2 t = 0 – VwA=5.0 mL, VwC=5.0 mL t = 2 days – VwA=6.0 mL, VwC=5.2 mL
	Co-current, vertical configuration
061305std	5 ohm, 25 deg C, 9.2 mL/min H_2, 9.3 mL/min O_2 t = 0 – VwA=6.1 mL, VwC=5.95 mL
061505std	5 ohm, 25 deg C, 9.2 mL/min H_2, 9.3 mL/min O_2 t = 5 days – VwA=6.5 mL, VwC=8.3 mL
062005std	5 ohm, 40 deg C, 9.2 mL/min H_2, 9.3 mL/min O_2 t = 0 – VwA=5.5 mL, VwC=5.5 mL t =23 hr – VwA=5.9 mL, VwC=5.9 mL
062105	5 ohm, 50 deg C, 9.2 mL/min H_2, 9.3 mL/min O_2